Stony Brook University

Evaluation of Electromagnetic Interactions between PET and MRI systems for Simultaneous MRI/PET Imaging

A Dissertation Presented

by

Sri Harsha Maramraju

to

The Graduate School

In Partial Fulfillment of the

Requirements

for the Degree of

Doctor of Philosophy

in

Biomedical Engineering

(Medical Physics)

Stony Brook University

May 2011

Stony Brook University

The Graduate School

Sri Harsha Maramraju

We, the dissertation committee for the above candidate for the

Doctor of Philosophy degree, hereby recommend

acceptance of this dissertation.

David J. Schlyer, PhD – Dissertation Adviser
Senior Scientist, Brookhaven National Laboratory; Assoc. Prof., BME dept., SBU

Terry Button, PhD – Chairperson of Defense
Associate Professor, Department of Radiology, Stony Brook University

Paul Vaska, PhD
Scientist, Brookhaven National Laboratory; Asst. Prof., BME dept., SBU

Craig Woody, PhD
Senior Physicist, Brookhaven National Laboratory

This Dissertation is accepted by the Graduate School.

Lawrence Martin

Dean of the Graduate School

Abstract of the Dissertation

Evaluation of Electromagnetic Interactions between PET and MRI systems for Simultaneous MRI/PET Imaging

by

Sri Harsha Maramraju

Doctor of Philosophy

in

Biomedical Engineering

(Medical Physics)

Stony Brook University

2011

Multi-modality imaging in clinical and pre-clinical settings promises to forge new vistas for better diagnostic interpretation compared to stand-alone imaging systems. For in vivo imaging studies, accurate interpretation of diseased conditions is possible if structural, functional and metabolic information of the region of interest is provided at the same time. At Brookhaven National Laboratory, a small animal positron emission tomograph (PET) detector was integrated into a Bruker Biospin 9.4 T microMRI scanner to perform simultaneous PET/MRI studies in rodents. The custom-built MRI coils were optimized for simultaneous PET/MRI studies. The feasibility of acquiring simultaneous PET/MRI data has been demonstrated that can provide structural soft-tissue contrast information from MRI complementing with physiological and metabolic information from PET at the same time. However, the technical challenges involved in integrating PET inside the high field MRI scanner have been predominant, because of the mutual electromagnetic interactions between the two systems that may compromise the overall performance of either system. The main aim of the dissertation is to identify and evaluate the electromagnetic interactions between the PET and MRI systems. The impact of radiofrequency

pulses on the sensitive PET electronics was investigated by employing different shield configurations around the PET detector housing. In addition, the assessment of MR image quality was performed using phantoms in the presence of powered PET detector covered with different shields. With thin layers of copper shielding and good grounding practices, it has been shown that the effect of radio frequency pulses on PET readout electronics was minimized and good quality MR images were acquired. In vivo simultaneous PET/MRI data of a rat brain and a mouse heart were acquired with different PET radiotracers that illustrate one of the potential applications for performing simultaneous PET/MRI studies.

To my mother, who taught me (and still teaching me) how NOT to take life so seriously

To my father, who kept asking me when I will be done with my PhD

Table of Contents

List of Figures

List of Tables

Acknowledgements

Six years is a long time and I cannot thank and acknowledge enough all the people involved in making this journey more memorable and interesting. This PET/MRI research is a result of involvement of many people, who contributed directly and/or indirectly towards a fruitful execution of the objectives. I have been lucky to be a part of this ensemble of intellectuals, who motivated me to get inspired, pushed me grow as a researcher and simply, shaped me up!

I thank my adviser Dr. David J. Schlyer, who has been gracious, generous and kind to provide me unconditional guidance and support since day one. Your sense of humor is spot on! I thank Dr. Terry Button, chairperson of my dissertation committee, for your insight and suggestions on the research work. I still remember your diet coke breaks between the classes. I would especially like to thank Dr. Paul Vaska, whose insight in problem-solving helped in tackle some of the toughest challenges in all the projects that we worked on. I am grateful to Dr. Craig Woody, with whom I share the same sentiments of being pessimistic about the experimental plans and deadlines, but eventually celebrate the fruits of success. I still remember how happy we both were when we got the first input function results from the beta-microprobe and more recently the PET/MRI experiments. I also thank Dr. David Smith, for pushing me to think beyond what I thought was sufficient in integrating PET/MR systems. It was a pleasure working with you.

I am truly privileged to work with Dr. Sergio Rescia, who along with Dr. David Smith helped me with the development of MRI coils. Without your help in troubleshooting some of the tricky shielding problems, this work wouldn't have been possible. I thank Sean Stoll for your quick fixes and a helping hand in assembling and integrating the PET system. I learned a lot from you about attention to detail. I will always remember our short van rides from Physics to MRI and back. I am immensely thankful to all my dear friends and colleagues Dr. Sachin Junnarkar, Dr. Martin Purschke, Dr. Jean-Francois Pratte, Dr. Aarti Kriplani, Dr. Daniela Schulz, Dr. Sudeepti Southekal, Bosky and Srilalan for their insightful suggestions, discussions, petty talks, fun and tolerating all my wrong doings! Thanks Lalan for all the help when I was sick and Sudeepti for all your pseudo-advising. I thank Dr. Karen Kinsella for her constant support during my thesis completion.

I am grateful to Kaushik and Aneeta, my two very good friends at Stony Brook, who dragged me out of the lab and reminded me that there can be a social life while doing research. Without their encouragement, I would have looked twice as old as I am now! I thank my childhood friend Vamsee, who has been there for me all along my graduate years and has been my strength, inspiration and support during tough times. You have been the most consistent human being I have come across thus far and I am ever so grateful to you for providing a homely environment and a peaceful state of mind.

Finally, I would like to thank my mother Mrs. Udaya, for her constant demonstrations of love and support. You have been my positive motivating force and inspiration, apart from taking pleasure of making fun of me and being a good sport! I thank my father Mr. Padmakar Rao, for reminding me about how not to lose momentum during my studies. I thank my brother Avinash and sister-in-law Divya, for being great pillars of support for all these years!

This research was carried out at Brookhaven National Laboratory under contract DE-AC02-98CH10886 with the U.S. Department of Energy as collaboration between BNL and the State University of New York at Stony Brook.

CHAPTER 1: BACKGROUND AND SIGNIFICANCE

1.1 Introduction

The main aim of this dissertation is to identify and evaluate the electromagnetic interactions between the Positron Emission Tomograph (PET) and Magnetic Resonance Imaging (MRI) scanners, when integrated together and operated simultaneously. Various interactions may occur due to the electromagnetic fields that exist when a powered PET device is operated in an MRI environment. Understanding the mechanisms of interactions and identifying ways to minimize the interference will help minimize the performance degradation of one system in the presence of the other. By creating an electromagnetically compatible environment during PET/MRI studies, an uncompromised acquisition of simultaneous anatomic, functional and metabolic information is possible that would demonstrate the synergistic strengths of the two systems.

1.2 Motivation for multi-modality imaging

Advances in pre-clinical research have expedited the utilization of non-invasive imaging modalities for tumor detection and disease diagnosis. Many stand-alone small animal imaging modalities such as X-ray Computerized Tomography (CT) and Magnetic Resonance Imaging (MRI) provide anatomical landmarks. For example, the delineation of tissues, fine anatomical detail of the rigid brain structure and superior soft tissue contrast are attainable with the excellent spatial resolution of MRI systems. Nuclear medicine imaging systems such as Positron Emission Tomography (PET) and Single Photon Emission Computed Tomography (SPECT) are commonly used to extract the metabolic pathways and understand the physiology in the living body. PET has been widely used for its ability to obtain high sensitivity *in-vivo* functional information, along with the assessment of biochemical and enzymatic processes in the body.

PET studies using various radiotracers that bind to specific receptors or enzymes can be used to assess the biochemical pathways for gene expression [1] and cell trafficking. There is a possibility that these markers are bound to non-specific signal sites in the tissue. Determining the anatomical location of specific binding is often difficult with PET, without the anatomical

landmarks provided by the MRI or CT. This is especially important in cell trafficking studies *in vivo.* The only way to confirm the biodistribution is to sacrifice and dissect the animal. Therefore, efforts are being made to integrate different imaging techniques that can provide both functional and anatomical information non-invasively in the same animal. Some of the examples of multimodality imaging techniques include PET/CT, SPECT/CT, PET/MRI/MRS, SPECT/MRI etc. The PET device that provides high sensitivity functional information when combined with high resolution CT or MRI utilizes the strengths of both modalities [2, 3]. Besides providing landmarks for the interpretation of PET data, the anatomical data obtained from CT can be used to provide information for attenuation correction of 511 keV photons in tissue and correct for activity spillover if the size of the structure is small in comparison to the resolution of the scanner. This information is necessary for accurate quantification of radiotracer concentration *in-vivo*. There have been recent developments in combining SPECT with MRI systems to extract the complementary information [4, 5].

1.3 PET/MRI Vs. PET/CT

The integration of simultaneous PET with MRI in small animal research has provided the opportunity to combine form and function. Both MRI and PET have evolved remarkably in pre-clinical settings and are now beginning to utilize the full potential of their respective strengths. In recent years, the advent of combined MRI and PET was realized after identifying the advantages the two modalities can offer in synchronizing structural, functional and metabolic information. Although scanners combining PET and CT paved the way in improving the accuracy in detecting disease [6], a few shortcomings were identified [7, 8]. The PET and CT scanners occupy a single gantry with a CT scan followed by PET sequentially. Given the slow acquisition of PET data compared to CT, this sequential procedure may lead to imperfect co-registration of the images due to the change of position and shape of tissue between scans [9]. This is a significant concern in pre-clinical studies as the image fusion of sequential scans in small animal studies could lead to inaccurate results. Since CT is limited to anatomical information, it is impossible to get temporal correlation of any process from the perspective of two different modalities. CT also comes with additional radiation dose per scan, limiting repeated imaging of the same animal

[10]. The agents used to enhance soft-tissue contrast in CT may also alter biological function in the organ of interest in animal models [11].

As an alternative, MRI provides better soft-tissue contrast without additional radiation dose compared to CT [12]. MRI can also be used to extract spectroscopic information by performing Magnetic Resonance Spectroscopy (MRS), which can measure pathological processes in the organ or ratios of metabolite concentrations to detect any tissue specific abnormalities. It can also be used to assess functional phenotypes in transgenic mouse models [13]. This metabolic information from MRS can be combined with biochemical and molecular information from PET to serve as a research tool and to monitor disease progression in animal models. Temporal correlation of the PET and MRS data has a potential application in correlating drug localization using PET with the simultaneous metabolic changes in that region using MRS *in vivo*. Another advantage of combining MRI with PET (as opposed to CT with PET) is the ability to use different MR pulse sequences (e.g. gradient echo, spin echo etc.) with greater flexibility to highlight different tissue characteristics. In addition, functional MRI (fMRI) provides functional information of the brain using blood oxygenated level dependent (BOLD) contrast. Unlike sequential PET/CT procedures, the acquisition of PET and MRI data can be made truly simultaneous, allowing accurate spatial and temporal correlation of the PET and MR images. The synchronized acquisition of structural, pharmacological and physiological information provides vital bodily processes *in-vivo* with an accurate anatomical framework and without compromising the spatial and temporal information from the two systems. Moreover, combined PET/MRI may reduce the scanning time and increase the repeatability of using the same animals in longitudinal pre-clinical studies, thus improving the throughput.

In a clinical setting, it has been reported that the co-registered PET/MR images along with diffusion tensor imaging have helped characterize epileptogenic brain disorders in patients [14]. The co-registration of PET and MR images was also used as a presurgical protocol to detect cortical dysplasia in patients requiring epilepsy surgery [15]. Other correlation studies using PET and MRI data of patients were performed to study Alzheimer's disease [16], pancreatic disorders [17, 18] and other diseased conditions [19-22]. Unlike PET/CT, the acquisition of PET and MRI data can be made truly simultaneous, allowing accurate spatial and temporal correlation of the PET and MR images, including the abdomen or pelvic regions in small animal imaging. There has been a lot of interest to perform whole body PET/MRI studies in humans for

oncological imaging [23-25] and further explore the integration of time-of-flight PET capability with MRI [26]. A recent publication by Boss *et al.* demonstrates the feasibility of obtaining simultaneous PET/MR brain images to study intracranial tumors with results comparable to PET/CT datasets [27]. The glucose metabolism in the substructures of the hippocampus was measured by Cho *et al.* [28]. With the synergistic integration of MRI and PET, the dynamic data obtained from both modalities can be compared, validated and quantitatively analyzed. Applications can be extended to cardiac, tumor and brain mapping studies as some of the examples of performing simultaneous PET/MRI in humans [29-31].

1.4 Technical challenges

The realization of combining PET and MRI comes with the technical challenges of integrating the PET detector in the MRI scanner. It is important to understand the extent of the impact that each system would have in the presence of the other. Unlike PET/CT, the imaging volumes of both PET and MRI must align for simultaneous imaging. Also, the integration of the two modalities is primarily dependent upon the PET detector geometry and the available space.

Conventional PET detectors are based on photomultiplier tubes (PMTs), which are very sensitive to magnetic fields. One of the main challenges for developing a PET/MRI scanner has been the effect of the high magnetic fields on the PMTs. The cascade of electrons produced between the dynodes in the PMTs is accelerated by the electric field and produce more secondary electrons. The electron path between the dynodes is deflected under the influence of strong magnetic fields, which may eventually lose their ability to detect light photons, resulting in corruption of PET data. Moreover, there is a tendency of the magnetic fields and fast switching gradients to interfere with or completely paralyze the PET readout electronics. The limited space inside the bore of the MR scanner is another hindrance in the placement of the PET detector.

PMTs are bulky in size and occupy more space. A mechanical integration of the PET detector hardware inside the MRI scanner becomes extremely difficult due to PMT size. The magnetic components often used in PET detectors can cause inhomogeneities in the field leading to susceptibility artifacts and loss of image quality in the MR images. The gradient fields may induce eddy currents due to the presence of ferromagnetic components in the PET scanner,

which may distort the MR images. Therefore, integrating the two scanners without compromising the performance of either is only possible by minimizing the electromagnetic interference (EMI).

1.5 Different approaches to combining PET and MRI scanners

For simultaneous acquisition of the MRI and PET data, it is essential to integrate the PET detector inside the MRI scanner. The placement of the radio frequency (RF) coil that is used for transmitting and receiving MR signals, is critical to minimize the interference with the PET detector. One scheme is to insert the RF coil inside the PET scanner. This is the most desirable as most standard RF coils are small and compact and can be easily retro-fitted inside the PET detector ring. This type of configuration is used in many of the current prototype PET/MRI systems for small animal imaging, with an assumption that the RF pulses do not pass through the PET detector ring when appropriate shielding arrangements are used. The PET electronics can be shielded from RF pulses to avoid any damage or interference of RF in the PET data. The PET/MRI combination can also be fabricated with the PET detectors outside the MRI field-of-view, similar to a PET/CT system. This is a recent approach implemented by Philips Gemini PET/MR system specifically designed for human PET/MR applications. However, the acquisition will be sequential requiring changing the patient bed positions. Figure 1.1 shows the schematic of these two approaches. The third approach is to have the PET system inside the RF coil when acquiring MRI data (not shown in the figure). This configuration can be employed with open MRI systems. Depending on the different geometries of the RF coils and the construction of the PET scanners, either of the approaches can be implemented to further explore the compatibility issues with different PET/MRI system configurations.

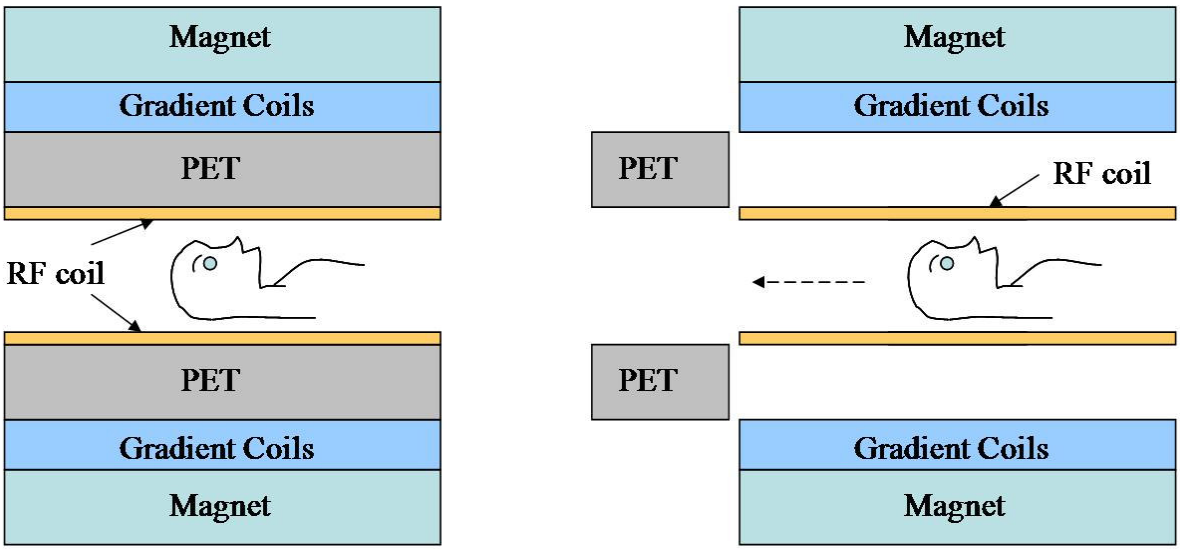

Fig. 1.1. Simultaneous PET/MRI approach with the PET inside the field-of-view (left) and sequential PET/MRI approach with the PET outside the field-of-view (right).

Implementing the first approach with PET inside the MRI, three possible PET/MRI arrangements were employed to build prototype PET/MRI systems depending on the sensitivity of the PET photodetectors in the MRI environment, as shown in figure 1.2.

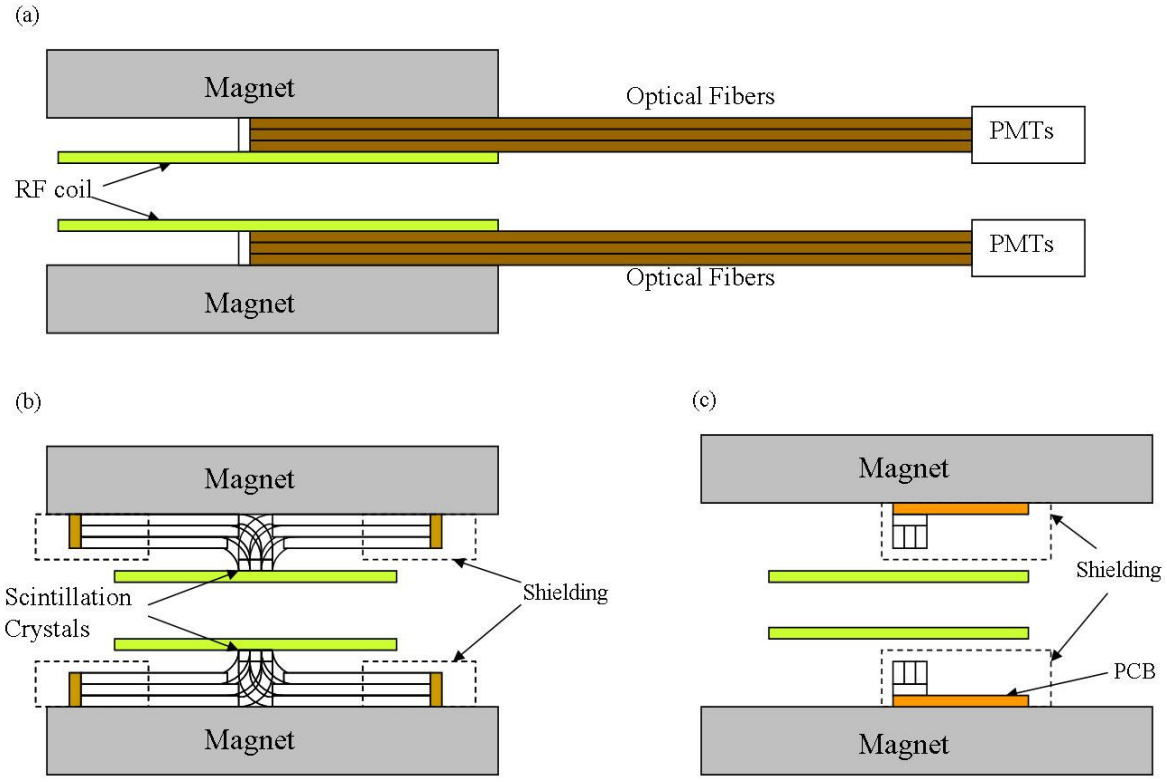

Fig. 1.2. Different PET/MRI system arrangements to obtain simultaneous PET/MRI data.

1.5.1 Optical fibers

Due to the sensitive nature of PMTs to even small magnetic fields, one of the approaches to minimize the EMI between the two systems was to move the PMT-based detector modules outside the magnetic field and employ fairly long optical light guides that are coupled to the scintillation detectors (Figure 1.2(a)). In 1995, Christensen *et al.* [32] first reported the use of optical light guides connected to the PMTs to realize a combined PET/MRI system. The same principle was implemented by other research groups [3, 33-38]. In this configuration, the EMI between the two scanners is minimized with only the scintillators being in the MR field-of-view. The PMTs do not require EMI shielding and this configuration is relatively easy to implement. One of the main caveats of using long fibers of several meters is that there is significant loss of scintillating light due to the efficiency of the light coupling and the bending of the fibers. This can result in degraded energy resolution, inaccurate crystal identification and poor timing resolution. With a large number of scintillation crystals, it is difficult to directly couple optical fibers due to the space constraints in the MRI scanners. This arrangement also limits the axial extent of the PET scanner.

Researchers from King's College (London) have developed a PET/MRI scanner using optical fibers to direct scintillating light photons to multichannel PMTs [39, 40]. The PET device comprises of four concentric rings LSO crystals, which provide depth of interaction information. About 70 % light loss was observed with the use of 3.25 m long optical fibers. In another study, the demonstration of *in vivo* simultaneous PET/MR images of rat brain was obtained by Raylman and co-workers with two PET detector blocks inside a General Electric 3 T Signa MRI scanner [33]. Each PET detector consists of 20 x 20 arrays of LSO crystals (2.5 x 2.5 x 15 mm^3) and was coupled to position sensitive PMTs via 2.5 m optical light guides. However, the PET device had poor energy resolution (85 %) FWHM due to attenuation of scintillation light in the long optical fibers. Although PET/MR images were acquired, demonstrating the feasibility of the system, the performance of the position sensitive PMTs (PSPMTs) were degraded by 24 % when inserted in the MRI scanner. Another research group from Japan developed a PET/MRI system based on PMTs and long fibers with depth of interaction information capability [37, 38, 41]. Two LGSO crystal layers were used having different decay times (33 ns and 43 ns) [38]. The PSPMTs are positioned in a low magnetic field region of a 0.3 T MRI scanner. The PET device employs dual

layer LGSO blocks coupled to PSPMTs through ~ 80 cm long optical fiber bundles. Simultaneous rat brain images were obtained with this device.

1.5.2 Split Gradient MRI

A novel PET/MRI system was developed by a research group from the University of Cambridge, UK [42, 43]. It is based on split magnet design where the PET scanner is installed between the two 1 T superconducting magnets. The technique is novel as the PSPMTs are positioned in the radial direction of the MR scanner, as opposed to axial direction as employed in other approaches. The 120 cm light guides connect the LSO crystals to PSPMTs operating within a 1 mT field. However, only 40% of scintillation light is transferred to the photodetectors in this configuration. Nevertheless, simultaneous PET/MR images were successfully obtained with this system.

1.5.3 PET field-cycled MRI

A research group from Western Ontario, Canada has developed a novel approach of using the field-cycled MRI technique [44], where the PET data is acquired between MRI operations. The field-cycled MRI system consists of two separate magnetic fields. One of the two is a strong polarized magnetic field of 1 T, which is used to magnetize the sample. This field is rapidly switched ON and OFF. The second 'readout' magnetic field having field strength of 0.1 T is switched ON and is utilized for MR image acquisition. In this system, the polarized magnetic field is a strong field with no requirement to have a steady homogeneous field, unlike the conventional MR systems. Also, the homogeneous readout magnetic field does not have to be strong to acquire the MR signals. This arrangement would reduce the technical difficulties of designing the system, compared to conventional MR system design. The idea is to have the PET device installed in the gap of the polarizing magnet. However, PET data is only acquired when magnetic fields are turned OFF, so this system is not applicable for simultaneous PET/MR imaging, restricting the temporal correlation studies in small animals.

1.5.4 APD-based PET/MRI Systems

Although using light guides minimized the EMI and good MRI signals were obtained, the performance of PMT-based PET devices was reported to be compromised because of significant scintillation light loss. This arrangement can also limit the axial field of view of the PET scanner. This led to the development of solid state PET systems that allow placement of PET inserts in even small bore magnets. Unlike PMTs, solid state avalanche photodiodes (APDs) can operate in high magnetic fields [45, 46]. They are small, compact, have high quantum efficiency compared to PMTs, and can be coupled to the scintillators without the need of optical fibers.

New PET/MRI systems were developed using APDs and simultaneous PET/MRI phantom and animal data were acquired successfully [47-51]. A hybrid approach was demonstrated by Catana and co-workers from University of California, Davis, who coupled short optical fiber bundles (10 cm length) were coupled to position-sensitive APDs [49], as shown in figure 1.2(b). The PET insert is comprised of 16 LSO/APD modules with inner diameter of 60 mm. LSO scintillators, each measuring 1.43 x 1.43 x 6 mm^3, were placed in the center of the MRI bore while APDs reside outside the MRI field of view to further minimize any MR interferences [48, 49]. This arrangement was advantageous as no metallic components were placed at the isocenter of the magnet. The timing resolution is 25 ns for this system, with an energy resolution of 25.5 % and an absolute sensitivity of 0.6 %. Simultaneous PET/MR images of a whole body mouse were successfully obtained with this device. Also, *in vivo* mouse brain MR spectroscopy and diffusion weighted imaging (DWI) were performed simultaneously with PET [49]. However, subtle artifacts in MR images remain and expanding the axial extent of the PET scanner is limited due to the use of optical fiber bundles.

The PET/MRI research program from the University of Tuebingen has become a pioneer in preclinical studies and has obtained simultaneous PET/MR images of the mouse brain, mouse heart and has combined PET data with functional MRI and MR spectroscopy studies [45, 47, 50]. Their PET system consists of 10 LSO/PSAPD modules, where each LSO (1.6 x 1.6 x 4.5 mm^3) crystal 12 x 12 array is coupled via a custom-made light guide to 3 x 3 APD array. This particular configuration also allows expanding the detector in the axial direction, as the PSAPDs are directly coupled to the LSO crystals (Figure 1.2(c)). The PET detector ring (ID = 60 mm) is placed inside ClinScan Bruker Biospin 7 T MRI scanner. As standard Bruker RF coil is used that can easily fit into the PET system, but the FOV is limited by the dimensions of the RF coil

(OD/ID = 60 mm/35 mm), with an axial FOV of 19 mm. The time resolution is calculated to be 8.2 ns inside MRI. The system energy resolution was 25.1 % when measured inside the MRI, with a detection sensitivity of 0.23 % [47]. Simultaneous PET/MRI phantom and animal studies were carried out successfully in the Bruker 7 T scanner. Recently published data demonstrates the ability to carry out simultaneous PET/MRI cardiac studies in a mouse model of infarct [52]. Another research group from Sungkyunkwan University, Korea, developed a PET module based on Geiger-mode APDs coupled to LYSO crystals [53]. The charge output from the photodetectors was transmitted to the preamplifier station outside the MRI FOV. The feasibility of this approach was demonstrated in this study.

The feasibility of PET/MRI technology has also been extended to human brain studies with the PET device mounted in a clinical 3 T human MRI scanner [54, 55]. A recently published work demonstrated the feasibility of performing PET/MRI studies in humans to diagnose intracranial tumors [27].

1.5.5 SiPM-based PET/MRI systems

Although APD-based PET detectors have many advantages compared to PMTs, subtle artifacts may exist as the gain and noise in APDs are sensitive to temperature [45]. There has been a recent development of solid-state photosensors using silicon photomultipliers (SiPMs) that have a potential to be used as PET detectors. They possess the strengths of both PMTs and APDs as they provide much higher signal amplitudes than APDs, can be operated with simple preamplifiers and are insensitive to magnetic fields. Currently, SiPMs are being tested for their overall optimum performance for PET applications including time-of-flight [56, 57] and is currently being evaluated in order to be used in PET scanners operating in high magnetic fields [58-61].

1.6 Recent developments and performance evaluation of PET/MRI systems

Several research groups have developed prototype PET/MRI systems as discussed in the previous section. Many review articles laid emphasis on the design constraints and the degree of interference with the PET/MRI systems, in addition to the potential applications [62-66]. An article by Herzog *et al.* highlighted some of the current challenges encountered in the PET/MRI

system design by various research groups around the world as presented in recent imaging conferences and PET/MRI workshops [67]. New studies report the need for attenuation correction for human PET/MRI applications [68-74]. There has been some interest in exploring the iron oxide nanoparticle radiolabeling with PET radiotracers to develop PET/MRI dual agents [75-77]. A recent publication by Frullano *et al.*, noted the significance of developing a PET/MRI dual agent to map extracellular pH values in diseased conditions [78]. A European (HYPERImage) consortium (http://www.hybrid-pet-mr.eu) was established by investigators from six countries who are developing a time-of-flight PET/MRI system for clinical research [79]. The transition from preclinical PET/MRI investigations to clinical studies is evident and could provide wealth of information towards diseased conditions in patients in the future.

The performance evaluation of some of the existing preclinical PET/MRI systems was reported. The impact of MR on the PET performance was investigated by researchers in University of California, Davis [80], who earlier examined the interference between the two systems [49]. The reconstructed image spatial resolution was reported to be 1.21 mm at cFOV with or without MR pulsing. The average energy resolution is 25 % and the sensitivity of the scanner is 0.31 % using a 25.4 mm phantom with 80 ns wide coincidence time window. The same research group has evaluated the electromagnetic interactions due to the presence of different shield configurations near the MR imaging volume [81]. It was concluded that the chemical shift imaging can be used as an important tool to quantify the impact of metallic objects near the isocenter of the magnet. Research group from the King's College, London, UK evaluated the performance of their MRI-compatible PET system using optical fibers [82]. They reported a spatial resolution of 1.5 mm at the cFOV, 70 % energy resolution and 0.95 % sensitivity with 20.9 ns time window. On the other hand, Wehrl *et al.* at University of Tuebingen, Germany, assessed the effect due to the presence of PET system on MR image quality and RF noise interference [83]. It was noted that the PET system did not significantly deteriorate the MR imaging performance. The attenuation properties and the impact of MRI hardware on PET reconstruction were evaluated by Delso *et al.* for whole body PET/MRI applications [84]. The focus on investigation of the impact of PET on MRI and MRI on PET systems is significant to not only evaluate the performance capability of the existing PET/MRI systems, but also to build new PET systems that can withstand electromagnetic interactions in

the MRI environment. In addition, any improvements to the PET device geometry and thorough magnetic compatibility of the detectors must be performed at the design level.

1.7 Dissertation Outline

The main objective of this research is to understand and minimize the mutual electromagnetic interactions between a PET device and an MRI scanner in a bi-modal imaging system. This dissertation proposes to study the negative impact of one system over the other and to optimize the performance of each system by evaluating the shielding and grounding conditions required to obtain acceptable PET/MRI data simultaneously. Thorough evaluation of mutual interference can provide insights for design and development of new hybrid PET/MRI scanners at the design level. The focus of this work is on identification of the electromagnetic interactions in the MRI environment as well as evaluating the feasibility of conducting simultaneous PET/MRI.

The initial portion of the work as described in Chapter 2 will give a brief overview of the MRI principles and a short description of PET and MRI scanners along with the design and construction of a custom-built RF coil. Some of the significant observations during the simultaneous operation of unshielded PET system inside the MRI are discussed in Chapter 3. The sources of electromagnetic interaction mechanisms between the two systems and the introduction to the different ground distributions and shielding theory are explored in Chapter 4. Chapter 5 will present the imaging results from the PET/MRI system as well as the results due to the impact of RF pulses on the PET system using different shields. Analysis and further discussions of the experimental results are presented in Chapter 6. The PET system performance results are presented after employing optimal shield followed by some of the limitations of the study. Chapter 7 presents the future directions and conclusions.

CHAPTER 2: SCANNER DESCRIPTIONS: MAGNETIC RESONANCE IMAGING AND POSITRON EMISSION TOMOGRAPH

This chapter mainly focuses on the basic principles and hardware components of Magnetic resonance Imaging (MRI) and Positron Emission Tomograph (PET) scanners. A brief description of the Bruker 9.4 T MRI scanner is described along with the design and construction of custom-built RF coil for PET/MRI applications.

2.1 Basic principles of Magnetic Resonance Imaging (MRI)

The basic principles behind the physics of MRI are well understood through the fundamental concepts of electromagnetic (EM) waves, proton spin physics and nuclear magnetization. One of the characteristics of EM waves is that they travel at the speed of light. They have two components: an electric field and a magnetic field. These fields are 90^0 out of phase with each other. The propagation of the EM wave in vacuum is perpendicular to both electric and magnetic components. Hence any change in the electric field results in a corresponding change in the magnetic field and vice-versa. For MR imaging applications, the magnetic component of the EM wave is more significant, compared to the electric component which absorbs energy and dissipates heat. In the spectrum of EM waves, the MRI operating frequencies mostly fall in the radio wave region. Therefore, the radiofrequency (RF) system in the MRI is capable of transmitting RF signals into the imaging sample. The interaction of this signal with the sample is recorded, which is later processed and reconstructed into an MR image. The basis for MRI signal accumulation can be explained by the nuclear spin physics of the protons.

The Hydrogen nuclei

Our body contains many atoms. Hydrogen atoms are in abundance in the form of water molecules (H_2O) and fat. The hydrogen nucleus consists of a single proton that possesses a positive charge and spins around its own axis. Any charged particle with nuclear spin produces an intrinsic electromagnetic field. This characteristic of the hydrogen nuclei with a positive charge is exploited in obtaining MR signal. When an unpaired proton is placed in an external magnetic field, it wobbles or 'precesses' around the applied field as shown in Figure 2.1. This is

because the proton experiences a force (torque) due to its motion resulting in angular momentum. The rate or the frequency at which the proton precesses is proportional to the strength of the magnetic field applied and is given by the Larmor equation:

$$\omega = \gamma B_0$$

where ω is the angular precessional angular frequency of the proton in radians per second, B_0 is the external magnetic field strength measured in tesla (T) and γ is the proportionality constant known as the gyromagnetic ratio, expressed in radians $s^{-1}T^{-1}$. The equation can be re-written in terms of linear frequency as

$$f = \gamma B_0/2\pi,$$

where f is the Larmor frequency (expressed in MHz) at which the proton precesses. For a hydrogen nucleus (γ= 267.513 Mrad $s^{-1}T^{-1}$) the Larmor frequency is 42.6 MHz at 1 T. For the magnetic strengths of 1.5T, 4T and 9.4T, the corresponding Larmor frequencies are 63.86 MHz, 170.3 MHz and 400.3 MHz respectively. Therefore, the stronger the magnetic field B_0 the faster the proton precesses about this field.

When an RF pulse is transmitted into an imaging sample (e.g. tissue) perpendicular to the external magnetic field B_0, it excites (flips) the protons from the longitudinal magnetization and changes the direction of its precession to the transverse plane. The flipping of protons from longitudinal plane to the transverse plane is possible only if the frequency of the bursts of RF energy matches with the precessional frequency of the protons. The system is then said to be in 'resonance'. If the RF bursts are not at the Larmor frequency, then there won't be any resonance and no realignment of the protons. A detailed description of this phenomenon can be found in [85]. The RF pulse adds energy to the protons when in resonance. The protons gradually relax to their original alignment when the RF pulse is switched OFF. During this recovery (or relaxation) time, they emit weak EM waves acquired as 'MR signal' at the RF receiver. Just like a moving charged particle generates magnetic field, an oscillating magnetic field causes movement of charged particles by reciprocity. Therefore, an induced flow of charged particles (electrons) results in induced voltage and current on the RF receiver, which is measured as an MR signal that undergoes further amplification, digitization, signal processing and final MR image reconstruction steps.

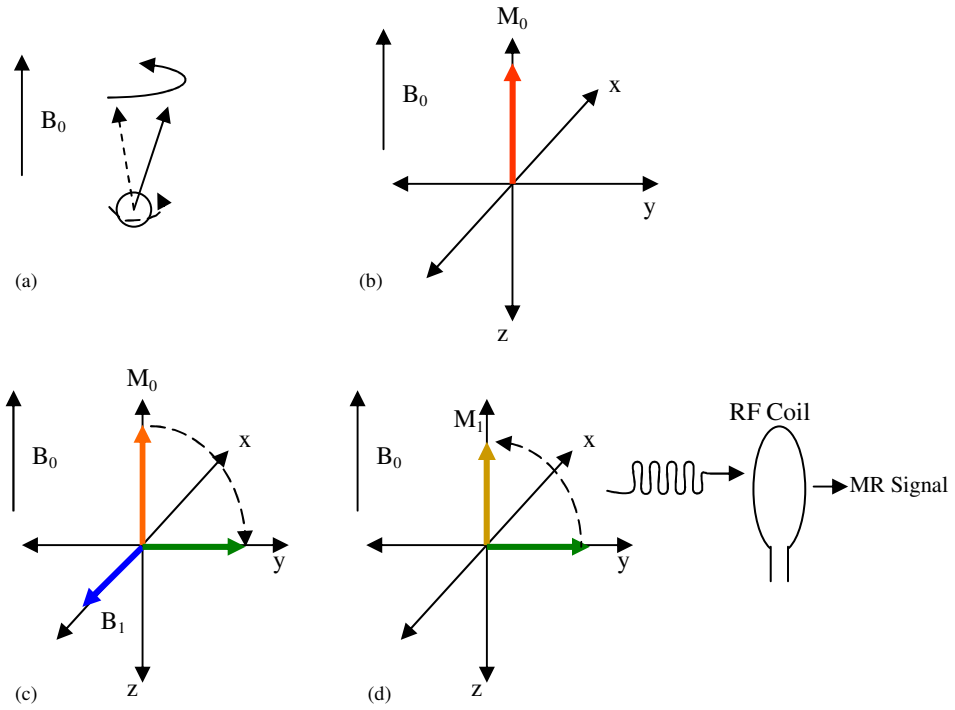

Fig. 2.1. Precession of a proton in a magnetic field. (a) A single proton with positive charge in the presence of external magnetic field precesses around the axis of the applied field. (b) Using three-dimensional Cartesian coordinates, the external magnetic field B_0 is along the z-axis, where the protons are in equilibrium having a longitudinal magnetization vector M_0. (c) When B1 field is applied along x-axis perpendicular to B_0 field, the protons are displaced from longitudinal plane to x-y transverse plane. (d) As the protons transition from transverse plane back to the equilibrium, they emit EM waves (from the principles of reciprocity) that are captured by RF coil as an MR signal.

2.2 MRI Hardware

This section briefly outlines the MRI instrumentation and hardware components of the MRI scanners that are commercially available. The MRI system in general constitutes a large horizontal bore magnet that accommodates the volume of interest; the gradient system which creates linear changes in the magnetic field in the X, Y and Z-planes; the RF transceiver system which transmits and receives MR signals and a computer that performs data acquisition, processing and image reconstruction. Figure 2.2 shows the basic components of the MRI system. Below are some of the key features of each of these components.

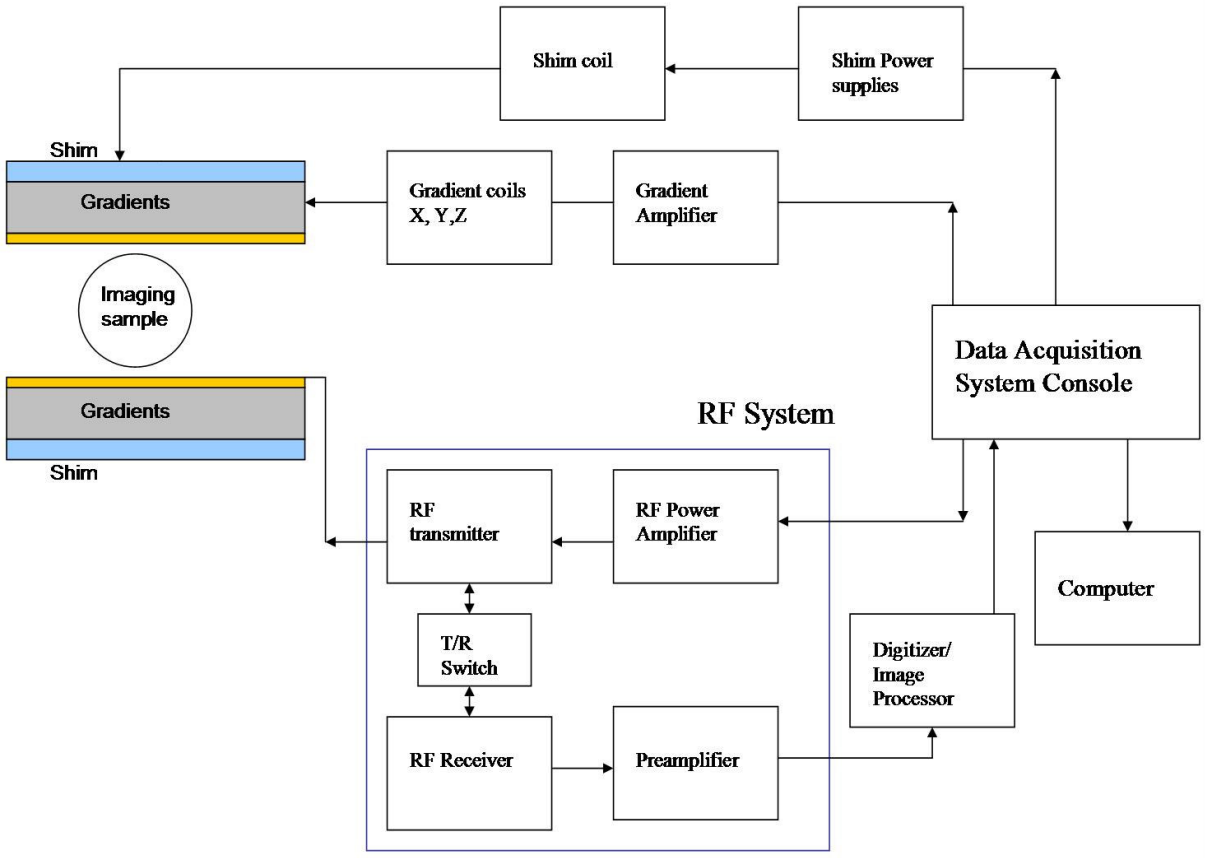

Fig. 2.2. Simplified schematic of the basic components of the MRI system.

2.2.1 The magnet

There are three main types of magnet designs that are available. They are permanent, resistive and superconducting magnets.

Permanent magnets: As the name indicates, the permanent magnets are always ON and cannot be turned OFF. They do not require liquid cooling and are low on maintenance. However, for human applications they are very heavy (100 tons) and can provide a maximum magnetic field strength of only about 0.5 T.

Resistive magnets: They are based on the principle of the current flowing through the coil producing an electromagnetic field. They can be easily turned OFF in case of an emergency. Maximum field strength of only 0.3T can be achieved using these magnets. Poor uniformity and constant power supply are some of the disadvantages of this type of magnets.

Superconducting magnets: Superconducting magnets are widely used in many research and clinical facilities. They can generate ultra high magnetic fields and operate near absolute zero

temperature (-270 ^{0}C). These magnets require liquid helium cooling to maintain zero resistance on the conducting wires, hence the name superconducting magnet. A high level of magnetic field homogeneity can be maintained using these magnets. However, liquid helium must be supplied regularly to maintain the temperature and they remain ON as long as the temperature is maintained. One of the important considerations in choosing the type of magnet is to maintain a high degree of homogeneity, where the changes in the magnetic field are minimal over a wide volume of imaging sample. This is essential for obtaining good MR image quality.

2.2.2 The gradient system

Gradient coils are elaborately wound coils that are very carefully designed to create linear variations to the main magnetic field in one specific spatial direction. These coils are essential in localizing the signals from a selected tissue. There are three orthogonal gradients in the X, Y and Z-directions that are assembled inside the magnet bore and are utilized to generate an intentional linear perturbation in the homogeneous magnetic field allowing the spatial encoding of the tissue. The magnitude of variation in the field is on the order of mT/m, which is low compared to the external magnetic field but is high enough to localize the spatial information of the tissue. Rapid switching of linear gradients result in the banging noise heard in the magnet because the gradient coils carry high currents (on the order of several hundred amperes) for a very short period of time. The coils experience force and try to move, resulting in noise when switched ON and OFF rapidly. The different designs of gradient coils can be found in the literature [86].

2.2.3 Shim coils – magnetic shimming

Maintaining a high degree of homogeneity in the external magnetic field B_0 is ideal in an MRI scanner, to obtain artifact-free MR images. However, inhomogeneities may exist due to the poor site location, inefficient shielding or floor plan, magnetic field susceptibility etc. The sample being imaged may also be a primary source of distortion in the magnetic field. The shim coils are used to shim the magnetic field to compensate for the offset and correct for magnetic field distortion. They are usually shim plates, iron bars or small magnets that are placed in the bore between the main magnet and the gradient coils.

2.2.4 The RF system

The RF transceiver system is used to transmit RF excitation pulses and receive the MR signal from the tissue. The system consists of an RF synthesizer, an RF power amplifier and an RF transmit/receive coil. The RF synthesizer provides a center frequency with a master clock and controls the phase of the RF pulses [87]. The RF power amplifiers are used to provide enough power to excite the protons in the sample to be imaged. The RF coils are used to transmit RF bursts or receive the signal from the body or both. They are responsible for uniform excitation of the imaging volume and receiving the signal from the body without any phase distortions. Different types of RF coils are discussed at length in the literature [88] depending on the applications. The basic design of the RF coils is discussed further in section 2.3.

2.2.5 The data acquisition system

The weak MR signals go through various stages of amplification before they are digitized, demodulated and filtered. The data is pre-processed, segmented and finally reconstructed to obtain a 3-dimensional MR image. In order to obtain uncorrupted weak signals, it is usual to shield the MR room to prevent any unwanted radiation from disrupting the MR signal. A Faraday cage is created by shielding the MR room with thin walls of copper or steel.

2.2.6 Fringe fields

The field emanating from the main magnet is called the fringe field. In ultra high frequency magnet systems, the fringe fields may extend to a large distance and they may have undesirable effects on the electronic systems in the vicinity such as electronic device monitors, power cables, computers and consoles. Also, these fields maybe harmful for persons having any metal fragments in their bodies. Precautions must be taken to restrict MR room access for the people wearing medical implants such as pacemakers. To contain the fringe fields, active shielding is employed where another set of conductive windings are used that partially oppose the main magnetic fields. In some MRI scanners, room shielding is employed to truncate the fringe fields. The distance at 0.5 mT (5 G line) is considered safe for persons with medical implants.

2.3 Basics of RF coil design

One of the most important components of the RF system is the RF resonator, commonly known as RF coil. The basic purpose of the RF coil is to resonate at the Larmor precession frequency. This is achieved by generating uniform fields perpendicular to the static magnetic field to flip the protons in the tissue. There are three main types of the RF coils namely, the transmitter only coil, the receiver only coil and the transmitter/receiver or transceiver coil. The transmitter only coil generates the RF excitation, while the receiver only coil detects the weak induced voltages on the receiver circuitry when the transmitter is OFF. Both coils can be used independently or in congruence for MRI studies. The transceiver coil can be used to excite both the RF signals (creating the B_1 field) and detect MR signals from the imaging sample. In order to generate a desirable MR signal, the RF coil must generate an effective magnetic field (B_1) to flip the protons uniformly over a desired volume. In other words, all the protons must experience same amount of RF energy within the excitation volume.

In terms of network theory, the RF design is an example of an electrical circuit. Any current carrying conductor has some resistive, inductive and capacitive components to it. The opposition to the flow of electrons in a conductor is generally defined as resistance (R) expressed in ohms (Ω). The current carrying conductor produces a magnetic field around it. The constant of proportionality of the flux linked to a coil with the current in the coil is given by inductance (L) expressed in henrys (H). The component in the circuit that stores energy in the form of an electric field is the capacitance (C) expressed in farads (F). An inductor stores energy in the form of magnetic field. Inductors and capacitors cause the current to be out of phase with the voltage. The ratio between the voltage and the current is the impedance, which consists of an in-phase (real) component called resistance and a 90degrees out-of-phase part called reactance (purely imaginary and is denoted by j, where $j = (-1)^{1/2}$). Impedance (Z) is the vector sum of inductive reactance, capacitive reactance and resistance. The impedance of R-L circuit is given by

$$Z = R + jX_L$$

where the resistance R is the real part of the impedance and the reactance X_L is the imaginary part of the impedance ($X_L = \omega L$). The resistance R is located on the real axis, while the inductive

reactance X_L is located on the positive *j* axis as shown in the Figure 2.3 below. The sum of R and X_L gives the complex impedance.

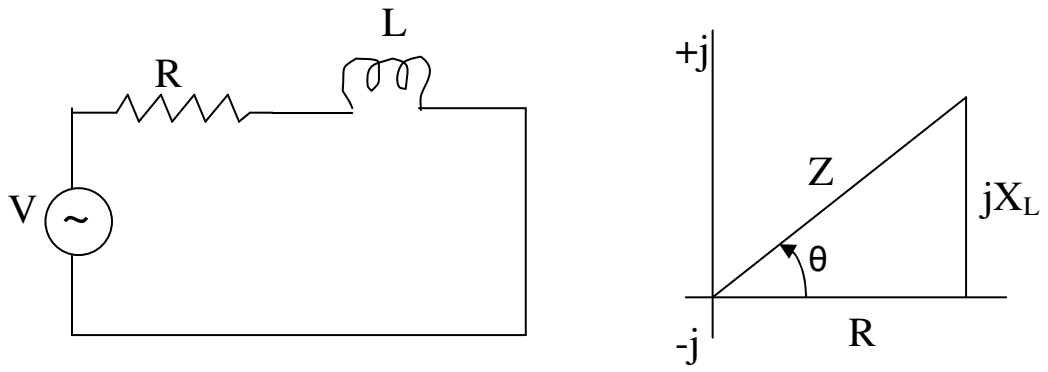

Fig. 2.3. R-L circuit (left) with reactance components when displayed on the complex plane (right).

Similarly, the impedance of R-C circuit is given by

$$Z = R - jX_C$$

where Z consists of resistance R in real part and capacitive reactance ($X_C = 1/\omega C$) in imaginary part, as shown in figure 2.4. The angle between the resistance and impedance is the phase angle between applied voltage and current in the circuit.

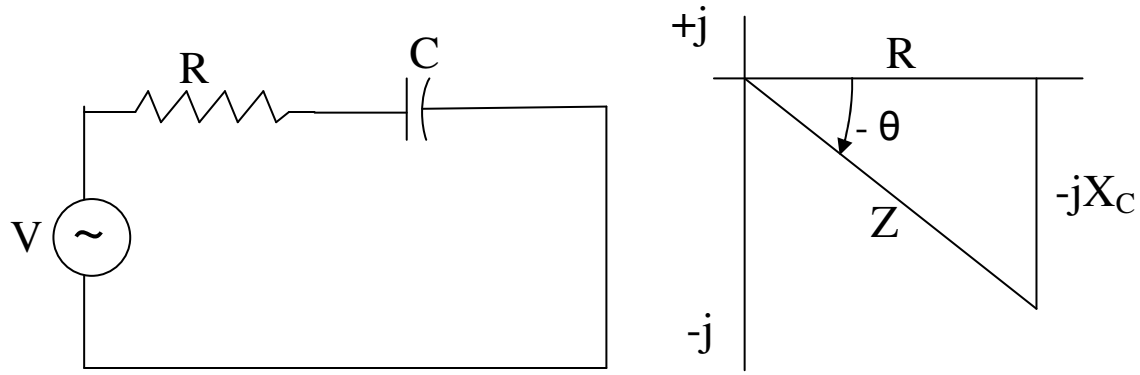

Fig. 2.4. R-C circuit (left) with reactance components when displayed on the complex plane (right).

From the impedance diagrams of R-L and R-C circuits, it is clear that the reactance components are 180^0. If we consider a series or a parallel R-L-C circuit, the current lags behind or leads the applied voltage, depending on the values of X_L and X_C. When $X_L > X_C$, the circuit is predominantly inductive. If $X_C > X_L$, the circuit is more capacitive.

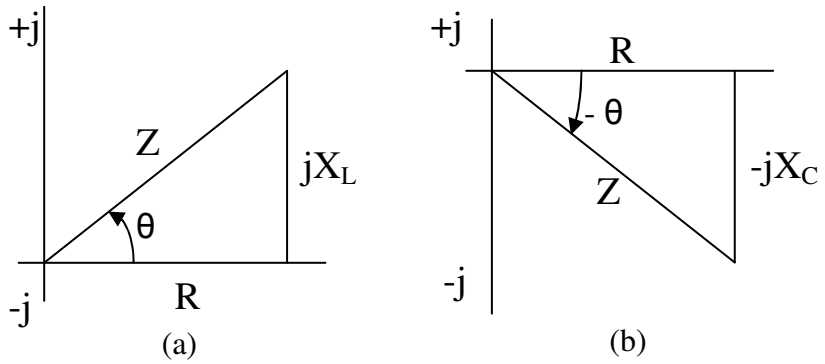

Fig. 2.5. The impedance diagrams of R-L circuit (a) and R-C circuit (b). Note that the reactances are in opposite directions in both diagrams.

However, if one of the parameters of the R-L-C circuit is varied such that the current in the circuit is in phase with the applied voltage, then the circuit is said to be in *resonance*. At resonance

$$X_L = X_C$$

$$j\omega L = \frac{j}{\omega C}$$

$$\omega = \frac{1}{\sqrt{LC}}$$

$$\text{Since } \omega = 2\pi f, \; f_R = \frac{1}{2\pi\sqrt{LC}}$$

where f_R is the resonance frequency.

Almost all the electric circuits offer impedance to the flow of current. Therefore, a typical RF coil design is an example of a tuned R-L-C circuit, where the reactance components must cancel each other and the impedance of the tuned circuit will become pure resistance. A sharp frequency response can be achieved by tuning the circuit at resonance. Figure 2.6 shows an example of a resonant circuit of a typical RF coil with series capacitive matching.

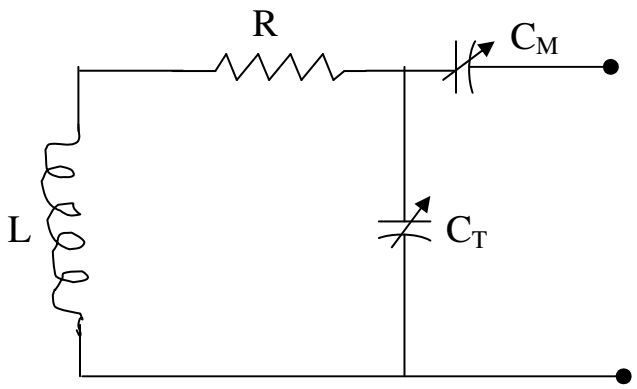

Fig. 2.6. An RF coil circuit diagram. R = resistance; L = inductance; C_T = tuning capacitance; C_M = matching capacitance.

Coil Tuning

By tuning, we mean to adjust the frequency of the RF coil to resonate at the Larmor frequency and excite the protons in the sample. These adjustments are usually performed by varying the capacitance values on the coil, using non-magnetic variable capacitors or electrically adjustable variable capacitor diodes. The imaging sample inside the coil distorts the field as the sample acts as a group of conductive elements. By tuning the coil to the appropriate frequency we are maximizing the receiving signal.

Coil Impedance Matching

Assuming to use a 50 Ω RF amplifier, to maximize power transfer to the RF coil, the coaxial cable has a characteristic impedance of 50 Ω. Hence, for efficient power transfer, the RF coil impedance must also be matched to 50 Ω in order to match the 50 Ω output of the power amplifier. At the resonance frequency, the coil impedance becomes a pure resistance of 50 Ω (the reactive components of the capacitance and inductance should cancel each other). This kind of *impedance matching* is employed in order to improve the efficiency of RF transmission into the imaging sample. If the impedance matching is not optimized, the transmitted RF energy is reflected rather than being absorbed in the imaging sample. It may lead to inefficient RF excitation yielding poor MR image quality. Moreover, inefficient impedance matching would require increasing the power levels of the RF.

The efficiency of the RF coils is measured by a quality (Q) factor. In any L-C circuit, inductors and capacitors have stray resistance as well as the conductors. These resistive losses cause heat dissipation. With an increase in the frequency the resistance increases due to the skin

effect. The Q factor is the ratio of the maximum energy stored to the energy dissipated per cycle. It is also a measure of voltage and current variations in the circuit and determines the overall performance of the coil [86]. Depending on the load variations in the coil, the non-magnetic tuning and matching capacitors are used to adjust the coil frequency to the resonant frequency and to match the impedance of the coil to 50 Ω coaxial cable from the power amplifier, thus, maintaining high Q factor.

2.3.1 Types of RF Coils

In general practice, surface coils and volume coils are the two prominent types of RF coils that are employed. The surface coil is usually in the shape of a ring with a small coil diameter (typically 25 mm for small animal studies). They are useful to receive signal close to the area of interest peripherally, but they lose signal away from the coil as the penetration depth in the tissue is dependent on the coil radius. In general, the closer the coil is to the imaging sample, the better the MR signal. Surface coils are generally used as a receiver to image small anatomical structures (e.g. small animal brain studies).

The volume coils, on the other hand, cover the entire tissue of interest to broadcast oscillating RF fields uniformly. They are supported on a cylindrical structure surrounding the imaging sample. A circular loop of conducting wires or conducting foils around the surface of the cylindrical structure is used to carry alternating currents and establish a homogenous B_1 field. The common examples of volume coils are the Saddle coils and Birdcage coils. A Saddle coil typically consists of thin films or strips of conductor (copper) arranged on the surface of the cylindrical structure forming identical loops. Each loop carries identical currents flowing in the same direction and creates uniform magnetic field lines. This principle is similar to the design of the gradient coils, but the objective is to optimize the uniformity of the magnetic field rather than to achieve maximum linearity [89]. The sinusoidal distribution of the currents is obtained by four conductors in a Saddle coil. Birdcage coils, on the other hand, have equally spaced segmented multiple conductors supported by two circular end rings. They generate better uniform magnetic fields compared to Saddle coils. Birdcage coil design is widely used in many commercially available MRI scanners.

2.3.2 Quadrature coils

The RF coils that are described so far are examples of linearly polarized coils. Here, a single coil pair is used to excite the spin magnetization of the protons by generating alternating currents that have a constant phase. This is an example of an RF coil that generates field along one direction. The receiving MR signal is the result of resonance absorption of only those proton spins that are precessing in that phase. The MR signal from the out-of-phase proton spins does not interact with the receiver circuitry and is dissipated as heat into the imaging sample. The linearly polarized RF coil is only half efficient in rotating the spin magnetization.

Quadrature coils [90, 91] on the other hand, utilize two coil pairs (placed orthogonal to each other) to detect the signals that are both in-phase and out-of-phase, increasing the receiver sensitivity by a factor of $\sqrt{2}$ and reducing the RF power by half. In this mode, one coil pair of the two-pair system is rotated 90^0. Driving the alternating currents that are phase-shifted by 90^0 in each of the coils, result in detection of effective magnitude of the net magnetization along orthogonal directions. This is achieved when the induced currents on the receiver undergoes a 90^0 phase shift. The quadrature coils rephase the currents that contribute to improvement of the signal by 40 %. This is commonly called circularly polarized coil. The detection mode is termed 'quadrature' because the input signal is split in two with same magnitude but differ in quadrants (90^0 apart).

In order for the RF coil to function in quadrature mode, two coil pairs that are independent of each other or that decouple during resonant modes must be utilized to generate orthogonal magnetic field components. In this RF coil, two coil pairs are arranged orthogonally as shown in the Figure 2.7. During RF transmission, the driving (incoming) currents are split into two separate signals that differ in phase by 90^0 and are fed to the RF transmitter simultaneously. This generates circularly polarized fields with equal magnitudes. Two signals (one is real, while the other is imaginary) are received that are 90^0 out-of-phase with each other. The vector sum of the signals from the two orthogonally arranged coils contributes to the total magnitude of the signal. If the real and the imaginary components are considered as vectors that are perpendicular to each other, the resultant magnitude is computed by its vector sum, which represents the absolute phase of the received signal ($\sqrt{2}$ times the original signal). The RF power is reduced to half because when the RF excitation from one coil begins to decline, the excitation from the other orthogonal

coil starts increasing due to the 90^0 phase shift. The RF exposure to the imaging sample is reduced in this configuration.

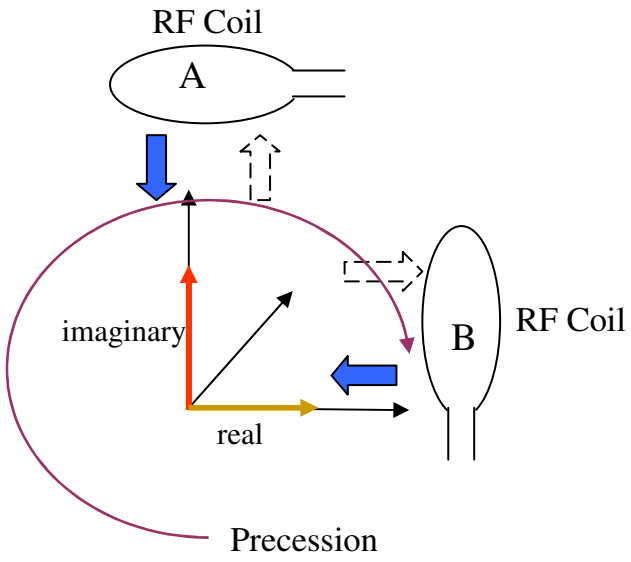

Fig. 2.7. Working of a quadrature coil (transmit and receive). Two independent RF coils A and B are oriented orthogonal to each other. The shaded arrows indicate the RF energy is split into two in these coils with a 90^0 phase difference. This would result in detecting the signal from the proton's spin precessing in the same direction (blue arrow). The dotted arrows show the signal detected independently at each coil that is received as real and imaginary components. The magnitude of these two components (the diagonal) can be combined to produce a signal which is 1.41 ($\sqrt{2}$) times more than a linear coil.

Two main criteria must be met to use the RF coil in quadrature mode. The first one is to split the RF transmission power into two currents that have a 90^0 phase difference. The second criterion is to combine the two 90^0 components in the receiving signal that is fed into the preamplifier and not leaked into the transmission load. This is achieved by constructing a four-port circuit, commonly called as a splitter/combiner or a 90^0 hybrid branch-line network device. These types of RF hybrid combiners and dividers are commonly used in high frequency radio communications and measurement instruments.

From the Figure 2.8, the input port 1 is connected to the RF transmitter. The ports 2 and 3 that are responsible for exhibiting the 90^0 phase shift are connected to the RF coil. The output port 4 is connected to the RF preamplifier. Here ports 1, 4 and 2, 3 are isolated from each other. The RF pulse from port 1 is split in quadrature mode to ports 2 and 3. This results in a rotating magnetic field on the transverse plane. If the direction of nuclear magnetization is in the same direction as

the Larmor precession, the MR signals with a 90^0 phase difference are received at ports 2 and 3. These signals are summed in phase at port 4, which is connected to the preamplifier.

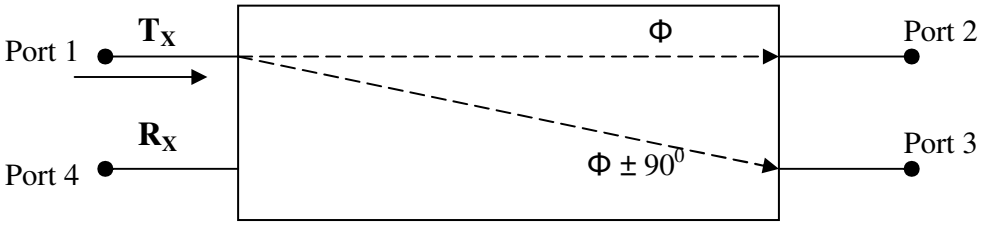

(a) Transmit mode

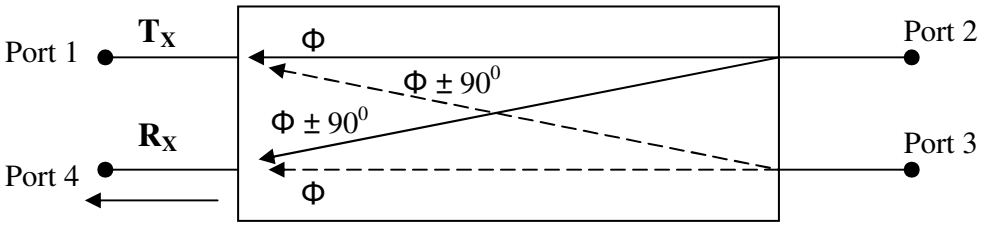

(b) Receive mode

Fig. 2.8. Schematic of the four-port 900 hybrid phase-sensitive quadrature detector device in transmit and receive modes, which is used to operate the RF coil in quadrature.

Port 1, on the other hand, sees the signals that are out of phase by 180^0 and they cancel out. In this way, the receiving signals are not leaked at the transmission load. The four-port 90^0 hybrid network must be electrically and mechanically symmetrical to obtain the desired output. A detailed description about the construction of hybrid devices at high frequencies can be found in [92].

2.4 Positron Emission Tomography (PET)

Positron Emission Tomography (PET) is a non-invasive imaging technique that maps the biochemical and physiological processes *in vivo*, through quantitative imaging of positron emitter labeled molecules in the human body. It mainly employs a short-lived positron emitting radioisotope (i.e. ^{11}C, ^{13}N, ^{15}O and ^{18}F), which is administered to the patient through injection. When the radioisotope decays, it emits a positron. It looses its energy after a short path length (few millimeters) and is annihilated by coming in contact with an electron, giving off a pair of anti-parallel 511 keV gamma photons emitted at approximately 180^0 relative to each other. This

simultaneous emission of two annihilation photons is detected in coincidence by detectors surrounding the patient. With a large number of these events it is possible to reconstruct an image of the *in vivo* radioisotope distribution. Hence, the main goal of the PET systems is to use the PET radiotracers and generate PET images of biodistribution, drug pharmacokinetics etc.

The Rat Conscious Animal PET (RatCAP) detector [93] is a 3-dimensional (3D) ring tomograph that is capable of imaging a conscious adult rat brain. It is a miniaturized PET device that is attached to the rat's head directly to eliminate motion between the head and the scanner, while permitting the movement of the rat [94]. Retaining the same design, architecture and technology, the latest version of the RatCAP with non-magnetic materials (such as APD sockets, pins etc.) was used, to integrate the PET device optimized for reliable operation in the presence of high magnetic fields. Some of the significant modifications of the new RatCAP version include an upgrade from single-ended signal readout to low noise, low voltage differential signal (LVDS). This technique is capable of minimizing potential digital interference to analog circuits [95].

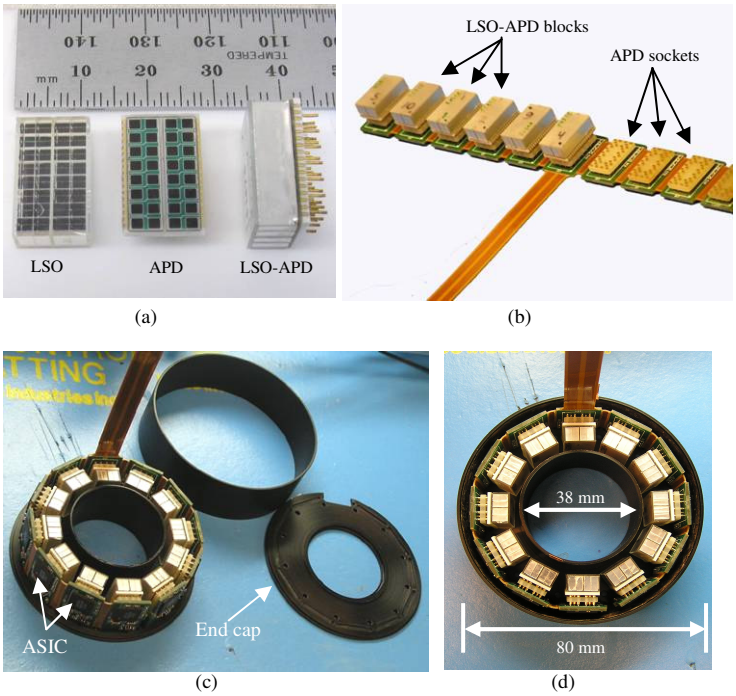

Fig. 2.9. Components of the PET detector. (a) LSO crystals and non-magnetic APDs. (b) The LSO-APD blocks are coupled together and plugged into the non-magnetic APD sockets on the flexible circuit. (c) Custom-designed ASICs are embedded at the front-end of the PCB. (d) The flexible PCB is rolled to form the PET ring in a plastic housing.

Further description of front-end readout [96], signal processing chain [97], PET data processing [98] and image reconstruction [99] of the new version of the RatCAP [95] is already reported in detail. Briefly, a total of 12 detector blocks constitutes the PET ring and each of these blocks consists of a 4 x 8 array of 2.22 x 2.22 x 5 mm^3 lutetium oxyorthosilicate (LSO) crystals (Proteus Inc.) bonded together with a 0.078 mm thin reflective foil (3M VM 2000), separating the individual crystals. The LSO crystals are coupled with a matching non-magnetic S8550 (Hamamatsu) APD array as shown in Figure 2.9 (a). Experimental and simulation results of the light collection efficiency measurements using these APD arrays have been previously reported [100]. More preliminary results using a 5 mm LSO crystal block coupled to S8550 APD array are provided in [94, 101]. Each LSO-APD block is plugged into a non-magnetic APD socket mounted on the flexible printed circuit board (PCB) as shown in Figure 2.9 (b). The flexible PCB is rolled together and secured in a plastic housing to form eight 48-crystal PET rings with a total of 384 crystals, having an ID of 38 mm and an axial extent of 18 mm at the center of FOV. For PET signal readout, a 32-to-1 serial priority encoder is embedded in the ASIC to multiplex timing information and the crystal address of every event through a single digital output. Serialized timing and address information from the ASIC is received and processed on a stand-alone electronic board called the time to digital converter and signal processing module (TSPM). The TSPM board transfers data over two optical fibers to an external peripheral component interconnect (PCI) based data acquisition board [97]. The PET detector has a system clock of 100 MHz on the TSPM board, which is daisy-chained to all the 12 ASICs embedded on the flexible circuit. It has been observed that the PET system clock interferes with multi-harmonic resonances of the MRI's proton frequency (400 MHz), when operating in the magnet. Therefore, the system clock oscillator on the TSPM was modified from 100 MHz to 106 MHz to minimize the interactions due to harmonics. The + 6 V DC power supply (Matsusada) is used to power the system clock. The APDs are powered by applying a bias voltage of approximately 420 V, supplied by high voltage power supplies (Keithley Instruments, model no. 6487). The low voltage and high voltage lines along with a central common ground are carried by a single shielded cable from the power supplies to the PET device.

The PET data acquisition was performed on Windows XP using the LabVIEW interface and the data is written directly to the disk. PET data was acquired in list-mode format. Data processing is done offline and a 3D maximum likelihood expectation maximization (ML-EM)

iterative algorithm was used to reconstruct the PET images [99]. Using the Monte Carlo SIMSET simulation [102] system response matrix, the PET detector FOV is divided into 0.9581 x 0.9581 x 1.149 mm^3 voxels. The images were visualized using acquisition sinogram and image processing (ASIPro) VM microPET analysis software (Concorde Microsystems). The PET data from the phantom and animal studies were reconstructed for 50 to 100 iterations depending on the imaging sample being reconstructed and post-smoothed using a 3D Gaussian filter ranging between 1.5 mm - 1.8 mm full width at half maximum (FWHM). The spatial resolution of the system is limited by the individual crystal dimensions (2.22 mm). The reconstructed image resolution is 1.2 mm FWHM at the center of the FOV and is under 2 mm FWHM towards the edge of the FOV [103]. The PET image generates 33 voxels transaxially and 17 voxels axially (slice thickness of 1.05 mm). The overall system energy resolution is 13 %, coincidence timing resolution is 10 ns and system sensitivity at the center of FOV is 0.27 % [103].

2.5 Design of RF coil for PET/MRI studies in 9.4 T

A standard Bruker MRI birdcage coil which is routinely used for imaging studies at 9.4 T has an OD of 72 mm. This was impractical to use for simultaneous PET/MRI measurements given the geometric design of the PET system (ID/OD = 38 mm/80 mm) and restricted access inside the bore. Therefore, custom-designed volume coils were fabricated in house which fit inside the PET system as shown in Figure 2.10. The ID/OD of the RF coil is 32 mm/37 mm and the coil length is 76 mm with an active axial extent of 27.4 mm. Although, the imaging volume is limited by the geometry of the PET detector ring, it is large enough to center the head of an adult rat inside the active region of the coil. The RF coil consists of two orthogonal Helmholtz pairs, i.e. it is composed of two hexagonal coils built by thin strips of copper as printed traces. These strips are mounted on a cylindrical structure made of G10 material (glass-epoxy laminate). The first coil of each pair is connected to the second by means of a thin PCB trace. Each hexagonal coil is made resonant at 400 MHz by means of discrete capacitors (12.2 pF) mounted in the middle of each side. The coil is tuned to its proton resonance frequency of 400 MHz using variable trimmer capacitors (Voltronics Corporation, NJ) connected to long tuning rods to allow adjustment from the outside once the coil is inserted into the MRI magnet. The RF coil is inserted into the PET detector ring such that the PET and MR imaging volumes are aligned with each other

mechanically to obtain accurate co-registration. The coil is secured in X, Y and Z directions using non-metallic stoppers to avoid rotational movements once inside the PET detector.

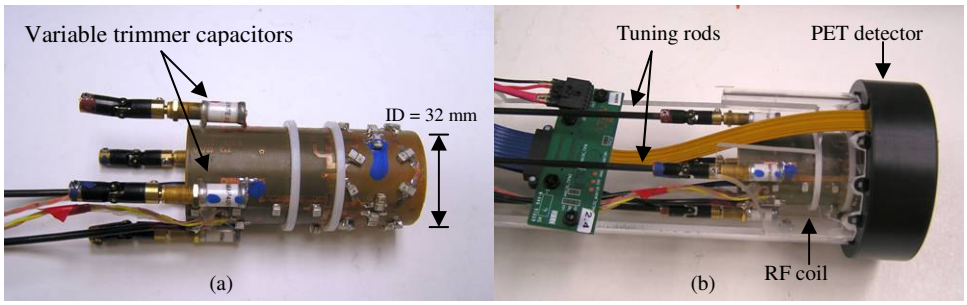

Fig 2.10 Custom-built RF coil. (a) The coil is secured inside the PET device (b) housed in black plastic casing.

2.5.1. Performance of RF coil on the workbench

The performance of the RF coils was tested on the bench using a spectrum/network analyzer (Agilent 4395A). The RF impedance test adapter module is connected to the spectrum analyzer to evaluate the coil input reflection coefficient as a function of frequency. The input reflection coefficient is the same as the S_{11} parameter of the scattering matrix. The reflection coefficient of the coil was measured after configuring the instrument in impedance analyzer mode. As a first step, the RF coil was tuned and matched at 400.32 MHz frequency with no loading. The reflection coefficient on the impedance analyzer is given in milli units (mU). To obtain a good match, the reflection coefficient should be minimal (ideally zero) at the tuned frequency. The tuning and matching of the RF coil was performed as outlined in [104]. The coil is tuned to the desired tuning frequency by varying the tuning trimmer capacitor and then adjusted to obtain the best impedance matching. The tuning and matching are readjusted until the reflection coefficient reaches its minimum at 400.32 MHz.

To measure the efficiency of the reflection loss, a voltage standing wave ratio (VSWR) was calculated. It gives a measure of 'reflected voltage' that is calculated before performing further evaluation on the probes. VSWR is given by

$$VSWR = \frac{1+|\Gamma|}{1-|\Gamma|} = \frac{1+|S_{11}|}{1-|S_{11}|} \quad \text{where}$$

$\Gamma = S_{11}$ = reflection coefficient

The return loss, RL is given by

$$RL = -20\log|\Gamma| \text{ dB}$$

$$RL = -20\log\left(\frac{VSWR-1}{VSWR+1}\right) \text{ dB}$$

Typically, the reflection coefficient ranged between 5 mU to 25 mU for each of the coil pairs. Figure 2.11 shows an overlay of the reflection coefficient plots of the two coil pairs with 'no load' condition, as a function of frequency.

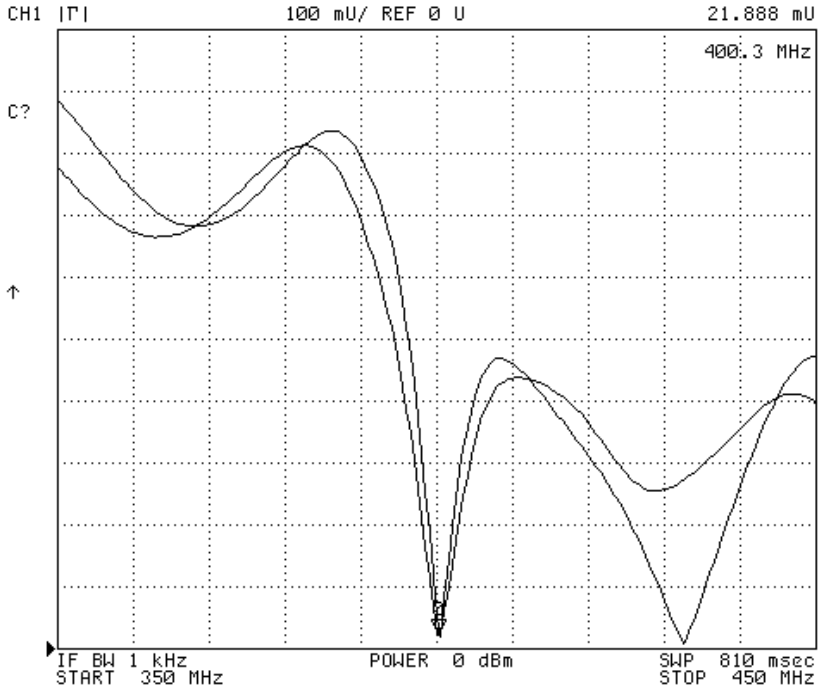

Fig. 2.11. Reflection coefficient curves for the two coil pairs of the custom-built RF coil.

Figure 2.12 shows the return loss corresponding to the reflection coefficient values obtained using the spectrum analyzer. The higher the return loss, the lower the lost power. For example, if the return loss is 20 dB, 1/20th of the incident power is reflected.

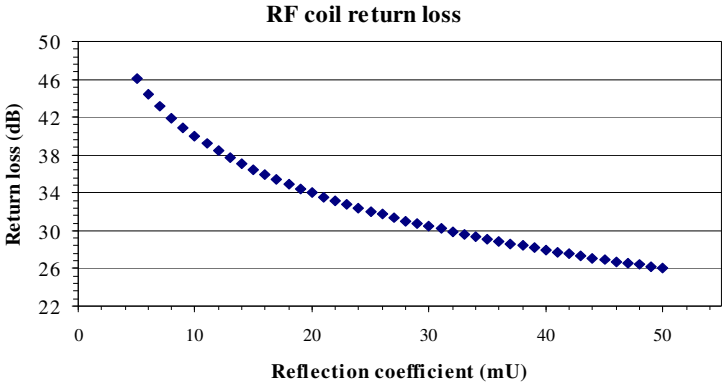

Fig. 2.12. Return loss (dB) of RF coil at 400.32 MHz.

Although the RF coil is equipped with two separate pairs of orthogonal loops, they need to be driven in quadrature mode to operate as a circularly polarized coil. Therefore, the quadrature driving was done by constructing a four-port hybrid device, as described in section 2.3.2. A branch-hybrid network as described in [92] was employed to drive the coil in quadrature mode as shown in figure 2.13. The coil is designed to operate in a fully quadrature transceiver mode by means of a λ/8 hybrid network to attain better signal-to-noise ratio (SNR) in MR images. The reflection coefficient plot with the combiner/splitter is shown in figure 2.14. A higher reflection loss is desired which indicates a close impedance matching resulting in the wider differentiation of powers of transmitted and reflected signals.

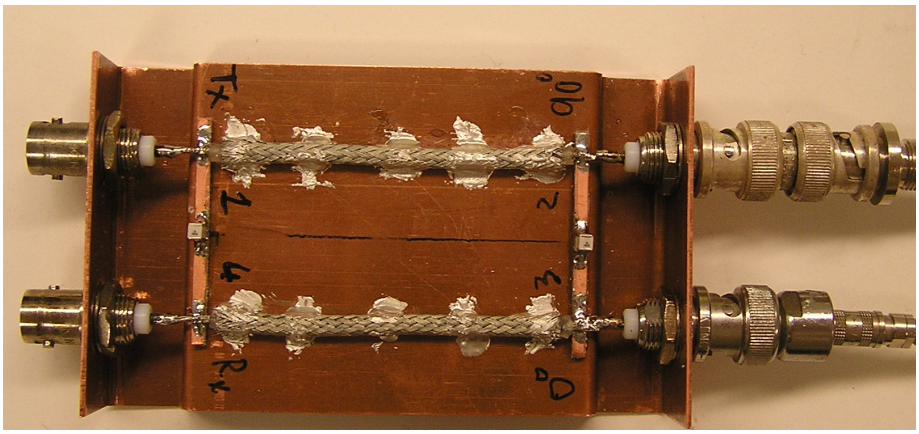

Fig. 2.13. 90^0 branch-hybrid network combiner/splitter used to drive the RF coil in quadrature mode.

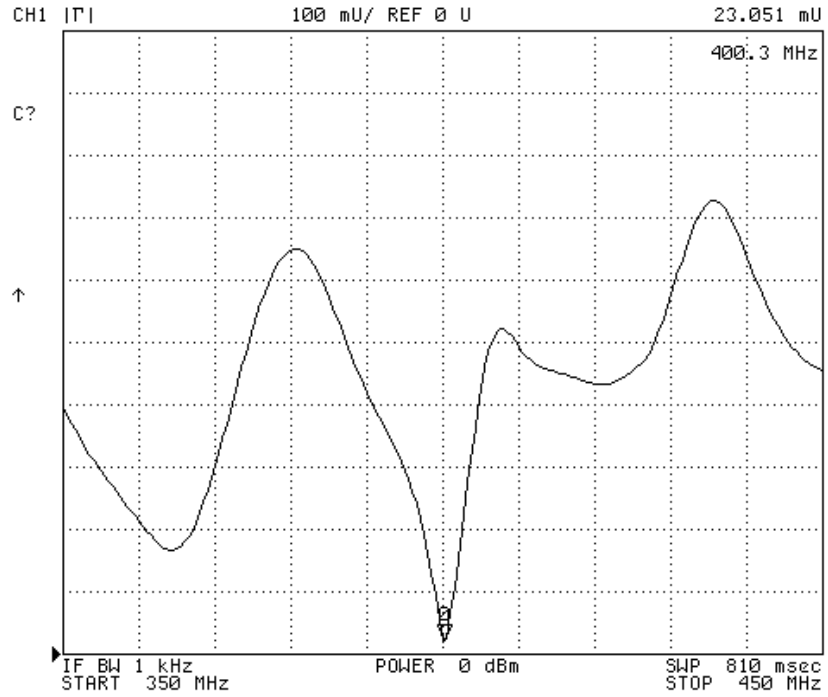

Fig. 2.14. Reflection coefficient curve with the RF coil connected to the combiner/splitter network.

Figure 2.15 demonstrates the advantage of using the RF coil in quadrature mode, compared to the MR image acquisition with individual coils alone. One of the coil-pairs are connected to transmitter or receiver acting as a linearly polarized coils. With each pair of the individual coils, the sensitivity is accentuated only along the direction where the coils are spatially located with minimal signal near the diagonal region opposing it. By connecting the coil-pairs to the combiner/splitter, the MR signal is acquired from both the coil-pairs with signals phase-shifted by 90^0.

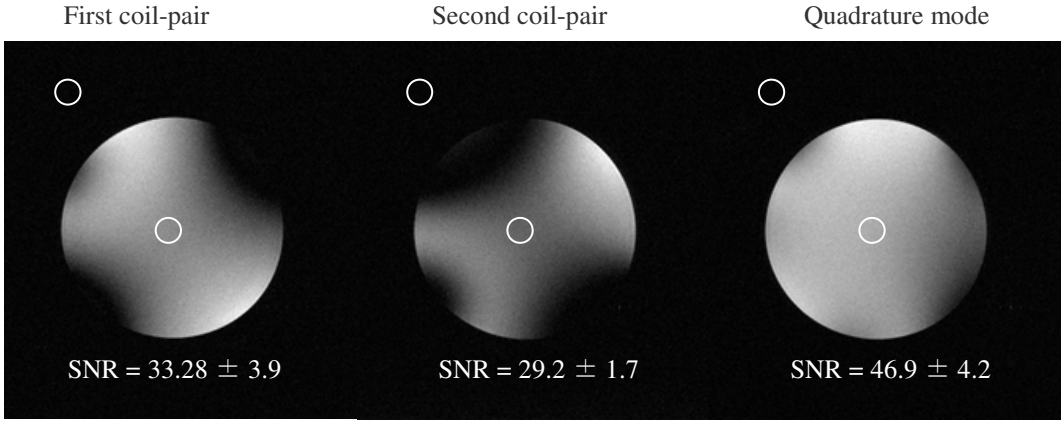

Fig. 2.15. MR images of a cylindrical phantom acquired with individual coil-pairs and in quadrature mode.

Since the RF coils are an example of cross-coil pairs, each of the coil pair was tuned and matched individually. The tuning and matching adjustments were tested for different filling factors. The filling factor is the ratio of the volume of the imaging sample to the volume of the coil. Unlike clinical RF coils, the filling factor is comparatively more for the small animal RF coils. This is a significant distinction between clinical and pre-clinical volume coils. One of the challenging requirements of our custom-built RF coil is to be able to tune and match for both unloaded and completely loaded conditions. For example, in order to image a rat brain or a whole body mouse, the coil volume is loaded to the limit resulting in a decrease in inductance and an increase in the resistive losses, leading to an overall degradation of the Q factor. The extent of degradation is accentuated at high frequency operation. Therefore, the coil was tuned by replacing some of the fixed capacitors with optimum capacitance values. Phantoms with different load variations were used to simulate the load equivalent of a rat head to evaluate the performance of the coil on the workbench. The tunability of the coil was an issue especially when the behavior of the coil pairs mismatch at the center frequency. The components on the both the coil pairs must be balanced in order to achieve a good performance. Our RF coil is an example of a mid-range coil as defined by Doty *et al.* [88]. The product of the center frequency and the coil diameter is 12.8 MHz-m.

2.6 The 9.4 tesla microMRI scanner and PET/MRI experimental setup

We are using a Bruker 9.4 T superconducting horizontal bore magnet (Bruker Biospec 94/20, 400 MHz proton frequency, Magnex scientific) as shown in Figure 2.16, for the PET/MRI acquisitions that has a clear bore diameter of 210 mm. The scanner is controlled by the Bruker Avance console and is equipped with an actively shielded 116 mm diameter gradient set (B-GA12), which is capable of producing a maximum gradient strength of 200 mT/m. The MR images were acquired, reconstructed, visualized and analyzed using the ParaVision software from Bruker Biospin. The 5 Gauss fringe fields extend 2 m radially and 3 m axially in either direction, from the center of the magnet. The MR room is not a Faraday cage and there is no patch panel filtering employed for the PET/MRI scans.

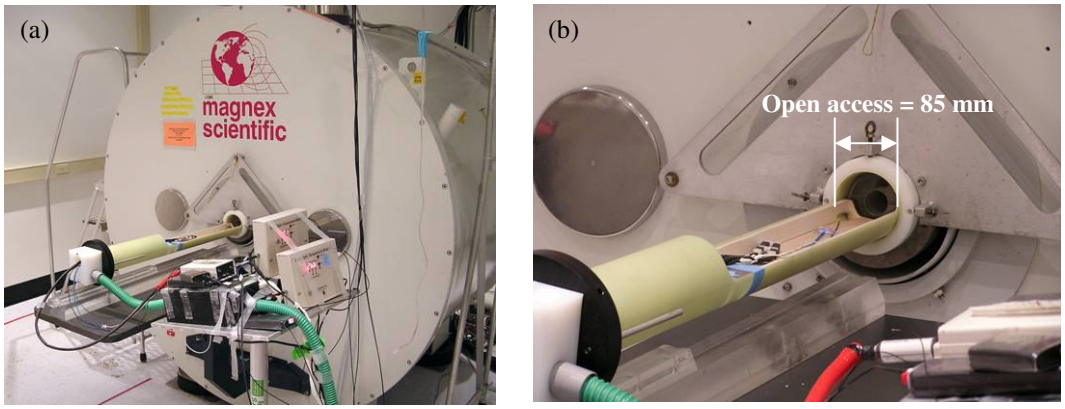

Fig. 2.16. The Bruker Biospin 9.4 T MRI scanner (a) with 85 mm diameter open access (b).

A long support tube (ID = 84 mm) made of G10 extends through the entire bore of the magnet. Two concentric foam liners were used between the gradient set and the support tube to suppress the noise due to the mechanical vibrations, leaving 85 mm open access for imaging. The support tube is secured at both ends of the magnet and is designed to accommodate two tube assemblies made of G10 plastic material as shown in figure 2.17. The first tube assembly is used to secure the RF coil placed inside the PET device and its data cables, which are inserted from the rear end of the magnet bore. The cables are connected to the TSPM board which is secured in a metal enclosure as shown in figure 2.17(a). The second tube assembly is used to position the animal on the animal handling platform and is then guided from the front end of the magnet bore, such that the animal's region of interest and the PET detector are spatially aligned at the homogeneous region of the magnetic field.

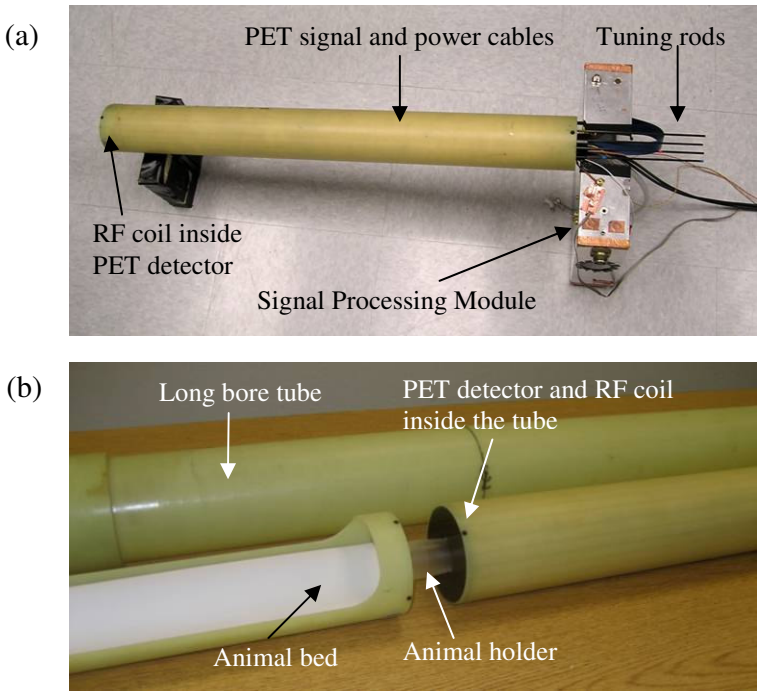

Fig. 2.17. PET/MRI tube assemblies. (a) The RF coil and PET detector are secured in a G10 tube assembly. The data and power cables along with the signal processing module remain at the rear end of the magnet. (b) A second tube assembly with the animal bed is used to position the animal and slides into the first tube. A long bore support tube accommodates both the tube assemblies inside the magnet.

This arrangement helps in abutting and detaching the tubes independent of the PET electronics and is convenient for animal positioning and radiotracer administration. All the PET power supplies are well outside the MRI room during the scans. Figure 2.18 shows the schematic of the PET/MRI setup in the 9.4 T magnet.

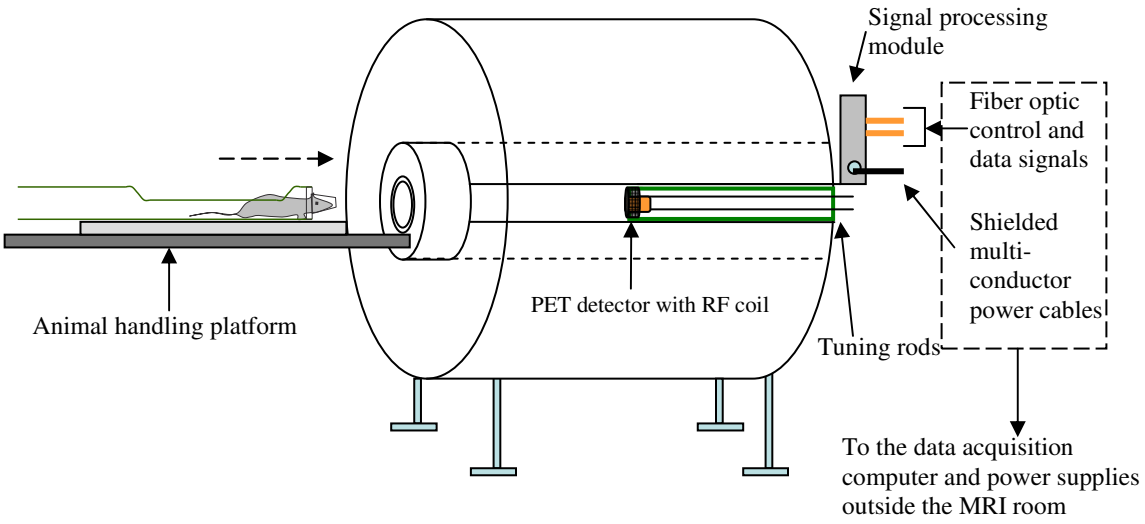

Fig 2.18. Schematic of PET/MRI acquisition setup in a 9.4 T Bruker Biospin microMRI scanner. The RF coil secured inside the PET detector is placed at the isocenter of the magnet. The imaging sample is positioned on the animal handling platform which is slid from the front of the magnet abutting the tube encapsulated by the PET detector and the RF coil.

2.7. Chapter summary

In this chapter, some of the basic principles and components of an MRI system were presented. In addition, the basics of the RF coil design were discussed to help in understanding the specific design and construction of the small animal RF coils. The advantage of quadrature driving in the volume coils has been highlighted to obtain better SNR in the MR images compared to linearly polarized coils. RF coils were constructed specifically for performing simultaneous PET/MRI studies. The coils were tested on the workbench before the MRI acquisition. A brief overview of the PET system based on RatCAP and its integration in a Bruker 9.4 T MRI scanner was presented. The next chapter presents some of the initial experiments performed using the unshielded PET system inside MRI scanner.

CHAPTER 3: ELECTROMAGNETIC INTERACTIONS DURING SIMULTANEOUS PET/MRI OPERATION: OBSERVATIONS

In this chapter, the impact of the electromagnetic interactions between the unshielded PET detector and the MRI scanner is discussed. Specifically, identifying the source(s) of interference between the PET and MRI systems affecting the simultaneous operation is addressed. In the following sections, the impact on the MR image quality in the presence of unshielded PET system is described, followed by the impact on the PET electronics during active MRI acquisition with different MR pulse sequences.

3.1 Identifying the electromagnetic interference

During conventional MRI scans, no metallic objects are allowed inside the magnet bore for safety reasons. Patients with studs, tattoos and medical implants containing metallic traces or electronic circuitry near or at the imaging region of interest are generally not allowed to undergo MRI scans. This is because the B_0 field is compromised due to the coupling of the field lines with any metallic or ferromagnetic structures in the field. Although MRI-safe devices are being developed and investigated [105], at present it is hazardous for patients with medical implants as they may malfunction during the MRI scans,. When integrating the PET and MRI systems, there is a potential for interference in either system during active mode of operation. The possible sources of electromagnetic interactions are described in the following subsections.

3.1.1 Effect on MR image quality due to the presence of powered PET

Introducing even traces of ferromagnetic materials inside the bore of any MRI scanner is undesirable. As mentioned in previous chapter, newer versions of the MRI systems have a superconducting magnet, a gradient coil set and a radio frequency (RF) system. The main magnetic field B_0 must be homogeneous at the isocenter of the magnet bore. The gradient coils create intentional magnetic field variations (in the order of few mT) in the X, Y and Z directions for spatial encoding. The RF system is used to excite the imaging sample and receive an MR signal. The following are some of the impending issues due to the presence of a powered PET detector that can significantly affect the MR images:

B_0 inhomogeneities: When a patient is positioned inside the MRI bore, the field lines interfere and disturb the homogeneous region at the isocenter. This is because the body acts as a conductor with different organs having different tissue densities. First and second order shimming are generally employed to compensate for the distortions in the field. The presence of any metallic objects in the PET can disturb the B_0 field leading to distorted MR images. When the PET detector is powered, there is a possibility that the unshielded current carrying power cables (if laid parallel to the B_0 field) may create local magnetic fields perpendicular to the B_0 field, enhancing the electromagnetic coupling. It is important to maintain a higher degree of B_0 homogeneity during PET/MRI studies in order to perform advanced MR functional studies (fMRI) and MR spectroscopy.

MR Artifacts: The electronic components in the PET detector have the ability to radiate electromagnetic noise at high frequencies. As an example, if the clock used to time the events in the electronics has a square wave function, it may contain significant energy at high frequencies and therefore may generate noise. If these high frequencies are multiple harmonics of the MRI proton frequency, then they may interact with the MR signal and make their way into the MR frequency encoding steps resulting in interference artifacts in the MR images.

During MRI acquisition, the fast-switching time-varying gradient fields induce local currents on the surface of the metallic conductors, according to Faraday's laws of induction. These currents, known as *Eddy Currents,* in turn produce reverse electromagnetic (EM) fields that interfere with the B_0 field and the gradients. If the gradient fields are disrupted, the slew rate (the rise time of the gradients) and the gradients strength that is required to spatially encode the position of the imaging sample will be compromised. Particularly, if the decay rate of the gradient fields is slow, the residual fields contribute towards MR image read-out leading to image distortions [106]. Depending on the bore diameter, gradient strength and the overall geometry of the MRI system, the presence of the PET electronics or any conductive layers at the isocenter in the bore may cause significant image distortions during rapidly changing gradients leading to susceptibility artifacts and loss in the MR signal. Not only the MR imaging is affected, the off-resonance frequency shifts the MR spectrum after Fourier analysis compromises the MR spectroscopy studies [107].

RF inhomogeneities: The RF system consists of RF transceiver coil. Depending on the imaging sequence, the coil is generally optimized to excite the imaging sample by applying an external

magnetic field B_1 and receiving a maximum signal back. As discussed in Chapter 2, the RF coil is designed and constructed in order to couple with the imaging sample with minimal resistive losses or compromise on the quality factor (Q) of the coil. This allows the coil to flip the nuclear magnetization of the protons efficiently to maximize the reception of the MR signal. If the PET detector electronics containing ferromagnetic components are placed near the RF coil, it changes the effective coil inductance as the coil interacts with the conductors intercepting the B_1 field. This can result in coil detuning, impedance mismatch and a lower Q factor, leading to inefficient excitation of RF in the imaging sample. The transmitted RF energy becomes inefficient because the coupling between the RF coil and the PET detector electronics becomes predominant. To be precise, each RF pulse in a sequence is optimized to a particular flip angle. If the RF field distribution is non-uniform, the flip angles become irregular near the imaging volume leading to MR signal variations or loss of the signal. The RF energy deposition is compromised at higher frequencies and the inhomogeneous RF excitation is reflected and extends farther away from the imaging volume [108].

To compensate for the signal loss, a large number of signal averages are required which in turn increases the acquisition time. This would result in unnecessary dissipation of RF heat into the imaging sample. There could be complete signal dropout in the MR images due to the close proximity of metallic components or housing near the imaging volume [45]. Inefficient excitation of proton spins may also result in uneven signal intensities and non-uniform patterns in the MR images. Non-uniformities in the B_1 field have a negative impact on not only the imaging, but also during the spectroscopy and echo planar imaging studies.

Temperature fluctuations: Drifts in temperature can also affect the MR acquisition performance when advance MR techniques such as longitudinal fMRI studies are performed, which requires good temporal stability [109].

In summary, all of the above factors may contribute to the image distortions, susceptibility artifacts and overall signal loss in the MR images during the active operation of the PET system inside the MRI scanner. The degree of degradation in MR images may be more pronounced during PET acquisition as the power cables (if unshielded) may act as conductors carrying noise currents in the MR bore.

3.1.2 Effect on PET performance during MRI acquisition

The technical challenges involved in integrating the PET system inside the MRI scanner were described in Chapter 1, section 1.4. The introduction of magnetic insensitive APDs as a better alternative to PMTs in the design of MRI-compatible PET systems helped improve the overall performance of the PET. However, the influence of electromagnetic fields on the photodetectors cannot be underestimated. The interference effects on the PET electronics are directly dependent on the signal read-out design, architecture and geometry of the PET device. Therefore, the interaction mechanisms may vary accordingly. Following are some of the potential effects on the PET system during MRI acquisition:

Effect of gradients: The rapidly-switching gradients in operation during the MRI scan may induce currents on the PET detector electronics. There has been some evidence of interactions due to the gradients in the literature where the apparent rate of PET events decreased [49], during the simultaneous PET/MRI operation.

Effect of RF: Depending on the proximity of the RF coil to the PET detector, the PET electronics may experience strong RF bursts. These bursts can interact with the PET photodetectors, preamplifiers and the rest of the front-end electronics. The RF pulses generated by the alternating currents in the coil may be easily picked up by the PET signal clocks, disrupting the time arrival of the detected PET events. Also, they may induce noise transients and ripples on the PET digital output signals that might eventually corrupt the PET data. There is a possibility that the high power RF energy can completely paralyze the PET signal read-out, leaving the electronics in an inoperable state.

Vibrations: The mechanical vibrations due to the gradient fields can lead to misinterpretation of the PET images compromising the spatial accuracy during the PET/MRI co-registration. Because of the recurrent movements of the PET system inside the magnet bore, there is a possibility of alterations in the RF coil tuning/matching setup.

Temperature: Any changes in the temperature inside the PET electronics can degrade the PET performance, especially if the PET photodetectors are temperature-sensitive. A high intensity RF pulse sequence has the potential to generate heat near the conductive components of the PET detectors leading to misinterpretation of sensitivity measurements in the PET data.

Slates *et al.* first reported a study of artifacts on the MR images in the presence of PET [35]. Other research groups also presented detailed effects of PET detector on the MR images [45, 49, 83]. Effects due to the gradient fields on the PET inserts were reported with APD-based

photodetectors [49]. A recent article on the performance of SiPMs during MRI acquisition revealed some interference due to high intensity RF pulsing [61]. Some of the current challenges encountered by different research groups while acquiring simultaneous PET/MRI data were discussed in PET/MRI workshops [67]. The following section describes some of the test results using unshielded RatCAP PET device in the MRI scanner.

3.2 Observations of the Electromagnetic Interactions with the Unshielded RatCAP PET detector inside Bruker 9.4 T scanner

The simultaneous PET and MRI data was acquired after setting up the unshielded PET system inside the MRI bore, as described in section 2.6. The following subsections describe the impact of one system that can have on the other during simultaneous PET/MRI operation.

3.2.1 The effect of unshielded PET detector on MR images

The main goal of the test was to observe any visual distortions or artifacts on the MR images using our unshielded PET detector. The MR images were acquired with the PET system inside the MRI bore with vs. without powering the electronics. MR images were acquired with a cylindrical phantom with an inner diameter (ID) of 28 mm filled with water. A rapid acquisition with relaxation enhancement (RARE) spin echo pulse sequence (repetition time (TR) = 2500 ms; echo time (TE) = 9.8 ms; field-of-view = 30 x 30 mm^2; Matrix size = 256 x 256) was used for the scans. With the PET OFF condition, there were no visible artifacts on the MR images of the phantom. The PET system electronics were then turned ON. As a result, there was an interference spike observed close to the center frequency of the MRI (400.32 MHz) as shown in figure 3.1.

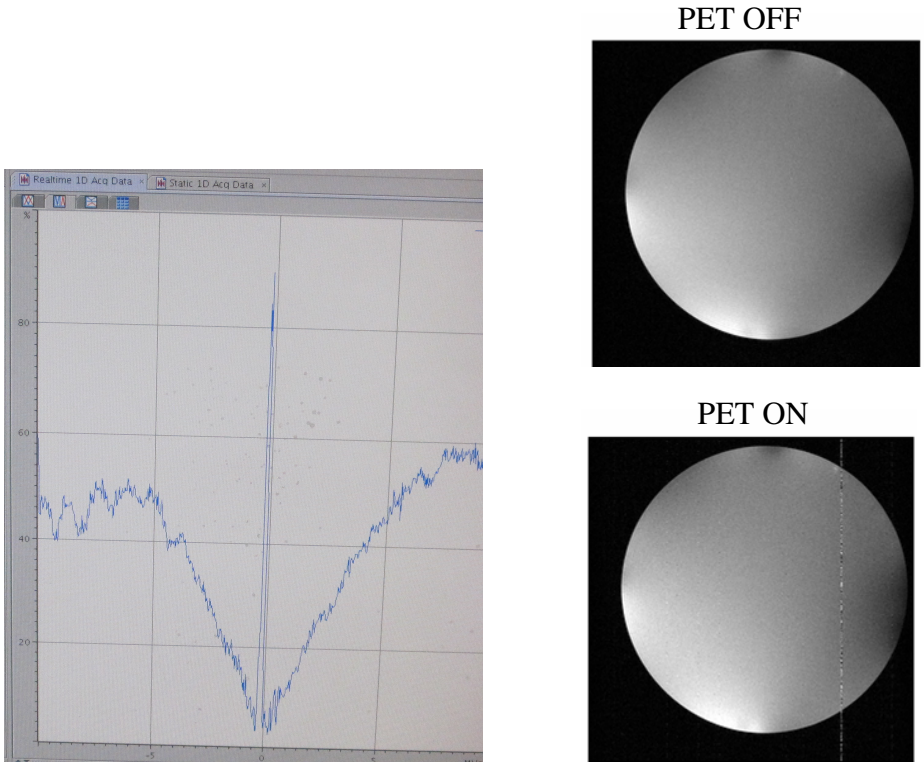

Fig. 3.1. Interference on the MR signal. Spike on the return-loss plot of the MR signal (left) and interference on phantom images with the powered PET condition (right).

There was no offset in the RF coil tuning or matching when the PET system was turned ON. The MR images were acquired by repeating the same MR scanning parameters. A line artifact is observed on all the images during the PET ON condition, as shown in figure 3.1. The line interference on the MR images due to the PET detector electronics is an example of the MR artifacts as described in section 2.1.1 and is well within the receiver bandwidth of the MR signal acquisition. The signal-to-noise ratio (SNR) of the acquired MR images was measured using ImageJ MR image processing tool. A small region-of-interest (ROI) was placed on the phantom and a second ROI in the background outside the phantom across all planes to measure signal and noise values, respectively. The SNR for each of the PET conditions was computed by averaging the ratio of mean and standard deviation, across all the slices. The SNR across all slices with the PET OFF and powered PET conditions is calculated to be 61.4 ± 4 and 51.2 ± 4, respectively. Figure 3.2 shows MR images of the rat brain acquired using RARE sequence where the line interference is seen in all the three orthogonal planes.

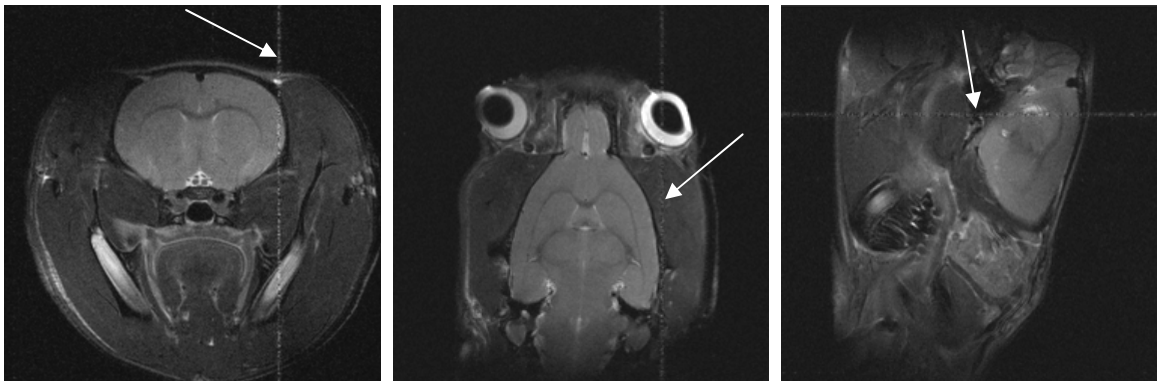

Fig. 3.2. MR images of a rat brain with the line interference during the powered PET condition; in transverse (left), coronal (center) and sagittal (right) planes.

3.2.2 Effect of MRI on PET detector

Gradient and RF excitation pulses were used in the presence of PET detector acquiring phantom data as mentioned above. Fast low-angle shot (FLASH) gradient echo and RARE sequences were acquired during active PET operation. The effect on the PET data due to gradients and RF was recorded independently, by probing the analog output of a single PET channel using a digital oscilloscope (Tektronix TDS7254B). When the gradients were applied individually (X, Y and Z) and all together independent of RF pulses, there was no change in the PET count rate. Also, no degradation was observed in the analog output pulse shape of the PET signals from the oscilloscope measurements. Figure 3.3 shows the scope shot of the bipolar analog output from a single PET channel with no gradients and with all the gradients turned ON.

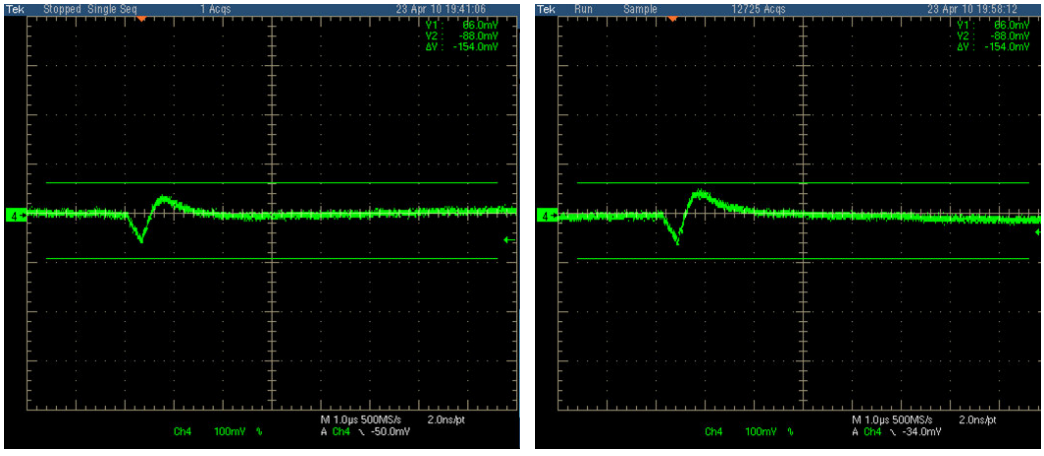

Fig. 3.3. Scopeshots of the PET analog output. (a) Analog output of a single PET channel inside the magnet bore during MR OFF condition. (b) Analog output during RF OFF and gradients ON condition. ***Note:*** The negative swing of the analog signal is ~ -580 mV from the baseline, when probed using the scope probe on the workbench at the tether of the PET detector. Since the probe points are practically not reachable when the PET is configured inside the magnet, the signals are probed using coaxial cable that was soldered to the analog input pads. The coaxial cable could not drive the signal due to the long length, saturating the signal at ~ -80 mV.

On the other hand, the effect of RF excitation on the unshielded PET detector was observed. Figure 3.4 shows the scope shot of the analog output during the RF pulsing. The analog signal is corrupted during the RF pulses.

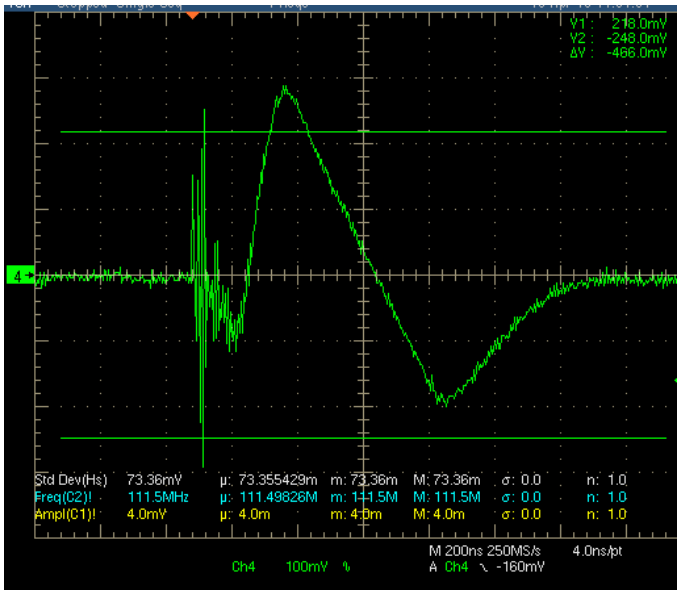

Fig. 3.4. Analog output of a single PET channel inside the magnet bore that was susceptible to the RF pulsing.

The steady PET event rate during RF OFF condition increased rapidly when the RF is turned ON. This sudden increase in the event rate occurs only during the active duty cycle of the RF pulse sequence. When the list-mode PET events were histogrammed into millisecond time bins, the spurious counts were seen as spikes that correspond to the RF pulse duration and time intervals of the imaging sequence. Figure 3.5 shows the list-mode data counts during gradient echo and spin echo sequences. The magnitude of these spurious counts (seen as spikes in the count rate) was higher for spin echo sequences compared to gradient echo sequences.

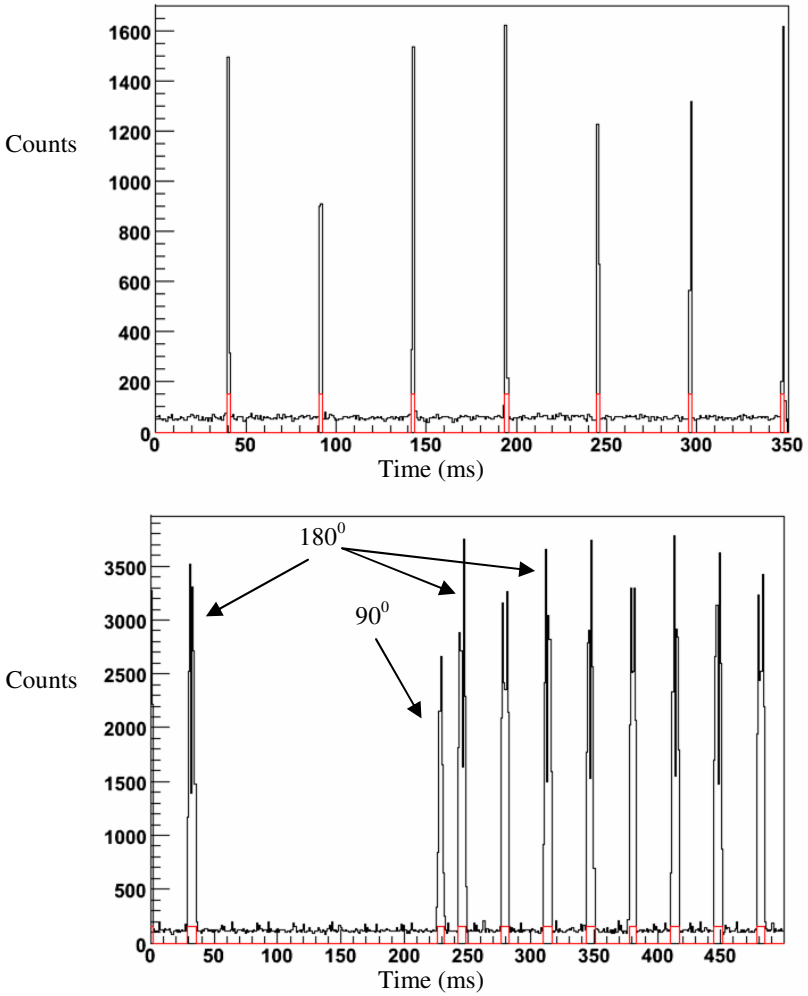

Fig. 3.5. Spurious counts seen as spikes in the list-mode PET data that correspond to the RF pulsing in FLASH gradient echo sequence (top) and RARE spin echo sequence with the spikes corresponding to one 90^0 pulse and eight 180^0 pulses (bottom). The magnitude of 90^0 spike is smaller compared to 180^0 spikes.

Another contribution to the corruption of PET data is low-magnitude spikes occurring at regular time periods. These spikes are a result of high inductances on the power cables and are independent of RF pulsing. Figure 3.6 shows the spikes in the PET data along with the RF pulsing. A potential difference of over 120 mV was observed between the shield ground and the signal returns near the power supplies and can lead to imbalances in the signal returns creating ground loops. The power cables extend over 10 meters from the power supplies stationed outside the MRI room to the center of the magnet and were susceptible to noise currents. This is because the cables can act as antennas if their length is longer than half wavelength at a given operating frequency [110]. At 400 MHz, the wavelength is 75 cm.

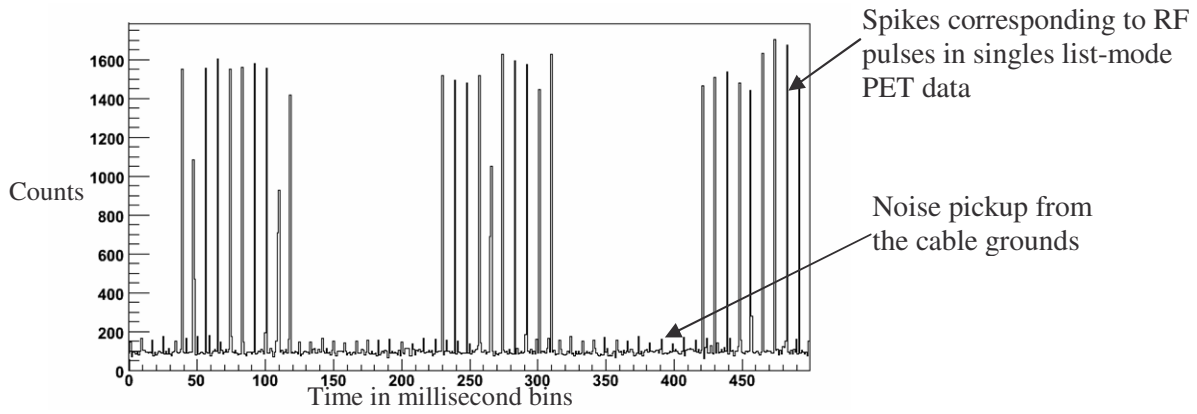

Fig. 3.6. Low-magnitude spurious counts were observed as a result of noise on the .power cables, in addition to the interference due to the RF pulsing.

Since the PET read-out electronics are in close proximity to the RF coil, it is believed that the strong RF excitation pulses inject significant charge into the read-out electronics. There is a possibility that the charge sensitive pre-amplifiers (CSPs) in the front-end electronics [96] may easily pick up the RF noise thereby triggering false counts incessantly during the duration of the RF pulse, which will appear as spurious spikes in the PET list-mode data. However, it is clearly evident that the PET read-out reverts back to its normal acquisition mode between RF pulses. The time bins where the noisy RF spikes occur were gated out by setting an appropriate count rate threshold, above which the data acquired during the RF spikes were discarded, as shown in figure 3.7. This resulted in a dead-time that corresponds to the RF duty cycle of the sequence. For FLASH sequences for example, the RF pulse duration is 1 ms and the repetition time is 16 ms per slice. This led to a loss of 6.25 % of the PET counts after gating out the RF spikes. For RARE sequences with the 8 refocusing pulses, it is 16 % to 28 %, depending on the RF pulse duration, which ranged between 2 ms to 4 ms and is also dependent on the number of slices acquired (more slices implies a higher RF duty cycle).

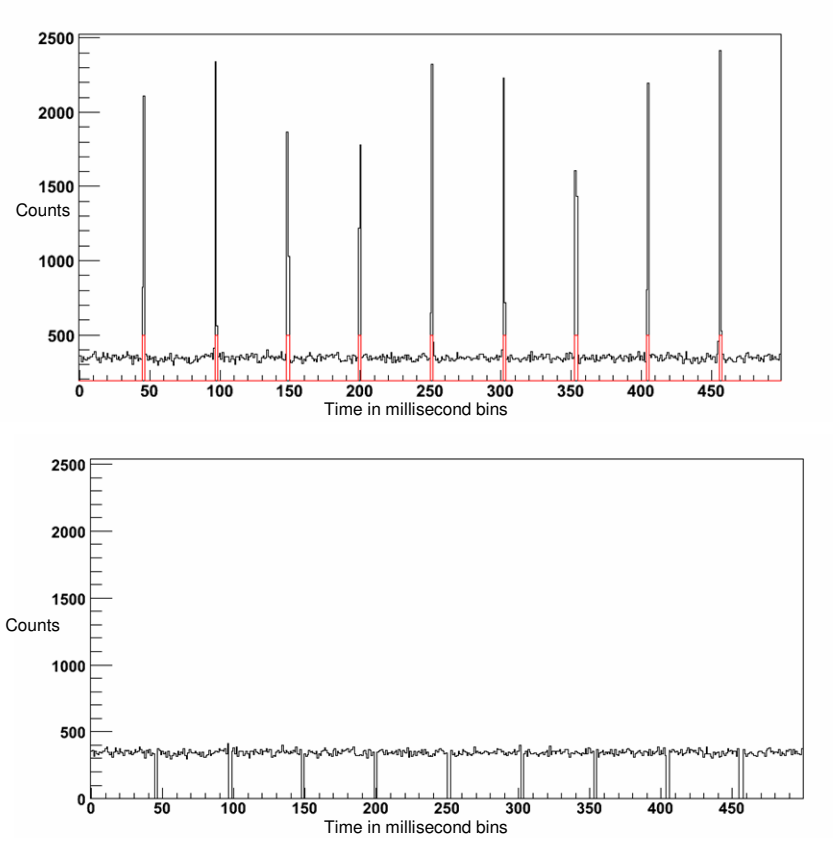

Fig. 3.7. RF gating during PET offline processing. The counts acquired during the RF intervals (top) are gated out (bottom) by selecting an appropriate threshold.

Although the spurious counts can be gated out during post-processing of the PET data, the impact of RF excitation was significant enough to temporarily block out all the PET counts in some susceptible PET channels. Depending on the pulse sequence and the RF power optimized for a particular flip angle, some of the channels had spurious activity with a large number of PET counts during the RF pulsing. By the end of the imaging sequence, no counts were recorded in the PET channels and they temporarily appeared to be dead during the PET acquisition. There were less than 10 % of the channels that did not record any PET counts at the end of the FLASH gradient-echo sequences and at least 30 % of the channels for the RARE spin-echo sequences, respectively. The susceptible PET channels stayed in an inoperable state until a system reset was performed.

3.3 Discussion

From the MR image quality tests, the drop in the SNR (by approximately 16 %) was evident when the PET system was powered. The PET power cables were shielded from the power supplies to the signal processing module (TSPM) box. The cables from the TSPM to the RatCAP flex were exposed and were not shielded, although they were enclosed in a tube assembly with a copper sheet on the inside, connected with a pigtail. The interference on the MR images indicate that the PET power cables could be a source of conducting EMI, which is picked up by the RF coil circuitry as noise. The spike on the return-loss plot of the MR signal is due to this RF pickup noise, especially if the MRI's proton frequency is within the range of the PET system clock or its harmonics. The line artifact on the MR images was observed after the PET system clock was powered by the low voltage supply. There were no additional artifacts on the MR images when the high voltage supplies were turned ON.

On the other hand, the interaction of RF with the PET electronics had a significant negative impact on the PET data acquisition, temporarily paralyzing the ability to record events in some of the PET channels. The RF coil is the main radiating element that is believed to be causing the noisy transients creeping into the PET front-end electronics. Spurious spikes in the PET data corresponded to the RF duty cycle. The magnitude of these spikes during RARE pulse acquisition is less for the 90^0 pulse than for the 180^0 refocusing pulse. This is indicative of the fact that it takes less RF power to flip the protons to 90^0 than to 180^0. The effect of RF interference on PET increases the amount of unwanted data written to the disk. None of the literature has indicated the effect of RF interference on PET inserts, though the effect due to the gradient switching has been reported [49]. One possible explanation could be that the sensitive detector readout electronics for other PET/MRI systems reside farther from the MRI FOV, and are therefore not influenced to the same extent. Other factors such as the use of optical fiber bundles, different readout design, scanner geometry, MR pulse acquisition protocols and placement of PET detector shielding may also help explain this difference compared to our system. One of the reasons there is no metallic shielding around the PET detectors in our system is that we want to obtain MR images with minimal attenuation of the RF power, as the shielded metallic enclosure in our previous PET/MRI work performed in 4 T MRI resulted in a significant reduction in SNR and required increasing the power levels of the RF amplifiers [111]. Since the PET detector is unshielded, the front-end electronics are vulnerable to the strong RF bursts. Also,

the close proximity of the PET electronics to the RF coil (within 20 mm) contributes to significant absorption of RF energy into the PET electronics, corrupting the read-out signals.

In addition, the noise pickup on the cables (independent of RF pulsing) due to the ground loops added another source of interference in the PET data. This is because of high impedance (high inductance in the ground path) on the power cables carrying the signal returns leading to more ground loops. A large potential difference between the signal returns and the chassis ground would induce loop currents and interfere with the signal. The electromagnetic radiation becomes significant depending on the ground loop area, the current and the frequency of operation. Long cables at high frequencies do not always provide the path of least impedance due to the inductive reactance components on the cables. If the signal returns do not find a least impedance path to ground, a huge potential difference may be developed due to the imbalance of the grounds in the circuit. The different types of coupling mechanisms and the path of interference must be identified to minimize the EMI during the PET/MRI acquisition.

All the above studies and observations indicate the need for employing suitable shielding and grounding approaches. Some of the shielding techniques can be used to minimize the effect due to the RF on the PET electronics. It may be argued that gating the RF pulses in the PET data in the offline processing may be used, instead of employing shielding methods. However, the fact that there has been a decrease in the count rate statistics and some of the PET channels are left in an unresponsive state makes it very advantageous to have shielding to remove or minimize the false counts in the PET system. With electromagnetic shielding, the effect of the RF can be minimized extensively [61]. A complete Faraday cage around the PET detector without any imperfections would be ideal to isolate the radiation due to the RF fields. There is a trade-off while choosing the shielding for PET electronics so as to not affect the MR images. The shield placed in close proximity of the RF coil may decrease the inductance of the coil. Therefore, different values on the distributed capacitors of the RF coil are required to compensate for the changes in the shield. The shielding and grounding configuration must be implemented in order to acquire the PET/MRI data with minimal compromises in the performance of either system.

3.4 Chapter Summary

The different sources of EMI during the PET/MRI acquisition were discussed in general in this chapter along with the impact of the unshielded RatCAP PET detector inside the Bruker 9.4 T MRI scanner. Some of the observations are summarized below:

- The effect on the MR images is in major part due to the PET system clock or its harmonics interfering with the MRI fundamental frequency. In addition, the power cables were unshielded with incomplete ground terminations, which resulted in ground loops in the system. Appropriate shielding around the PET signal processing module and grounding can confine the RF pickup and minimize the effect on the MR images due to the PET cables.
- The effect on the PET data due to MR pulsing is mainly due to the RF fields and not gradient fields.
- Some of the PET channels were knocked out during RF excitation. By implementing the shielding around the PET device it should be possible to suppress the effect of RF. By minimizing the loop areas, the inductive coupling between different circuits can be reduced.

The following chapter will focus on some of the shielding and grounding approaches to suppress EMI during PET/MRI studies.

CHAPTER 4: SHIELDING AND GROUNDING TO SUPPRESS EMI: AN OVERVIEW

From the observations described in Chapter 3, clearly the radio frequency (RF) excitation pulses interfere with the direct current (DC) power and signal lines of the PET system. In addition, if the PET power cables are not grounded correctly, emissions from these lines can be picked up by the RF coil and this can lead to the line artifacts in the MR images. An introduction to the electromagnetic (EM) shielding and its effect on the MR images, along with grounding approaches are discussed in this chapter. The following sections mainly focus on the overview of shielding theory and grounding arrangements to suppress the RF currents in the digital circuits.

4.1 Shielding Effectiveness

A parameter that is generally used to describe the reduction in electric and/or magnetic field intensity caused by the shield [110] is called the Shielding Effectiveness (SE). It is defined by IEEE 299 [112] and is usually expressed as attenuation in decibels (dB). A decibel is a logarithmic unit expressing the ratio of two quantities (e.g. power, voltage or current levels, field strengths etc.). Since the dynamic range of these quantities can be quite large, decibels are a convenient method for expressing these ratios and is commonly used in EM theory. For magnetic field, shielding effectiveness is defined as

$$SE_{(H,dB)} = 20\log\left|\frac{H_0}{H_1}\right| \text{ dB, where}$$

H_0 = incident magnetic field strength

H_1 = transmitted magnetic field strength

For electric field, shielding effectiveness is

$$SE_{(E,dB)} = 20\log\left|\frac{E_0}{E_1}\right| \text{ dB, where}$$

E_0 = incident electric field strength

E_1 = transmitted electric field strength

In general, EM shielding and solid ground-planes are employed to minimize the effect of EMI in many electronic systems. The EM shields inhibit the propagation of EM fields into the electronic device that needs protection from the outside fields. They can also confine the EMI

interference within the EM source and prevent the fields from getting out of the devices. The efficacy of the shield depends on factors such as

- the characteristics of the shield material,
- the dielectric permittivity,
- the magnetic permeability, and
- the electric conductivity of the material.

Other important factors are the frequency of the external RF or EM field being attenuated, the type of source (electric or magnetic), the geometry of the shield and the direction of incidence and polarization [113]. As an EM wave strikes the surface of the shield (considering the shielding geometry to be a plane sheet of metal), it is partially reflected from the surface and is partially transmitted into the medium and attenuated further as it passes through, as shown in figure 4.1.

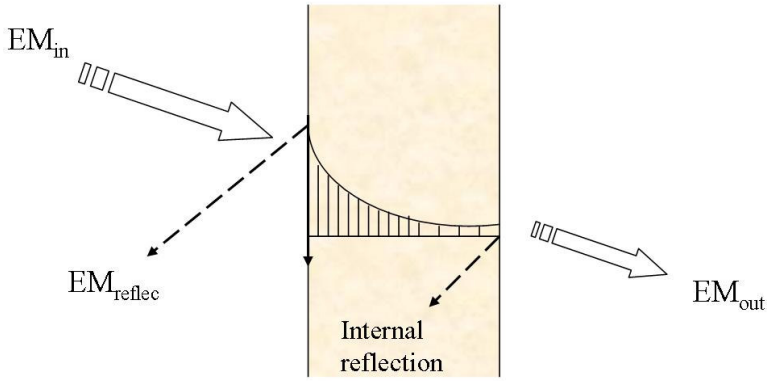

Fig. 4.1. Illustration of the shielding effectiveness of a shield to an incident EM wave.

The EM wave incident on the shield material is attenuated exponentially. Depending on the characteristics of the shield material, the EM wave is absorbed within the shield. This attenuation process is called absorption or penetration loss and the reflection is called reflection loss. The sum of absorption and reflection losses along with the multiple reflection factor defines the total shielding effectiveness (SE) in dB [114],

$$SE_{(dB)} = A_{(dB)} + R_{(dB)} + M_{(dB)}$$

where A represents attenuation loss, R is the reflection loss caused by reflections at both ends of the shield and M is the result of multiple reflections and transmissions within the shield. This parameter M can be ignored if the shield thickness is greater than the skin depth. The following sub-sections describe the influence of these parameters.

4.1.1 Reflection loss

The Reflection loss depends on the impedance mismatch between the incident EM/RF wave and the shield surface. The attenuation due to the reflection of an EM wave at normal incidence to the shield material, is given by [113]:

$$R = 20\log\frac{|Z_w|}{4|Z_s|} \text{ [dB]} \qquad \text{where,}$$

Z_ω = EM wave impedance

Z_s = EM characteristic impedance or shield impedance of the material

The shield material with high conductivity would have a low shield impedance Z_s. the conductivity takes place only near the surface of the shield material due to the skin depth. Hence the thickness of the material becomes redundant for reflective shielding.

The wave impedance Z_ω is the ratio of electric field and magnetic field (E/H). In a far-field, the EM wave is a plane wave with an impedance of 377 Ω. The general formula for characteristic shield impedance is given by

$$|Z_s| = 3.68 * 10^{-7} * \sqrt{\frac{\mu_r}{\sigma_r} * f} \qquad \text{where,}$$

μ_r = relative permeability of the shield (= 1 for copper)

σ_r = relative conductivity of the shield (= 1 for copper)

At 400 MHz, the shield impedance for copper is

$$|Z_s| = 3.68 * 10^{-7} * \sqrt{\frac{1}{1} * 4 * 10^8} \quad = 0.007\ \Omega$$

Therefore, the reflection loss for a plane wave in far-field condition is $R = 20\log\frac{|Z_w|}{4|Z_s|}$ dB

$$R = 20\log\frac{377\Omega}{4*0.007\Omega} = 82 \text{ dB}.$$

Near-field conditions:

In the near field scenario, the distance of the shield material from the EM source is less than $\lambda/2\pi$. The ratio $\lambda/2\pi$ is the boundary between near-field and far-field conditions. In the very near-field condition of a EM radiating circuit (i.e. distance << $\lambda/2\pi$), the wave impedance deviates from that of a plane wave and becomes the impedance of the EM source circuit. If that impedance is below the impedance of free space (377 Ω), the wave impedance Z_ω is considered a low impedance parameter, or predominately magnetic. If it is above 377 Ω, then it is considered a high impedance parameter and predominantly electric. It depends on the nature of the source (electric or magnetic) and distance from the source. A dipole antenna for example, is a high impedance circuit, so Z_ω is high. As the distance between the EM source and the shield is increased, Z_ω decreases and approaches 377 Ω. On the other hand, a small loop antenna is a low impedance circuit, so Z_ω is low. With the increase in distance, Z_ω increases and converges to 377 Ω. Figure 4.2 shows

The wave impedance in a near field (r << $\lambda/2\pi$) is given by [113]

$$|Z_\omega| = 2\pi f\mu r \quad \text{where,}$$

r = distance from the source to the shield in meters.

Substituting Z_ω value in reflection loss,

$$R = 20\log\frac{2\pi f\mu r}{4|Z_s|} \text{ dB}$$

Substituting free space value for μ and Z_s, the reflection loss in near fields become,

$$R = 14.6 + 10\log\left(\frac{fr^2\sigma_r}{\mu_r}\right) \text{ dB}$$

Table 4.1. shows the shielding characteristics for different sources.

Table 4.1. Shielding characteristics [115]

Source	Wave Impedance	Reflection
Plane wave	377 Ω	High
Electric source	High	High
Magnetic source	Low	Low

4.1.2 Absorption loss $A_{(dB)}$

Unlike, reflection loss, absorption loss does not depend on the nature of the source. It depends on the frequency. As the EM wave penetrates the shield, its amplitude decreases exponentially, due to the induction of currents in the shield leading to ohmic losses and heating of the material [113]. Therefore,

$$H_1 = H_0 e^{(-t/\delta)} \text{ and } E_1 = E_0 e^{(-t/\delta)} \text{ where,}$$

H_0 (E_0) = incident EM wave intensity

H_1 (E_1) = transmitted EM wave intensity

t = distance traveled by H_1(E_1) within the shield

δ = skin depth

The above equation can be rewritten as $\frac{E_1}{E_0} = e^{(-t/\delta)}$

The **skin depth** δ is defined as the depth of penetration required by the EM field to be attenuated to *1/e* (37 %) of its value in free air. Alternatively, it can be defined as the depth of shielding material in which (*1 – (1/e)*) or 63.2 % of the charge flows [116]. It can be written as:

$$\delta = \frac{\sqrt{2}}{\sqrt{(\omega * \mu * \sigma)}} \quad \text{m} \qquad \text{where,}$$

μ = relative permeability in free space = $4 * \pi * 10^{-7}$ H/m

σ = relative conductivity of the material

ω = $2 * \pi * f$ angular frequency in radian/s

For the above equation, it is clear that the skin depth is independent of the shield thickness, but it is inversely proportional to the square root of the frequency. As the frequency increases, the skin depth becomes smaller.

The absorption loss through a shield is defined as [113],

$$A_{(dB)} = 20\log\frac{E_0}{E_1} = 20\log e^{(t/\delta)}$$

$$A_{(dB)} = 20\left(\frac{t}{\delta}\right)\log(e) \quad \text{dB}$$

$$A_{(dB)} = 8.69*\left(\frac{t}{\delta}\right) \quad \text{dB}$$

Hence, for t = δ, the absorption loss in the shield is 8.69 dB.
Substituting for δ, the absorption loss is given by

$$A_{(dB)} = 131.4*t*\sqrt{f*\mu_r*\sigma_r} \text{ dB,}$$

where
μ_r = relative permeability of the shield (= 1 for copper)
σ_r = relative conductivity of the shield (= 1 for copper)
t = thickness of the shield in meters

Therefore, absorption loss increases (better shielding) with the increase in frequency as square root of *f* on a decibel scale. It also increases with the thickness of the shield relative to the skin depth. On the other hand, at low frequencies the skin depth increases and the absorption loss becomes low.

4.1.3. Absorption loss Vs. Reflection loss

From the above theory, it can be summarized that the reflection loss is dependent on the wave and shield impedances. A mismatch in the impedances helps in partial reflection of the EM wave incident on the shield. If the impedances of the shield and the wave are closely matched, the EM wave passes through the shield barrier without any reflection. Shield materials having high

conductivity are good attenuators of an electrically dominant wave in near field conditions. This is because the wave is reflected back due to the impedance mismatch leading to successful reflection of the incident wave. Hence, reflection is the primary shielding mechanism for electric field dominant sources. Metallic shields having high conductivity, conductive paints, foils etc. provide high reflection properties, where the reflections occur at the front surface of the shield. For the same reason, multilayer shields are preferred to exploit the gain due to the reflections and increased impedance mismatch [117].

On the other hand, absorption becomes significant for the magnetic field dominant sources due to the amount of the incident wave absorbed in the shield. Therefore, thickness plays an important role for absorption, but has no consequence on the amount of wave that is reflected.

4.2. Imperfections in the shield

The evaluation of the SE in the previous section was done based on simple structures and in ideal conditions, assuming the shield is a perfect conductor with no discontinuities. Analyzing the SE of the shield in realistic conditions requires great computational effort and complex numerical simulations, depending on the type and geometry of the shield and the nature of the radiating source. In general practice, the performance of the SE is compromised, mainly because of discontinuities or penetrations within the shield. These discontinuities include apertures, gaps, slots, seams, cracks and junctions in the shield. Some of the discontinuities are inevitable to accommodate input/output cable penetrations, ventilating holes, power lines etc.

For a shield to be effective, the shield enclosure must be RF tight. At high frequencies, the design and construction of the shield becomes very important to accommodate the discontinuities and yet not compromise on the overall efficacy of the shield. This is because when the EM waves are incident on the shield, they induce currents on the surface of the shield. The induced currents should be allowed to flow on the shield and must travel on a continuous plane in order to produce reflective fields with a polarity such that it tends to cancel the incident fields that are a source of interference. Some of the discontinuities and imperfections in the shield can impede the current flow and tend to minimize the SE.

4.2.1 Apertures

At high frequencies, any metal conductor can provide a large magnitude of attenuation. However, the discontinuities spoil the shielding effectiveness as shown in figure 4.2. Regardless of the thickness of the shielding material, the presence of apertures in the shield reduces the SE. The amount of leakage mainly depends on three factors. They are:

1. Maximum linear dimension (not area) of the opening.
2. Wave impedance.
3. Frequency of the source.

In many of the shielded enclosures, it is critical to understand how the linear dimension and orientation of the discontinuities have an impact on the overall SE. If a hole or a slot in the shield is perpendicular to the induced currents, it may interrupt the current flow. If the slot is oriented parallel to the current flow, then the slot will have much less effect on the SE. In general practice, many multiple slots or holes are preferred compared to one large hole. This is because it is not always practical to determine the flow of induced currents, if the geometry of the shield and incident EM fields are not well defined.

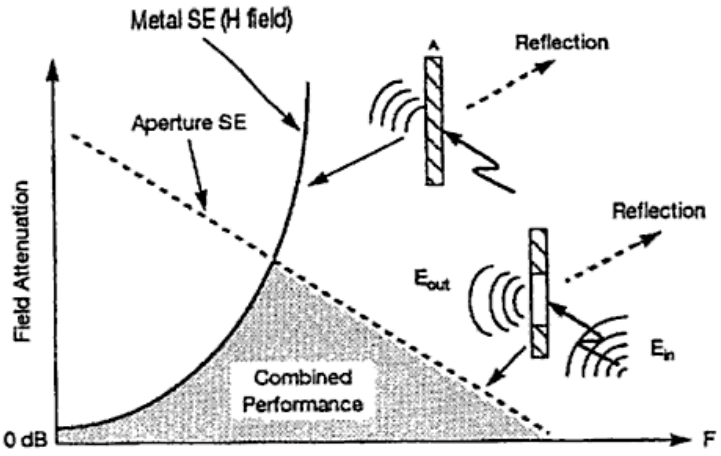

Fig. 4.2. Shielding effectiveness with and without aperture in the shield. Source: [118].

Another important factor affecting the SE is the behavior of the apertures as effective EM radiators such as intentional antennas whose dimensions are those of the apertures [119]. In other words, at high frequencies the intrinsic SE of the shield material is of less significance compared to the leakage through the apertures or holes. There will be a considerable amount of EM field

leakage if the linear dimensions of the apertures or slots are greater than 1/20 wavelength [110]. The slots in the shield act as effective radiators (slot antennas) at ½ wavelength. Therefore, the SE of the shield is reduced drastically if the linear dimension of the aperture is equal to or less than ½ wavelength. A simplified formula for calculating the attenuation for rectangular slot in a shield is given by [118]

$$SE_{dB} = 100 - 20\log l_{mm} - 20\log f_{MHz} + 20\log\left(1 + 2.3\log\frac{l_{mm}}{h_{mm}}\right) + 30\frac{t_{mm}}{l_{mm}} \text{ where}$$

l_{mm} = linear dimension of the slot in mm

f_{MHz} = frequency in MHz

h = slot height in mm

t = thickness of the slot (= thickness of the shield) in mm

the above equation is valid for $l < \lambda/2$. From the above equation, the linear dimension of the slot can be calculated in order to achieve a shielding effectiveness of over 100 dB. For **multiple slots**, SE is given by

$$SE = 20\log\left(\frac{\lambda}{2l_m}\right) - 10\log n$$

Here l_m = slot length in meters; λ = wavelength in meters; $l_m >$ slot height h; $l_m >>$ shield thickness t; n = number of slots.

The attenuation for **multiple round holes** is

$$SE = 20\log\left(\frac{\lambda}{2d}\right) - 10\log n$$

Here d = hole diameter in mm. The attenuation will become zero dB at $\lambda/2d = 1$. By creating a waveguide analogous to a honeycomb structure of multiple holes, the SE can be increased [120].

The above equation can be rewritten as [121]

$$SE = 20\log\left(\frac{150}{f_{MHz} * l_{meters} * \sqrt{n}}\right)$$

For practical measurements, it is significant to understand the type of EM source that must be isolated from the sensitive electronic components. Once the source is identified, the minimum

slot length or hole diameter can be computed to achieve the required attenuation at a given operating frequency.

4.2.2. Slot Antenna and its complimentary dipole

A slot in the conductive shield whose linear dimension is equal to ½ the wavelength is defined as a slot antenna (figure 4.3). At high frequency fields, the electromagnetic energy is radiated through the slot due to the induced currents on the shield [122]. The complement of the slot antenna can be considered as a dipole, where the regions of the shield and air as well as the electric and magnetic fields are interchanged. This implies the electric field will be horizontally polarized for a slot and it is vertically polarized for a dipole. The literature describing radiating emissions suggests minimizing the linear dimension of the slots that are less than λ/50 and never above than λ/20 [117, 123] to avoid RF leakage in the shield. At 100 MHz, it is suggested that apertures should not exceed 10 mm [117].

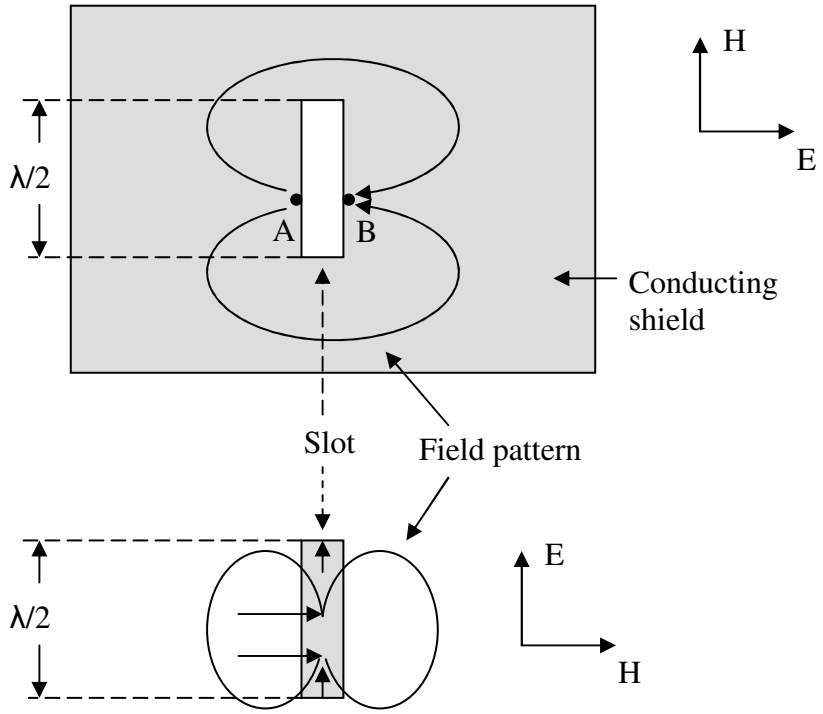

Fig. 4.3. Slot antenna and its complementary dipole antenna. Redrawn from [122].

There are many EMI containment strategies suggested in the literature [124, 125] to improve the SE of the overall shield enclosures. The use of conductive gaskets, screens, mesh and waveguides are some of the techniques used to improve the SE. Multiple apertures with small

diameter holes or honeycomb vents are employed for air cooling in an enclosure. EM shielding with metals provides good SE. However, not all electronic devices use metallic enclosures. Carbon fibers can be used with the plastic enclosures, but might not always be as effective as the shielded metal enclosures.

4.3 Grounding

A ground by definition points to an equipotential surface with zero impedance. In the real world, there is always a certain amount of impedance in the conductors. Hence, for practical purposes, a low impedance path must be identified for the current to return to its source [126]. This information is vital to identify the radiated emission from an electronic circuit and the susceptibility of the circuit to EM energy. The emphasis is more on discovering the path taken by the ground current. This is because the actual return path of the ground is not always as intended while designing a circuit. Determining the path of the ground current also helps in minimizing the magnetic coupling in the circuit. The magnetic (or inductive) coupling is a result of current loop area formed in the receptor circuit. For multiple ground paths, the loop area will be the path where the *actual* current flows. Therefore, by realizing that this path defines the ground, the large loop areas in the circuit can be minimized and the magnetic coupling can be reduced. It also helps in determining where to connect the decoupling filters to drain the high frequency interference components to ground in direct current (DC) circuits. The impedance of any ground conductor is given by

$$Z_g = R_g + j\omega L_g$$

where R_g is the resistance; ω is the angular frequency; j is the reactance component and L_g is the inductance in the conductor.

The impedance of a conductor is dependent on the frequency of operation. The resistance component of the impedance is more dominant at low frequencies, while the inductance component is more dominant at high frequencies. This is because the ground current takes the path of least resistance at low frequency conditions. On the other hand, the ground current takes the path of least inductance at high frequency conditions because the path represents the smallest loop area [110]. It is evident how the operational characteristics of the conductor vary depending

on the frequency conditions. In order to allow the current flow through the low inductance path, the ground current should not be interrupted.

4.3.1. Different Grounding Methodologies

There are different types of grounding that are employed depending on the type of electronic circuit (analog or digital) and the frequency of operation.

(a) Single-point grounding: This type of grounding is employed at low frequencies, where there exists a common current return path from multiple analog circuits. They can be connected in a series or parallel combination. Single-point grounding is easy to implement for simple circuits, but is considered inappropriate for complex digital systems that may lead to ground current imbalance and conducted emissions at low frequencies.

(b) Multipoint grounding: The implementation of multipoint grounding is suitable for high frequency systems, where each of the individual ground conductors of the circuit is connected to the ground plane or the chassis ground. This arrangement helps to minimize the ground impedance between the circuit ground and the chassis ground, leading to isolation of RF currents. The low impedance path is established mainly because of the lower inductance characteristic of the chassis metal enclosures connected to the circuit ground or ground wire of the electronic system.

(c) Hybrid grounding: If the electronic circuits are operated over a wide range of frequencies (few Hz to MHz), then hybrid grounding is employed that acts as a single-point ground at low frequencies and a multipoint ground at high frequencies.

At high frequency operation, all the single-point grounds act as multipoint grounds because of the stray capacitance between the ground conductor and the chassis (figure 4.4). The stray capacitance completes the loop because the impedance of the stray capacitance between the ground conductor and chassis is low. The ground currents flows through this low impedance path of the stray capacitance and avoid the long ground conductors that have high inductance.

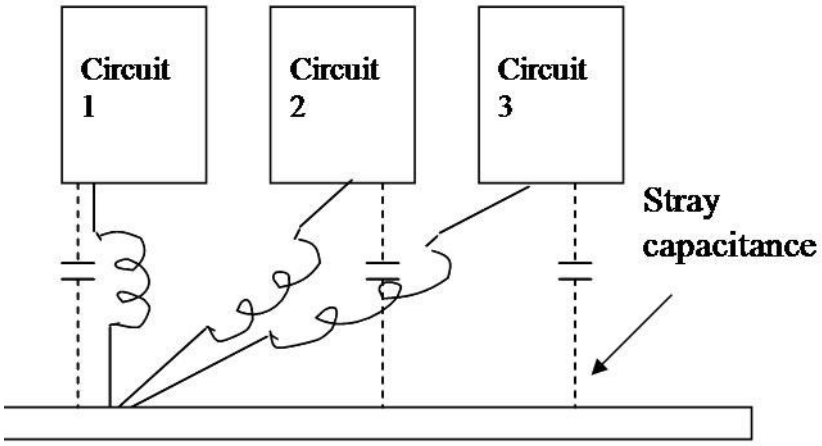

Fig. 4.4. At high frequencies, stray capacitances complete the loop. Single-point becomes multi-point ground.

In high frequency digital circuits, the ground leads of the digital components connecting to the chassis ground must be kept as short as possible to minimize the lead inductance. A large inductance due to the length of the ground leads increases the overall ground impedance. This leads to development of voltage potential across the connecting ground wire/lead resulting in common-mode coupling in the circuits. In addition, physically long ground wires act as small antennas that contribute to radiated emissions at high frequencies. Therefore, keeping the length of the ground wire short helps to minimize the magnetic coupling. The main goal is to couple the RF currents to the chassis ground by implementing a low-inductance distribution network.

4.3.2 Ground Loops

Ground loops occur when there is a potential difference between the ground currents and there are multiple ground currents flowing through the ground impedance path. These contribute to the propagation of RF energy because the ground current will attempt to flow in any available path. In high frequency circuits, inductance causes magnetic coupling of the RF currents with the digital circuits that results in an increase in the RF losses in the return path. A loop antenna is created that allows the RF energy to propagate on the DC lines and interfere with the overall signal integrity of the system. Therefore, the RF generating circuit must be kept as close as possible to the ground plane. There are three main solutions that are suggested in the literature [110, 127, 128] to break the ground loops, namely the use of isolation transformers, common-

mode chokes and optical couplers. These techniques help isolate the noise voltage on the transmission line from the signal.

4.3.3 Filters

Apart from connecting the ground wire or plane to the chassis ground to minimize the ground impedance, it is necessary to allow the high frequency RF currents present between the signal and ground planes to drain to chassis ground. This is implemented by employing decoupling capacitors that shunt high frequencies to ground. Depending on the lead inductance and the frequency of operation, decoupling capacitors are selected to minimize the RF voltages and currents between the signal and ground planes. This method would enhance the RF isolation in the system [127].

4.3.4. Antennas and Wavelengths: What constitutes an Antenna?

As the frequency of operation increases, the wavelength decreases as shown below:

$$f(Hz) = \frac{3*10^8 m/\sec}{\lambda}$$

$$f(MHz) = \frac{300}{\lambda(m)}$$

$$\lambda(m) = \frac{300}{f(MHz)}$$

where λ is the wavelength and f is the frequency. The frequency at which the components near the clock signals and switching circuits resonate at RF energies due to longer wavelength ground planes, becomes the *critical frequency.* The *electrical length* is defined as the ratio of the physical length (L) of the component to the wavelength (λ) at the fundamental frequency.

$$\text{Electrical Length} = \frac{L}{\lambda}$$

For very high frequency applications and in the design of printed circuit boards, an electrical length that is less than 1/20 wavelength is considered electrically short. However, there is a possibility that if the cables or wires have large impedance mismatches at RF frequencies then the electrical length of even 1/50 may not be considered as electrically short [129]. Large size electronic components such as resistors and capacitors cannot be used at very high frequencies because of their linear dimensions. Therefore, smaller components are preferred. Table 4.2 below shows the wavelengths at different frequency values.

Table 4.2. Wavelengths at various high frequencies

Frequency (MHz)	**Wavelength λ (m)**	**λ/4 (m)**	**λ/20 (m)**	**λ/50 (m)**
10	30	7.5	1.5	0.6
50	6	1.5	0.3	0.12
100	3	0.75	0.15	0.06
200	1.5	0.375	0.075	0.03
300	1	0.25	0.05	0.02
400	0.75	0.1875	0.0375	0.015
500	0.6	0.15	0.03	0.012

Apart from the parasitic capacitances and inductances that may be prevalent at high frequencies, if the cable length is electrically long at high frequencies then it can pick up the EM waves and can cause destructive interference in the circuits. The EM waves can bounce back and forth on the electrically long wires, which can radiate energy readily. The operational characteristics of some components vary and do not behave as intended at RF frequencies. The long cables can turn into antennas. If the signal wavelengths are smaller than the wire lengths, the RF effects dominate and further amplify the antenna operation. This is because the radiated power is proportional to the frequency and antenna length [130]. The electrons in the cables do not experience a net movement but they slosh back and forth and propagate the RF energy through the wires. In DC sources, there is a constant drift of the charges that produce reactive fields, while in the alternating current (AC) sources there is an acceleration of the charges that produce both reactive and radiating fields. The reactive fields store energy in the absence of

another circuit. If there are other circuits in the vicinity, the reactive fields can transfer energy either by capacitive or inductive coupling. Therefore, the electrons in the electrically long cables pass the RF energy from the RF source to the load or the DC circuitry, causing interference. At RF frequencies, the circuits that are electrically long require careful design to avoid generation of unintentional antennas. Hence, to confine the RF energy within the circuits, the long length of the ground conductor must be kept shorter than 1/20 wavelength or utilize multipoint ground planes wherever the length exceeds 1/20 wavelength.

4.4. Chapter Summary

An overview of shielding and grounding approaches, mainly at high frequencies was discussed in this chapter. The basic understanding of the shield performance with imperfections in the shield is significant in order to justify the implementation of shielding for PET/MRI operation. Shielding effectiveness can be calculated theoretically for holes and slots at a given shield geometry and frequency of operation. In addition, the ground topology and ground current flow mechanisms at RF frequencies give insight to identify the path of lowest impedance in the circuits. And finally, it is vital to identify the circuit components that act as unintentional antennas at the operating frequencies. All the above theory and explanation can help clarify the different mechanisms of RF interference on the DC sources.

CHAPTER 5: EVALUATION OF EMI BETWEEN PET AND MRI SYSTEMS USING SHIELDING AND GROUNDING METHODS

An overview of the shielding and grounding approaches discussed in the previous chapter is necessary to evaluate the performance of PET and MRI systems. Electromagnetic shielding is important to protect the electronic components from the RF fields. The following sections discuss the required changes in the ground topology and the effect of shielding on the performance of the PET and MRI systems.

5.1 Evaluation of cable layout and grounding topology for PET setup on the bench

The following sub-sections discuss the grounding schemes while setting up the PET detector for the scans on the bench and are independent of the effect of MRI pulse.

5.1.1. The initial cable and grounding layout for the PET system

The PET detector mainly requires a low voltage DC power supply to power the PET system clock and two high voltage supplies to power the APDs. The complete PET detector setup with the PET detector and its power supplies can be imagined as one unit arranged on the bench. However, the PET detector was stationed away from the power supplies to perform awake animal studies [95]. The requirement is the same even for the PET/MRI setup where long distance cables are required between the PET detector and the power supplies. Therefore, the PET detector was powered using 10-meter long cables. Figure 5.1 shows the schematic of the initial cable connection setup of the PET detector. A shielded coaxial cable with three pigtail connector plugs (+6V, GRD, SHIELD) is connected from a low voltage DC (6V) supply to the TSPM box that powers up the TSPM board having voltage regulators, gigabit link chipsets among other circuit components. The TSPM board delivers 1.9 V to power up the flexible printed circuit board (PCB) of the PET detector. To power up the APDs on the PCB, two high voltage DC power supplies (HV1 and HV2) were used, which are connected to the TSPM box through BNC (RG58) coaxial cables. The current return path from the +6V supply flows to its source through the shielded pigtail cable. From the figure, it is evident that the return current

paths of the two high voltage supplies also find their way back to the supplies through the same conductor.

Ground loops: The schematic of the PET detector cable connections are shown in figure 5.2. The PET grounding topology is an example of single-point ground, where the signal return grounds are tied together. It can be visualized as the series connection of all the circuit grounds and is generally employed using simple unshielded wires connected to banana plugs. If the return paths of the currents in these cables are visualized to be current carrying conductors, it induces magnetic coupling between the circuits. The low voltage shielded cable carries currents in both directions inducing magnetic fields that oppose each other. If the currents are equal and opposite, the magnetic fields cancel out. However, there might be some residual field left due to slight current imbalance caused by the HV return currents.

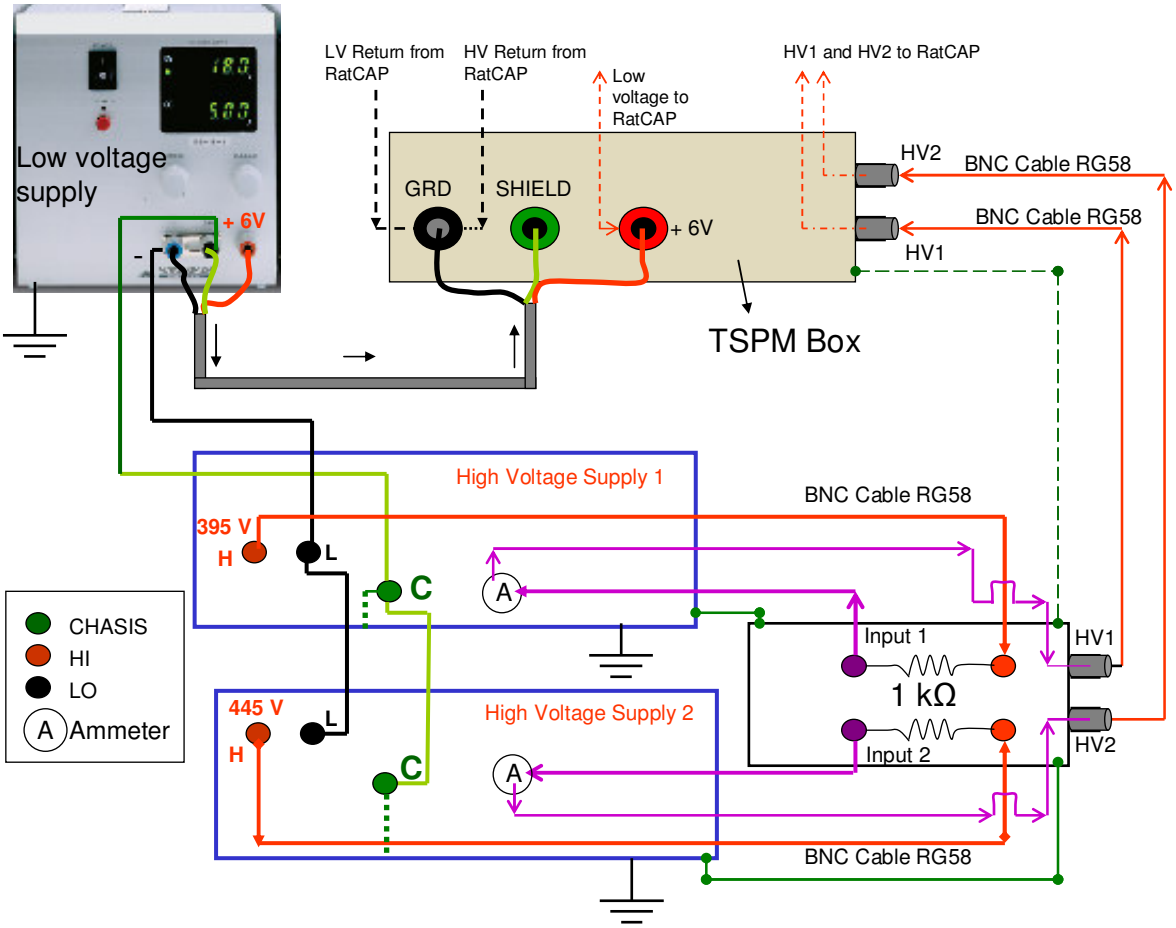

Fig. 5.1. The PET cable connections.

The high voltage coaxial cables do not have their own current return paths. Therefore, the return paths for the high voltage cables are tied to the return path of the low voltage supply. Sharing the same return path may lead to inductive coupling. In this configuration, there are two current carrying conductors in the same direction, which may contribute to common-mode currents and induce significant magnetic fields around the cables. Also, this coupling is dependent on the loop area enclosed by the actual current flow. As the loop area in the existing configuration is significant, the imbalance in the ground currents may introduce noise in the system. Moreover, this configuration is not considered ideal for operation at high frequencies [131].

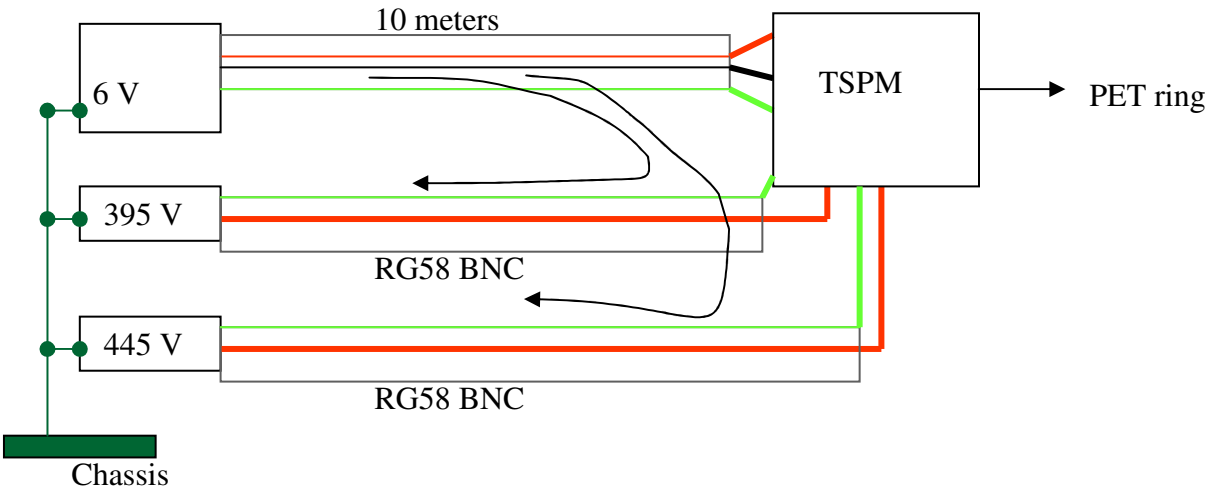

Fig. 5.2. Schematic of PET cable connections using BNC cables causing large ground loops indicated by the dashed arrows.

The shielded pigtail cable connectors that carry low voltage and connect to the TSPM box may have significant effect on total noise coupling to the cable. The current return path must be as close as possible to the signal conductor to cancel the magnetic flux between them. Also, the exposed section of the pigtail allows direct coupling of interior shielded cable over the length of the pigtail section. Hence these pigtails may easily pickup the noise currents at high frequencies [132], if their lengths are electrically too long. Some of the noise pickup can be minimized if the PET detector were setup in the Varian/Siemens 4 T human MRI scanner, because the MRI room is a Faraday shield. The cables entering the MRI room can be fed through the filter panel to suppress some of the noise coupling entering into the room. However, the same setup cannot be used in Bruker 9.4 T MRI scanner as the MRI room is not a Faraday shield. Therefore, there was

a requirement to replace the cabling and the termination strategies for better performance of the PET detector either on the bench or in the high magnetic fields.

5.1.2. The final cable and grounding layout of the PET setup

A large area of ground loops must be avoided to prevent conducted emissions from the cables [133]. At high frequencies, the magnetic coupling in the cables must be suppressed by using optimum shield terminations. A mere ground plane connection is inadequate because the shield must be terminated uniformly for maximum protection. A 360^0 contact between the shield and the connector is recommended to suppress the noise coupling at high frequencies [132]. Also, experimental data has been published that demonstrates how the noise coupling is predominantly due to the pigtail connections [134]. To ensure a better grounding framework, any ground current imbalances must be minimized. Since the ground loops in the PET detector cable layout are identified, the low voltage power cable with three pigtail plugs (for 6V, signal return and shield) as well as the BNC cables connected to the high voltage supplies were replaced with a multi-conductor shielded cable. The main advantage of using a multi-conductor cable is the conductors that were carrying the low and high voltage signals are in close proximity to the center ground conductor (or the signal returns), minimizing the magnetic flux between the conductors. In addition, the shielded cable completely encloses the signal and ground conductors. A well bonded connection between the chassis and the shield is desired. Two MLTR (MS3106A14S) connectors were used at either ends of the cable. The connector at one end of the cable is terminated to the TSPM aluminum box, which is essentially the shield enclosure. The second connector on the other end of the shielded cable is terminated to the chassis ground of the power supplies. This arrangement of having a direct connection of the connector shell to the equipment enclosure provides a 360^0 contact between the shield and the connector providing a uniform ground connection around the connector shell.

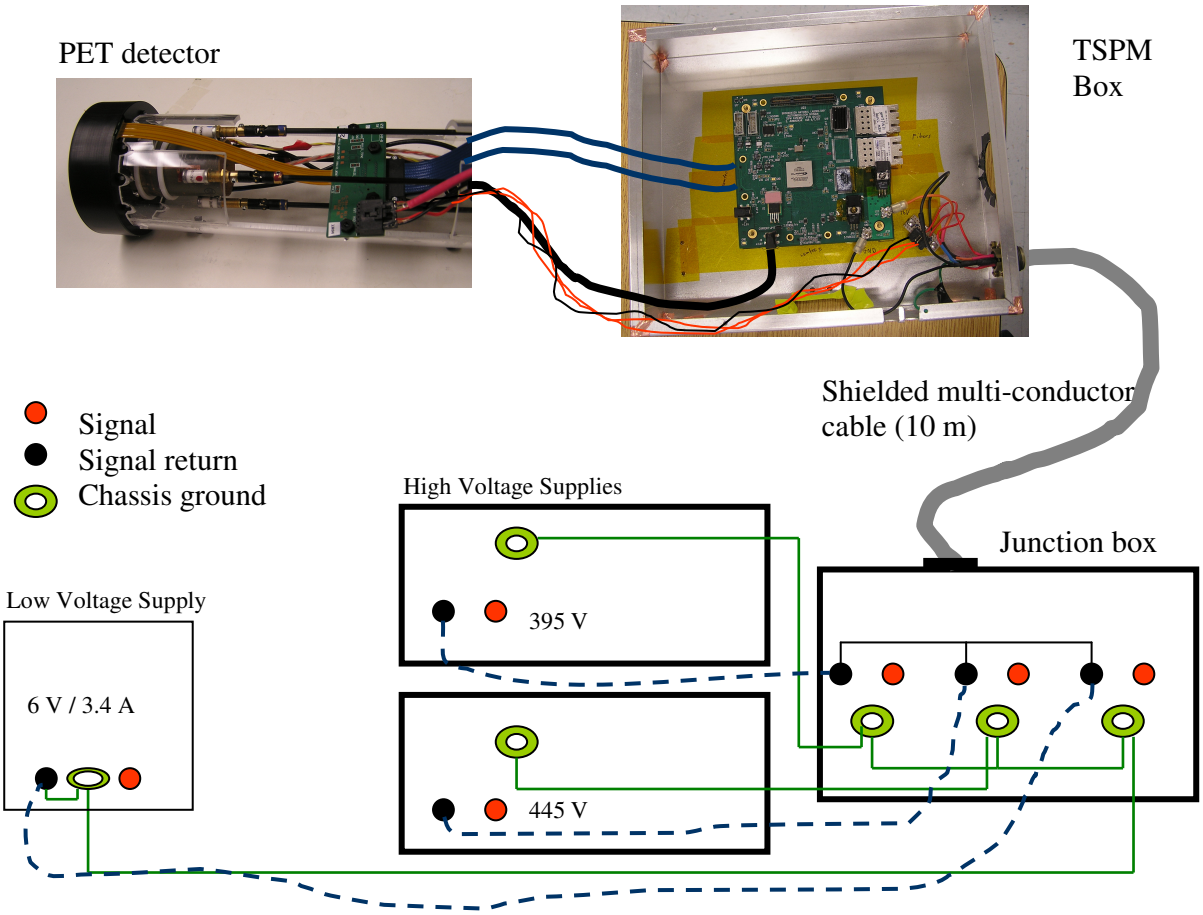

Fig. 5.3. Schematic of PET detector setup using multi-conductor cable. The cables from the TSPM box to the PET detector were housed in a shielded tube assembly.

Figure 5.3 shows the cable layout with the shielded multi-conductor cable. After powering the PET detector and acquiring the background baseline PET counts on the test bench, it was observed that there were some low-magnitude noise spikes in the PET data. These spikes were occurring at every 9 ms time period (~ 110 Hz). This behavior was also observed when the PET detector was powered inside the MRI, without RF pulsing (Chapter 3, section 3.2.2., Figure 3.6). Hence, the spikes are independent of RF pulsing. The following observations were made:

- The signal returns are kept separate from the shield ground in this setup. This was intentional because the shield ground was considered to be the low-impedance path to ground.
- An exception to the above statement is that the signal return ground at the low voltage power supply is connected to the chassis of the supply. This is the only place where the signal return and the shield grounds are tied together.

- There was a potential difference of 120 mV between the signal return and the shield grounds, when the PET detector was powered.

From the above observations, it is clear that there is an imbalance in the ground currents leading to noise. These noise currents are making their way into the front-end electronics of the PET detector. The single connection between the signal return and the shield ground is an example of a cable shield grounded at one end. Having the signal and ground conductors confined in a shielded cable is a good grounding practice. However, this arrangement was not effective. This is because the cable is grounded at one end. As a result, the stray capacitance originating at the ungrounded end of the cable shield completed the ground loop. Although the signal return and the shield grounds are connected at one end, the difference in the ground voltages indicate that the ground impedance was very high. In other words, there is an increase in ground impedance due to the large inductance in the cable shield. Therefore, even though the grounds are tied together, it appears as an open circuit. Since one end of the cable shield is left ungrounded, it does not provide good isolation to the ground. Instead, the stray capacitance in the vicinity of the setup completes the ground loop and introduces noise currents flowing in the signal conductors. This behavior is mainly observed at high frequencies where the physical cable length is longer than the wavelength of the fundamental frequency, resulting in reactive emissions on the cable. Grounding both ends of the cable shield is recommended in the literature [135], since this enhances the magnetic shielding. Grounding both ends of the cable shield allows the high frequency currents to flow on the surface of the shield. These in turn create magnetic fields that cancel the fields emanating on the signal conductors. Therefore, grounding the shield at multiple locations augments the circulation of high frequency currents that counteract opposing fields and improve magnetic field shielding.

The cable shield was grounded at multiple ground points to break the loop and *divert* the ground currents towards the path of least inductance and thus, maintain low ground impedance. By doing so, the voltage potential between the signal returns and the shield grounds was minimized from 120 mV to 0 mV. Figure 5.4 shows the cable shield is bonded at multiple points, which reduces the potential between the signal return and the shield. Also, the signal returns are tied to shield enclosure at multiple points on the TSPM board to enhance the noise suppression. After these changes were made, there was no interference of noise in the PET data.

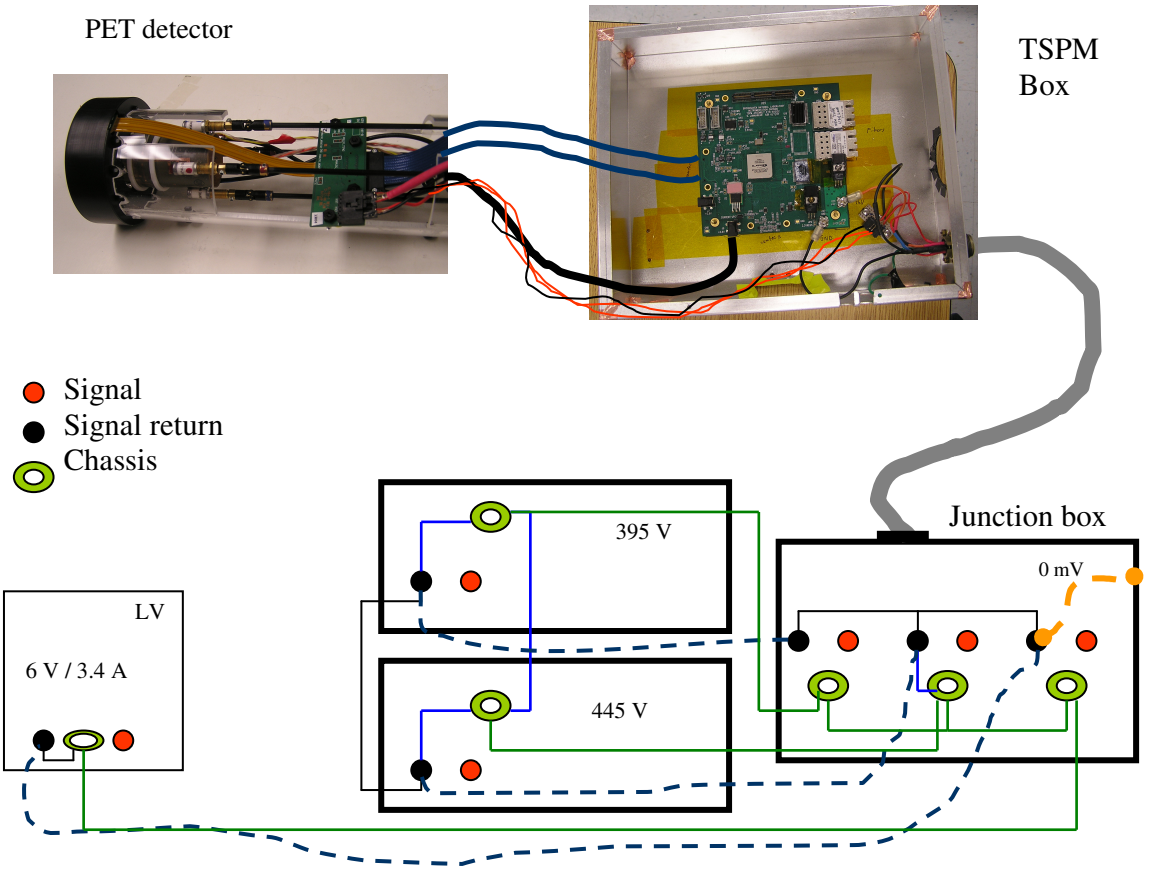

Fig. 5.4. Schematic of PET detector setup with signal returns connected to the shield (chassis) ground at multiple points (shown in blue).

5.2 Identifying the interference pattern in PET

As discussed in the previous chapters, the PET data is corrupted with spurious counts during MRI acquisition. It is important to identify the path of interference on the PET electronics. The goal is to investigate if the interference observed in the PET data is due to the radiated emissions emanating from the RF coil or due to the conducted emissions from the signal and power cables. The RF coil is a tuned R-L-C circuit as shown in Figure 5.5.

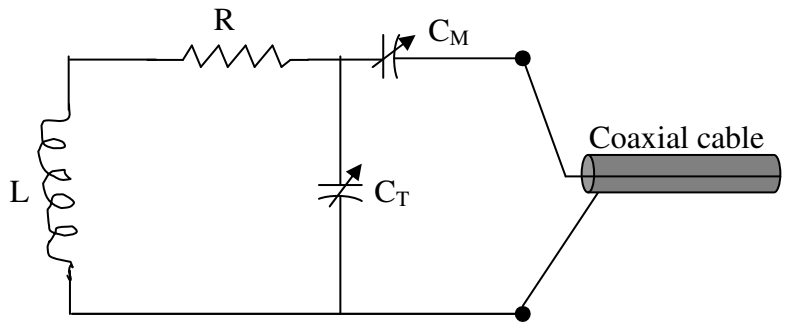

Fig. 5.5. A typical RF coil circuit.

A sharp frequency response can be achieved by tuning the circuit at resonance. The alternating current will reach its maximum when the circuit is driven at its resonant frequency. The signal conductors of the coaxial cables are connected in series with the matching capacitors of the RF coil. These RG58 cables have a characteristic impedance of 50 Ω. Hence, for efficient power transfer, the RF coil impedance is also matched to 50 Ω in order to match the 50 Ω output of the power amplifier. When the coil is tuned to its optimum, the coil impedance becomes a pure resistance.

For the experiment, the RF coil is tuned at 400.32 MHz frequency on the test bench. At this point, the coil impedance is a pure resistance of 50 Ω. To investigate if the interference affecting the PET electronics was due to the conducted emissions, the coil must be isolated from driving the RF currents to rule out the contribution from the coil. In order to achieve that condition, the signal conductor of the coaxial cable is disconnected at the matching capacitance and a 47 Ω resistor was connected in series to ground, as shown in Figure 5.6.

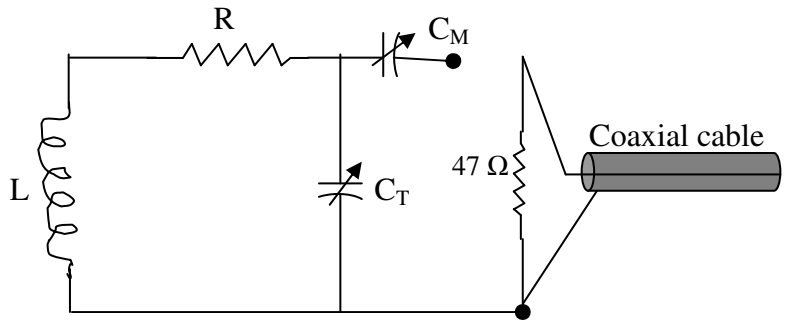

Fig. 5.6. The RF coil is disconnected from the circuit and connected to a 47 Ω resistor in series.

Since there are two pairs of coils, the replacement was done on both coil pairs. The coil is then secured into the PET detector and assembled in the tube as described in Chapter 2. The PET

is setup inside the 9.4 T magnet bore. When the RF is pulsed in this condition, the currents from the coaxial cable pass through the resistor to ground. This implies that the coil is left isolated, resulting in no radiated emissions. The only noise contribution can be from the conducted emissions from the cables interfering with the PET acquisition. A low duty factor MR sequence was pulsed for this study, as the resistors were not rated for the typical RF powers used in the MRI. During RF pulsing, the PET data was monitored to check if there is a corresponding increase in the singles count rate.

There was no indication of interference from the cables as there was no change in the PET count rate due to the RF pulsing. From this experiment, it is concluded that the path of interference is not due to the cables, but due to the RF coil acting like a radiating antenna. The resistors were disconnected and the signal conductor of the coaxial cable is connected back to the matching capacitor for both coil pairs.

5.3 Shielding the PET detector electronics

It has been identified that the electromagnetic (EM) fields generated by the RF coil propagates into the unshielded PET electronics and create interfering signals. Therefore, electromagnetic shielding is necessary around the PET detector housing to minimize the impact of EM fields on the PET electronics. At high frequencies the RF impinging on a shielding material creates local currents on its surface due to the skin effect. With the increase in the frequency, the effective resistance of the shield material increases resulting in currents flowing on the 'skin' of the shield material. These compensating currents generate local magnetic fields opposed to the original RF fields. However, if the fields are equal and opposite, then there is no or minimal effect of RF on the shielded devices. Accordingly, shielding the PET electronics and creating a good Faraday cage would help suppress the effect of RF on PET in the PET/MRI setup.

Skin depth, as described in Chapter 4 is given by $\delta = \frac{\sqrt{2}}{\sqrt{(\omega * \mu * \sigma)}}$ (meters) where

μ = magnetic permeability in free space = $4 * \pi * 10^{-7}$ H/m

σ = conductivity of the material (=1 for copper)

$\omega = 2 * \pi * f$ angular frequency in radian/s

Arranging the units, the skin depth for copper in meters is given by:

$$\delta = \frac{1}{\sqrt{\pi \mu \sigma f}}$$

From the above equation, it is evident that the skin depth is inversely proportional to the square root of conductivity, indicating that metals that are good conductors have lesser skin depth. Compared to other metals (e.g. iron or steel), copper is a better choice in terms of durability, machinability and is a good non-ferromagnetic material for shielding EM fields. Since the currents reside on the surface of the copper shield at high frequencies, hollow copper tubes are preferred over solid conductors.

There are two possible ways to shield the PET electronics from the EM fields generated by the RF coil:

- **Shield the RF coil**: Since it is the source of high- intensity RF fields, shielding it appreciably minimizes the effect of RF on the PET electronics. The coil is the main 'source' of RF that is radiating noise not only into the PET electronics, but also in the traces going to/from the circuit, and into everything the cables are connected to (e.g., signal processing module, power supplies, AC mains).
- **Shield the PET housing**: Shielding the PET housing ensures a Faraday-cage like structure wherein the RF fields from the coil cannot penetrate into the PET's electronics. Accordingly, the PET components and its circuits are isolated from potential interference from the RF pulses.

In principle, both of the above methods can be employed to obtain considerable RF tight shielding. However, the latter arrangement was implemented because having a shield around the RF coil resulted in changing the coil tuning range and spoiling the Q factor. Having a shield within 5 mm of the coil circumference, detunes the coil and tuning the coil would require changes to the coil components. Moreover, there could be a compromise on the Q factor of the coil with the shield. Another important factor is the inability to mechanically fit the coil inside the PET detector, given the geometry and the dimensions of the PET detector. The components

mounted on the outer surface of the RF coil are at least 5 mm in height, increasing the overall outer diameter of the coil to 37 mm. Therefore, there is < 1 mm gap between the outer diameter of the coil and inner diameter of the PET detector. Alternately, the shield that is used around the PET detectors can be considered as a shield to the RF coil as well, given the close proximity between the coil and the shielded PET housing.

5.3.1 Different configurations of the PET detector shield

The RF coil is excited with a 400 MHz carrier frequency in narrow band (bandwidth < 10 kHz per slice). Three different configurations of shielding were tested to evaluate their effects on the RF interference (Figure 5.7). The first shield (figure 2(a)) is a thin 18 µm copper sheet, glued with epoxy resin to all the surfaces of the unshielded plastic housing (ID = 38 mm). At 400 MHz, one skin depth of the copper equals 3.3 µm. Therefore, the copper sheet provides a shielding of more than 5 skin depths. It is specified in the literature [116] that a shield with a thickness of five times skin depth provides a 'perfect shield', as the currents are often considered negligible (i.e. $(1/e)^5$ ~= 0.007 = 0.674 %) on the active side of the shield. This would imply that the copper sheet virtually provides complete shielding. The copper layer is segmented to minimize the effect of eddy currents on the MR images originating from the gradient fields. Although all the outer surfaces of the plastic housing are encompassed by this single copper layer, the outer surface of the inner ring of this housing (the sleeve that forms the inner diameter of the PET) had two segmented offset copper layers attached to a thin kapton sheet.

The second shield again is a segmented copper but comprises two layers (double-sided), giving a total thickness of 36 µm; it was placed on all the inner and outer surfaces of the same plastic housing with good ground terminations. The copper segments were arranged to offset the axial gaps and holes intentionally to make the shield more RF-tight (if there is a possibility of the RF leaking into the shield through axial gaps). The third shield is a 1-mm thick aluminum housing (ID = 38 mm), which is continuous on all faces with no segments. For aluminum, one skin depth at 400 MHz equals 4 µm. Since the aluminum shield thickness is 1 mm, it might be an overkill providing a shield of over 200 skin depths. The MR images and PET data were acquired with these three shields in place, and compared with images from the unshielded system.

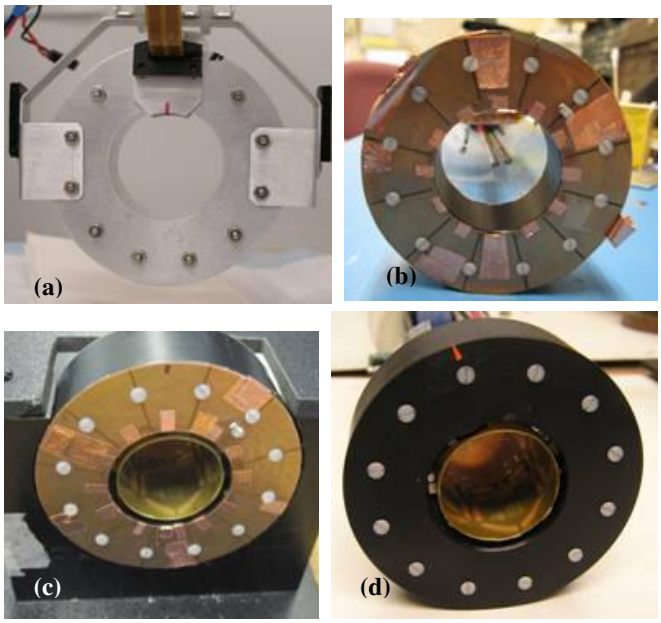

Fig. 5.7. Different shield housings. (a) aluminum, (b) single-layer copper-, and (c) double-layer-copper shields. The results were compared with unshielded housing (d).

5.3.2 The effect of different shields on the PET detector

To study the effects of shielding on PET data, the PET detectors were carefully removed and re-assembled in the different housings. The PET data was acquired outside and inside the MRI (with RF OFF) to analyze the effect of the shield alone on the PET count rate. The baseline count rates of the PET, i.e., the singles counts per second, were compared with and without the different shields. Figure 5.8 shows that there is no significant difference in the count rates under these different conditions.

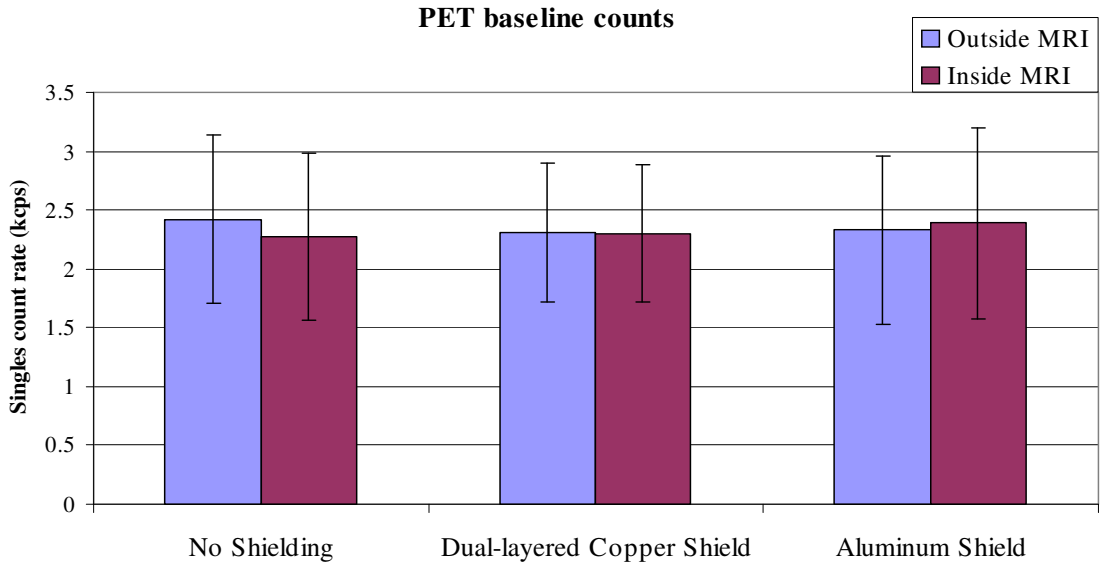

Fig.5.8. Comparison of PET baseline singles count-rate with different PET housings.

The effect of RF on PET was investigated, employing three different MR pulse sequences: (a) rapid acquisition with relaxation enhancement (RARE) spin echo with rare factor 8; (b) spin echo (SE); and, (c) fast low-angle shot (FLASH) gradient-echo sequence. With the RF turned ON, the singles count rate was highest for the unshielded condition and lowest for the aluminum shield (Figure 5.9).

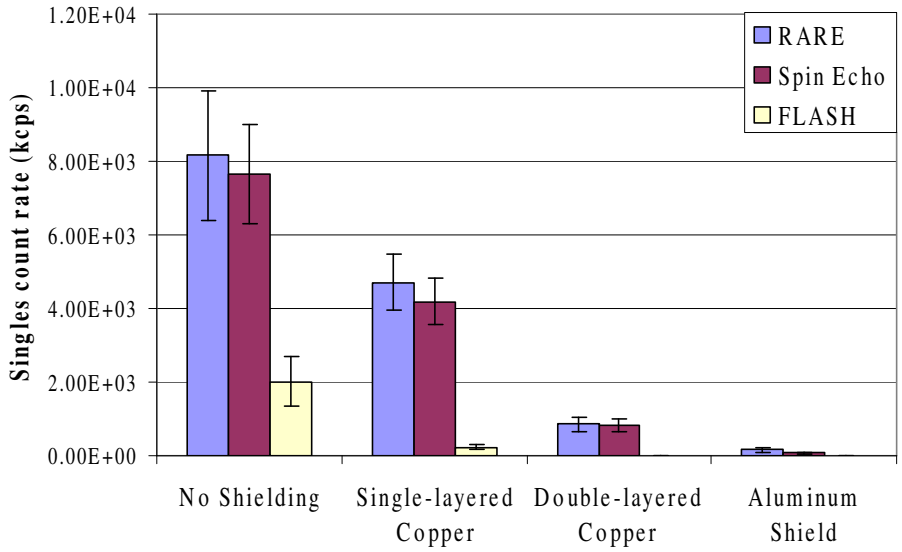

Fig. 5.9. Comparison of the PET count rates during RF pulsing for different shield conditions.

A minimal suppression of RF was noted using the single layer of segmented copper layer on the outer surfaces compared to the double-layer copper shield. The aluminum shield and the double-layer copper eliminated the effect of the FLASH gradient echo-sequences; furthermore, both suppressed the effect of the RARE sequences, compared to the unshielded condition. Moreover, in some PET channels, none of the counts were blocked.

5.3.3 The effect of different shields on MR images

The tuning range of the RF coil was adjusted due to the frequency shift created by the close proximity of the shield. The signal-to-noise ratio (SNR) in the MR images was compared with different shields. A cylindrical phantom (ID = 17 mm) filled with 2.5 g/L of a gelling agent (Gelzan) was used to acquire MR images. Figure 9 shows the effect of shielding on the SNR. It was calculated using the ImageJ MR processing tool by drawing a small region of interest (ROI) on the phantom and outside the phantom of the MR image, and computing, for each slice, the ratio of the mean pixel value in the phantom to that of the standard deviation outside the phantom. The SNRs for all the sequences with the aluminum shield in place were poor and the image quality was degraded compared to the unshielded condition (Figure 5.10).

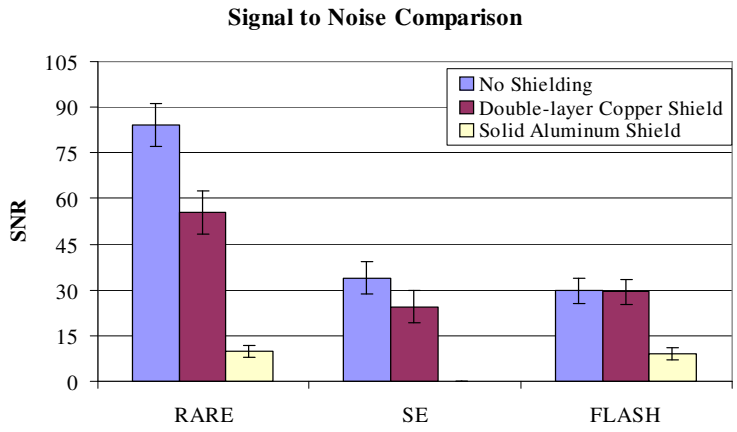

Fig. 5.10. Comparison of SNRs of MR images for different shield conditions.

The deterioration mainly is due to the effect of eddy currents resulting in poor reception of the MR signal. On the other hand, there were no visual artifacts or eddy current effects on the MR images acquired using the double-layer copper shield, as shown in Figure 5.11.

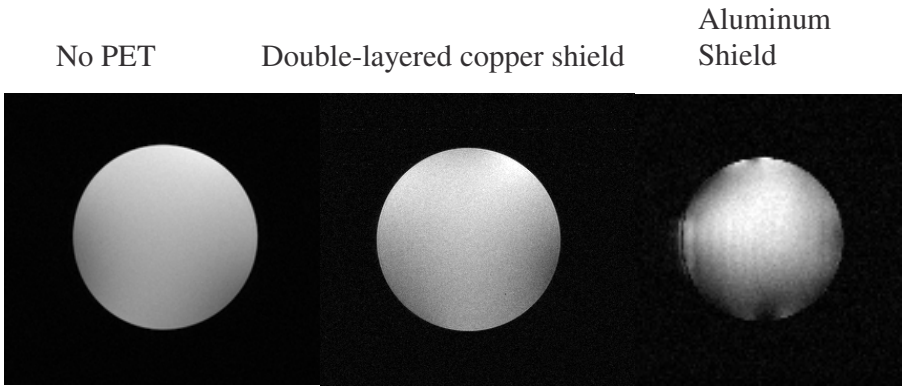

Fig. 5.11. Comparison of MR images for different shield conditions.

The drop in the SNR in comparison with the unshielded condition is expected due to the proximity of the metallic shield to the RF coil. However, the SNRs for unshielded and double-layer copper shield conditions for the FLASH sequences were not significantly different. This could be due to the non-uniformities at higher flip angles. If the refocusing pulses in the RARE sequences are not optimized at the set flip angle, it may degrade the MR images. In FLASH sequences, the flip angle is usually < 30^0 degrees and there is no refocusing involved. Hence the overall effect due to the refocusing pulse is absent for both unshielded and double-layer copper shield conditions. Figure 5.12 shows the homogeneity measurements performed with no PET and double-layer copper shield conditions. As observed from the plots, the uniformity of the images across all slices were below the recommended standards [136]. Here, the area of the ROI on the MR images was drawn close to 75 %. These recommendations were made for human MR scanners. A smaller cross-sectional area may improve the uniformity, though by a small amount.

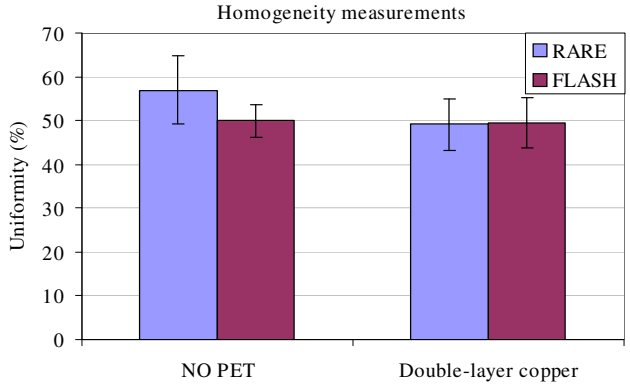

Fig. 5.12. Comparison of homogeneity

As evidenced from the plots, the double-layer segmented copper shield is a good tradeoff, giving good-quality MR images while significantly minimizing the effect of RF. In addition, the PET counts in some channels are not obliterated when the dual-layer copper shield is used. To verify whether powering the PET electronics would influence the quality of the MR images, they were acquired both with PET OFF and ON using the double-layer copper shield housing. A large ROI was drawn on the phantom image and the standard deviation was measured using ImageJ. By subtracting the MR images with PET powered and unpowered, the standard deviation of the subtracted image was recorded by drawing a large ROI. From the Figure 5.13, it is inferred that powering the PET electronics has no effect on the quality of the MR image quality.

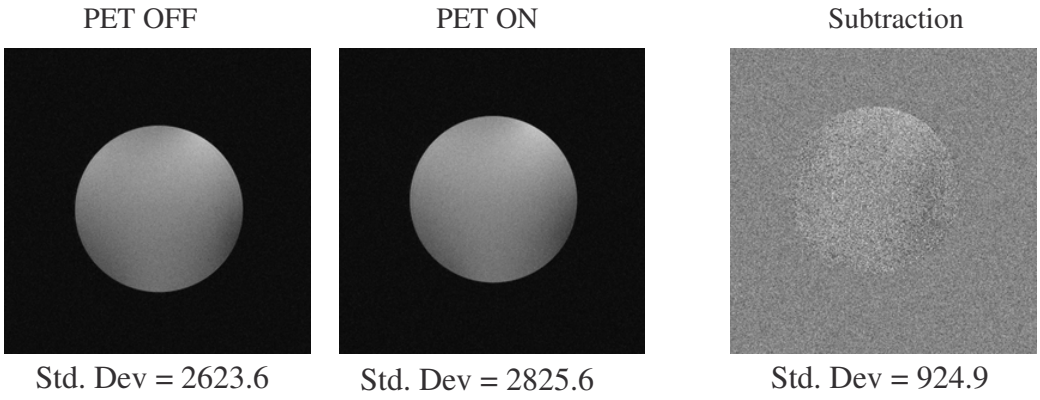

Fig. 5.13. Subtraction of MR images during PET OFF and PET ON conditions.

5.3.4 MR images of a fruit and a vegetable with copper shield PET

To further illustrate the ability of MRI to resolve fine structures with PET shielding, MR images of a slice of tangerine and an onion that fit inside the RF coil were acquired with the PET OFF and PET ON condition, using the double-layer copper shield. Figure 5.14 shows the MR images demonstrating that fine structures < 100 µm are resolvable.

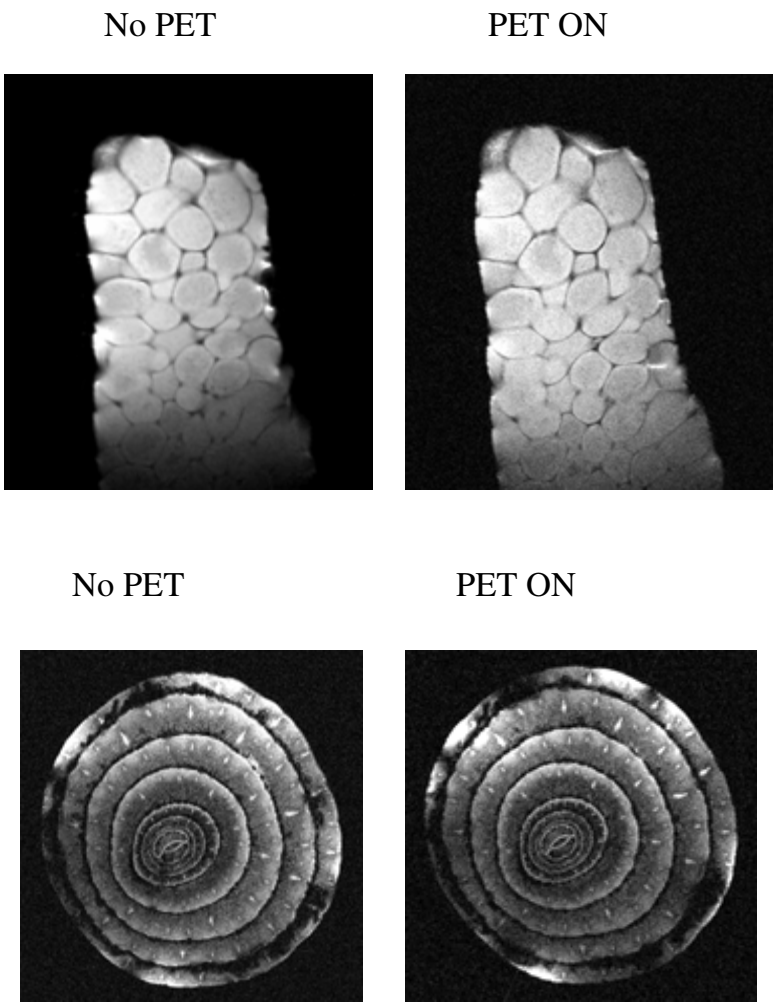

Fig. 5.14. MR (RARE) images of a tangerine slice (top) and FLASH images of an onion slice (bottom) with PET OFF- and ON conditions.

5.4 Evaluation of PET performance using double-layer copper shield

It is deemed that the double-layer copper shield was the best choice for shielding the PET detectors from among those that have been evaluated. The PET detector's performance was assessed by collecting PET data with MR ON and MR OFF conditions.

5.4.1. PET sensitivity

The coincidence sensitivity of the PET system was calculated using a ^{22}Na point source (30 μCi) in a Delrin backing and covered by acrylic cube. It has an active diameter of 1 mm and a length of 0.5 mm. The point source was centered inside the holder and was guided into the magnet so that the source is at the PET center of the field-of-view (axial and transaxial). Over

10,000 coincidence counts were acquired with MR OFF, FLASH and RARE conditions, respectively. The spurious counts in the PET data acquired during the RARE sequence were gated out for these measurements. A coincidence time window of 20 ns (± 10 ns) was used and the LLD was set to 350 keV. The true coincidence rate was calculated by subtracting the randoms from the prompts and divided by the total time of acquisition. The absolute sensitivity [103] of the system was calculated by taking the ratio of true coincidence rate (counts per second) to the product of the measured activity of the point source in Becquerel and the branching fraction of ^{22}Na (0.906). The absolute coincidence sensitivity for MR OFF, FLASH and RARE conditions was calculated to be 0.31 %, 0.30 % and 0.2 % respectively. The decrease in the sensitivity during RARE sequence was due to the dead time in the PET data during RF pulsing. The point source data was acquired on the workbench outside MRI scanner. The absolute sensitivity was 0.30 %. Therefore, except for the PET data during RARE sequence acquisition, the PET sensitivity measurements outside the MRI scanner vs. MR OFF vs. FLASH acquisitions show no significant degradation in system sensitivity.

5.4.2 Spatial resolution

The PET data that was acquired for the sensitivity measurements were processed to calculate the spatial resolution at the PET center of field-of-view. The point source sinograms from each of the MR conditions were added to the uniform cylinder phantom data sinograms that was acquired separately. The source to background contrast ratio was 5:1. The PET ML-EM images of the point source were reconstructed for each of the MR conditions. Spurious counts during the RARE sequence pulsing was discarded from the PET data before reconstructing the images. The spatial resolution was calculated using ASIPro image viewer. The reconstructed images were not smoothed. The reconstructed PET images show that there is no difference in the measured spatial resolution during MR OFF and MR ON conditions and also when acquired outside MRI scanner.

5.4.3. Energy Resolution

The energy resolution was calculated by stepping up the threshold voltage from 350 KeV to 650 KeV [103]. Figure 5.15 shows the energy resolution for a single channel during MR OFF and MR ON conditions. The PET channel had many counts during the MR ON (FLASH) acquisition. An increase in spurious counts in the low-energy region during MR ON indicates

that these counts can be removed from the PET data by setting the low-level energy discriminator that excludes the spurious counts. There was minimal degradation in the energy resolution of the non-susceptible PET channels during the MR OFF and ON conditions. Figure 5.16 shows the ratio of the photopeaks for both conditions.

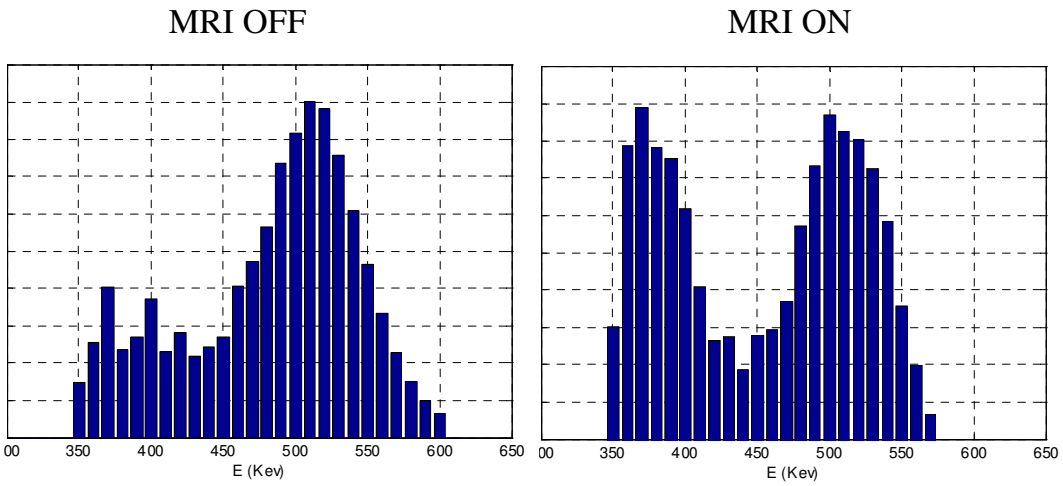

Fig. 5.15. Energy resolution of a single channel during MRI ON and OFF conditions.

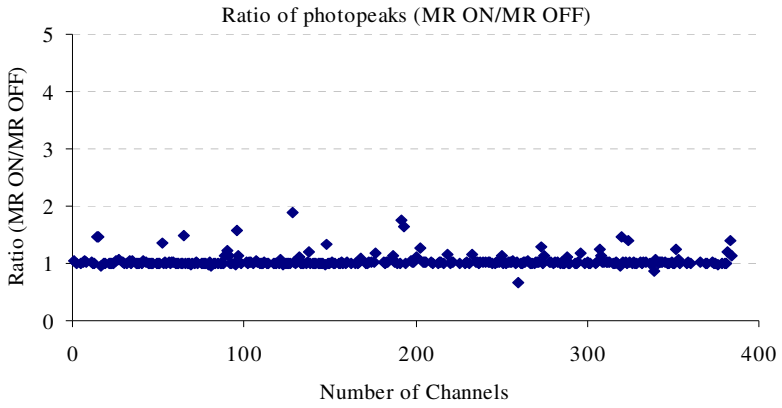

Fig. 5.16. Photopeak values of all the PET channels during MRI ON (FLASH) and OFF conditions.

5.4.4. Timing resolution

A cylindrical phantom (ID = 17mm; length = 22.2 mm) was used with eight rods pierced through its base from one end and protruding from the other end. The inner diameter of each rod was 1.22 mm. The center cylindrical chamber was filled with a solution of D_2O. Approximately 15 MBq of ^{18}F-FDG filled the eight rods of the phantom. The time resolution was calculated by selecting a wide coincidence timing window prior to data processing. The FWHM was calculated after summing the timing information from all the channels. The time resolutions for the MR OFF, FLASH and RARE pulse conditions were 10.4 ns, 10.41 ns and 10.78 ns respectively. Figure 5.17 shows the time resolution plot. The RARE sequence had minimal effect on the time resolution of the PET scanner after discarding the spurious counts.

Fig. 5.17. Time resolution comparison for MR OFF, FLASH and RARE sequences using double-layer copper shield.

5.4.5 PET calibration for activity concentration

In order to calibrate the PET images during MRI acquisition, a uniform cylindrical phantom (ID = 28 mm) that fits inside the MRI coil was used. The phantom was homogeneously filled with 1.1 MBq/ml of 2-deoxy-2-[^{18}F]fluoro-D-glucose (FDG) and carefully positioned in the active imaging regions of MRI coil and PET detector. The calibration of the radioactivity was assessed using aliquots of the solution and a calibrated sodium iodide well-counter (Picker). To

test the reproducibility of the quantitation, phantom PET data was acquired in list-mode data during active RF pulse excitation. The PET data acquisition was repeated with the same MR parameters and the two datasets were reconstructed using ML-EM algorithm and post smoothed. A large ROI was drawn on each of the cylindrical phantom PET images (avoiding the edges) to obtain mean values of the concentration of radioactivity, across all images. The calibration factors for each of the datasets were calculated by taking the ratio of well counter value to ROI-measured value.

With the MR pulsing during the PET acquisition, the noisy spikes in the PET data were gated out during offline processing, prior to image reconstruction. The calibration of the uniform cylinder phantom was obtained for the two PET datasets by drawing ROIs on the post-smoothed reconstructed PET images. The measured calibration factors were repeatable within 6 %, demonstrating the ability to acquire quantitative PET data during MR pulsing.

In summary, the effect due to the RARE pulse sequences on PET data can be observed on the sensitivity and time resolution parameters. Table 5.1 summarizes the measurements for different acquisition conditions.

Table 5.1. PET measurements for different acquisition conditions

	Sensitivity (%)	**Spatial resolution (mm)**	**Time resolution (ns)**
Outside MRI	0.30	1.22	X
MR OFF	0.32	1.19	10.4
FLASH	0.30	1.17	10.41
RARE (post-gating)	0.20	1.21	10.78

5.5. Simultaneous PET/MR imaging results of phantoms and rodents

5.5.1. Simultaneous PET/MRI: Phantom studies

A rat brain phantom made of plastic, was a 16 mm diameter cylinder (25.4 mm in length) consisting of two identical cylinders inside it with an inner diameter of 4 mm each. It was constructed to approximately replicate the two striatial regions in the brain. The two cylinders

inside the phantom were filled with 5 MBq/mL of 2-deoxy-2-[^{18}F]fluoro-D-glucose (FDG) solution with warm background in the outside cylinder with a concentration of FDG a factor of 3 lower than the 4 mm cylinders. PET and MRI data were acquired simultaneously. Figure 5.18 shows the simultaneous PET/MR image of rat striatum phantom filled with FDG in transverse view.

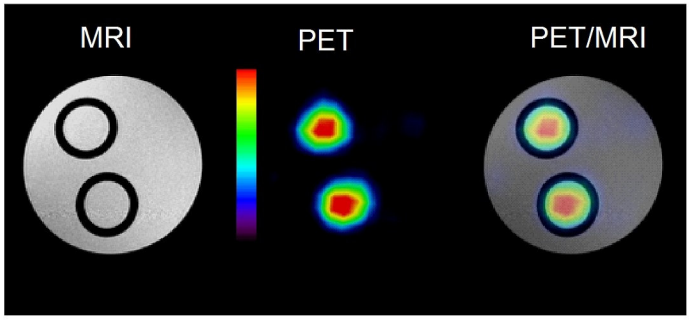

Fig. 5.18. Rat striatum phantom images filled with [^{18}F]-FDG acquired simultaneously with multi-slice proton density RARE pulse sequence.

In another experiment, the FLASH and RARE sequences were acquired during PET acquisition using a rod phantom as described in section 5.4.4. Figure 5.19 shows the simultaneous PET/MR images of the rod phantom in transverse- and coronal-views.

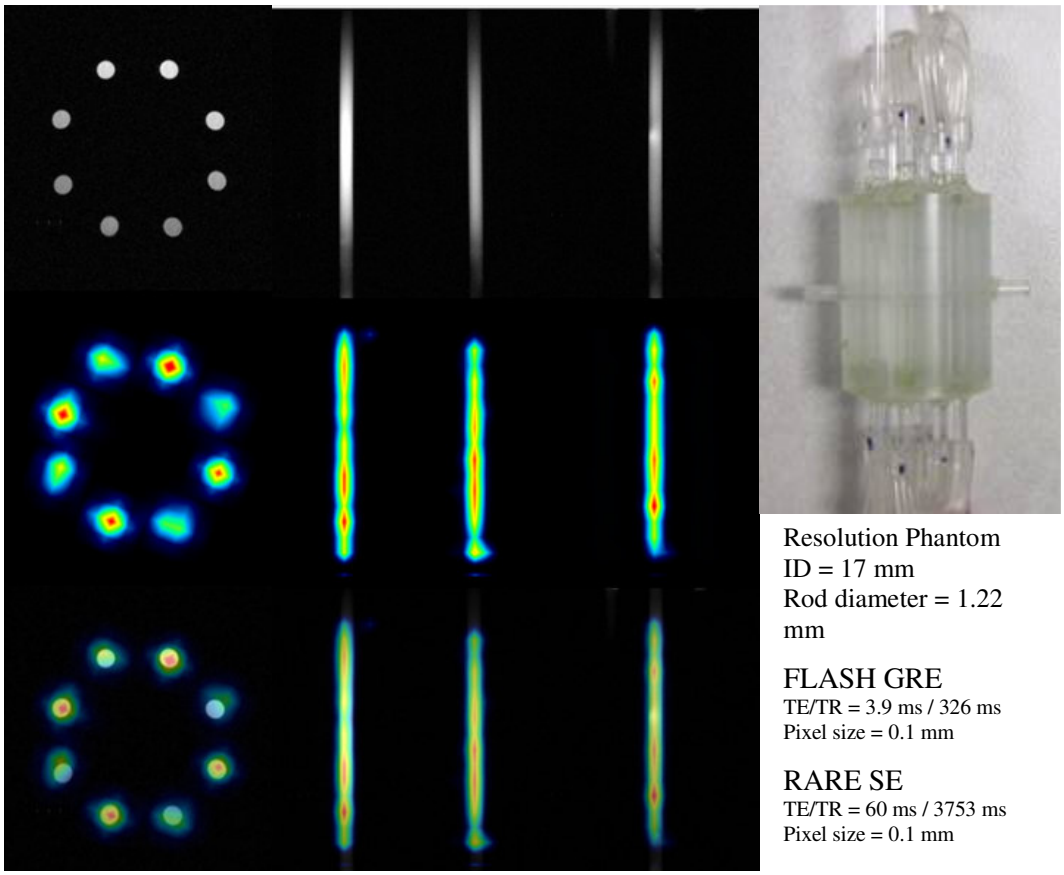

Fig 5.19. Simultaneous PET/MR images of a resolution phantom were acquired using FLASH and RARE sequences. Top: MR images; center: PET images; bottom: PET/MRI overlay.

5.5.2. Simultaneous PET/MR images of the rat brain and mouse heart

All animal experiments were approved by Institutional Animal Care and Use Committee (IACUC) at Brookhaven National Laboratory (BNL) and conducted in accordance with the *Guide for the Care and Use of Laboratory Animals*. Sprague-Dawley female rats (~260 g) were used for all the PET/MRI experiments in the 9.4 T MRI scanner. A rat head holder made of Lucite was built to support the rat's head. The rats were anesthetized intraperitoneally with pentobarbital (Nembutal, 40 mg/kg) and given glycopyrolate (0.15 ml) and saline (1 ml) along with the anesthetic for the control of salivation and hydration, respectively. To maintain anesthesia while in the scanner, the animals were exposed to a gas mixture of oxygen and isoflurane (up to 2 %). Approximately, 22 MBq of [^{18}F]-FDG radiotracer was administered intravenously through a jugular vein catheter to obtain the FDG distribution in the rat brain. PET/MRI data was acquired 30 minutes post-injection. In another rat experiment, approximately 29 MBq of [^{11}C]raclopride was administered intravenously to assess dopamine D2 receptor

availability in the brain.

Swiss-Webster male mice (25 – 30g) were used for cardiac PET/MRI studies. The rat head holder on the animal platform was replaced with a custom-made mouse holder made of G10 plastic material. Physiological monitoring probes were connected to the forepaws of the mouse and the holder was secured in the animal tube assembly. The mice were anesthetized using the same method as with the rats. Approximately 11 MBq of [^{18}F]-FDG was administered through tail vein injection and PET/MRI data were collected 30 minutes post-injection.

The animals were scanned with physiological monitoring probes attached. Vital signs such as pulse rate, respiratory rate, electrocardiogram (ECG) and body temperature (constantly maintained at 37^{0}C) were monitored and recorded during the scans, using MRI-compatible small animal monitoring system (SA instruments, Stony Brook). ECG gating technique was used to extract the ten individual phases of the mouse cardiac cycle. Each phase of the cardiac cycle (R-R interval) is framed into 10 millisecond bins to obtain the dynamic MR image of the mouse heart. The PET images are also R-wave gated by synchronizing the data acquisition with the MRI gating pulse. The transistor-transistor logic (TTL) input signal from the ECG gating device is directly fed into the PET signal processing module (TSPM), which triggers the gating pulse in the PET list-mode data. The PET data was binned into ten 10 millisecond frames which are accurately co-registered with the MR image frames. Data from each of the 10 millisecond frame is summed with the corresponding temporal frame to form an image. This resulted in ten PET frames that exactly correspond with the ten MR frames in time.

Standard MR sequences included a FLASH gradient echo sequence and RARE spin echo sequence. A list of MRI scanning protocols for animal scans is summarized in table 5.2. The PET and MR images were co-registered using PMOD version 2.75 image fusion software. The MR image is loaded as a reference study file. An orthogonal layout was selected to display all the planes. The PET image was loaded as a reslice file and was matched spatially with the MR reference file.

Table 5.2. MRI scanning protocols for simultaneous PET/MRI acquisition.

Parameter	**Rat brain ^{18}F-[FDG]**	**Rat brain (^{11}C)**		**Mouse heart**
Sequence	FLASH – 3D	RARE	FLASH – 3D	FLASH – 3D *Cine*
Matrix size	256 x 128 x 128	256 x 256	256 x 256 x 256	86 x 256 x 860
Time to echo, TE (ms)	3.4	39.4	3.4	2.7
Repetition time, TR (ms)	15	2500	15	10
Field-of-view (mm^2 / mm^3)	51.2 x 25.6 x 25.6	76.8 x 38.4	38.4 x 76.8 x 38.4	42.8 x 21.4 x 21.4
Slice thickness (mm)	0.2	0.9	0.15	0.167
Pixel size (mm)	0.2	0.15	0.15	0.249
Flip angle (degrees)	15^0	180^0	15^0	10^0
Scan time	16 min 29 sec	5 min 33 sec	33 min	34 min 54 sec

The rat brain MRI, PET and co-registered images acquired using [^{18}F]-FDG in Figure 5.20 show the glucose distribution in the brain. The FDG localization is noticeable in Harderian glands and in different regions of the brain.

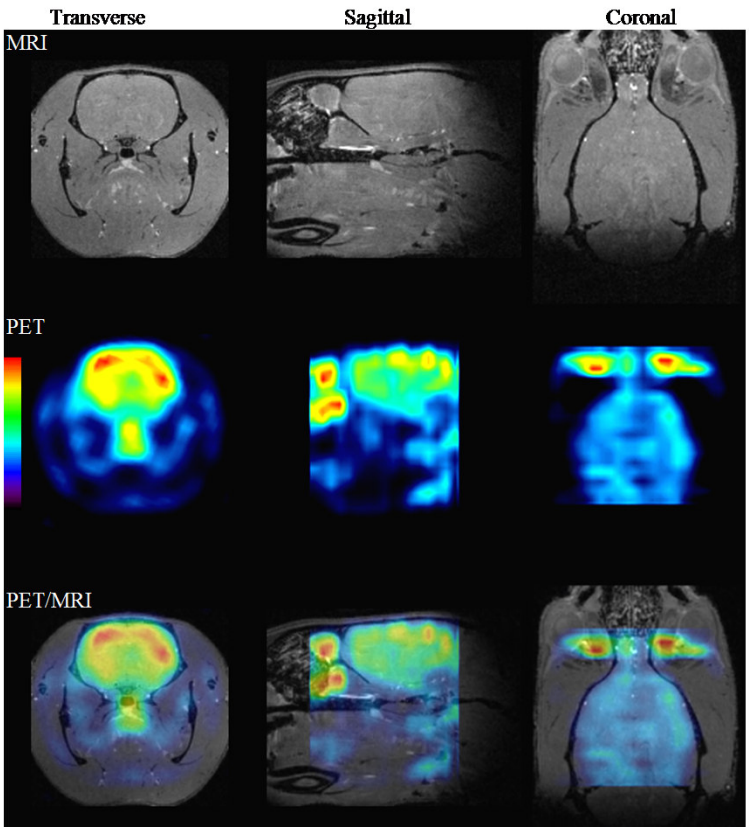

Fig. 5.20. Simultaneous PET/MR images of a rat brain administered with [^{18}F]-FDG using FLASH-3D isotropic MR pulse sequence (row 1: MR images; row 2: PET images; row 3: PET/MRI overlay) in transverse (column 1), sagittal (column 2) and coronal (column 3) views, respectively.

The [^{11}C]raclopride uptake mainly in the striatum of an anesthetized rat brain in transverse and coronal views are shown in figures 5.21(a) and 5.21(b), respectively, using different MRI pulse sequences described in table 5.2. Figure 5.21(c) shows both the MRI and PET temporal frames of a 10-frame FLASH cine MR sequence of a mouse cardiac cycle.

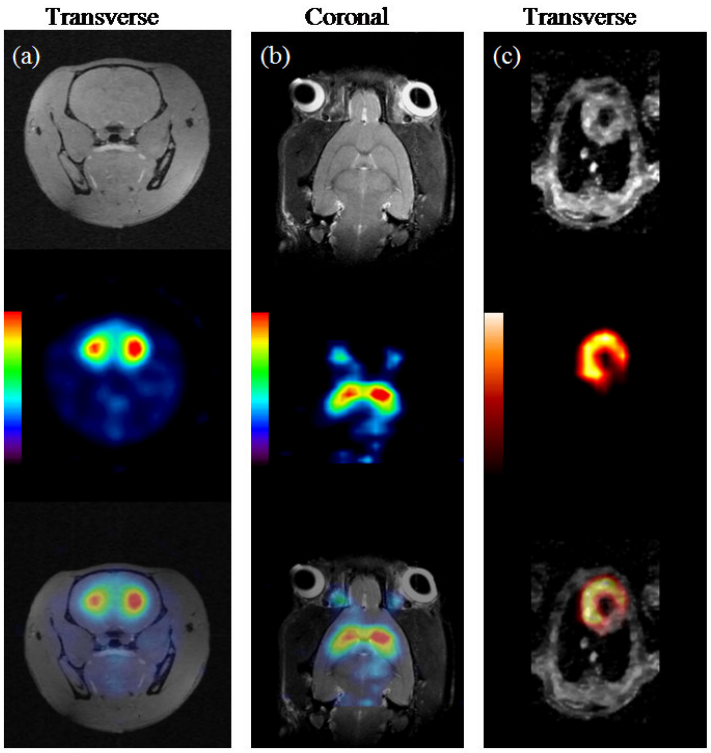

Fig. 5.21. Rat brain PET/MR images administered with [11C]raclopride shows the dopamine receptor binding in the striatum, in transverse view (a) acquired with FLASH isotropic pulse and in coronal view (b) acquired with RARE pulse sequence. (c) Simultaneous *cine* PET/MR gated cardiac image of a mouse heart in transverse view showing one of the cardiac phases. The slice thickness of the MR image is matched with that of the PET image (1 mm). The rat brain and mouse heart images demonstrate the ability to perform scans using the same PET/MRI setup.

In addition, MR Spectroscopy (MRS) data and echo-planar imaging (EPI) sequences from a rat's brain were obtained when the PET was ON, as depicted in Figure 5.22. Each of the metabolites was clearly discernable from the MRS spectrum, and good-quality MR images were acquired using the EPI sequences.

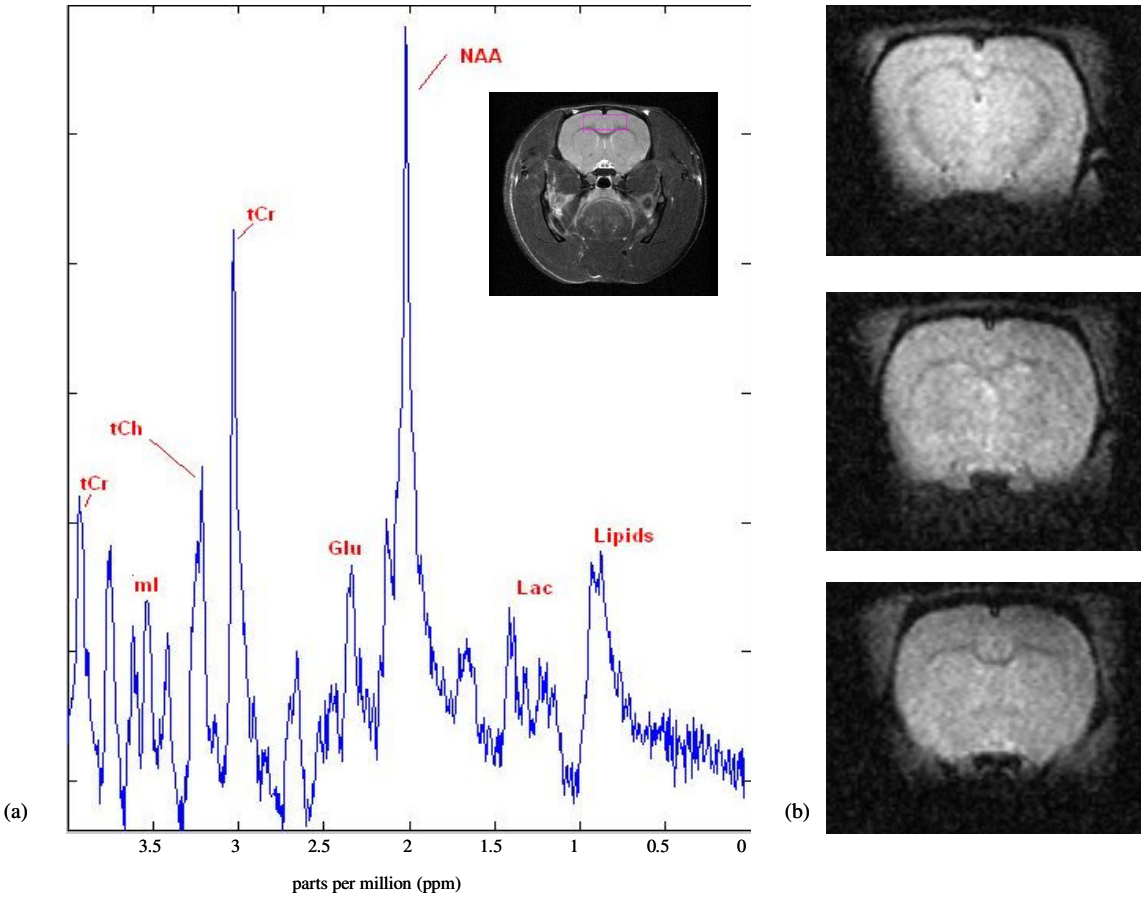

Fig. 5.22. MRS of the rat brain showing different metabolites therein, obtained during a PET acquisition (left). Transverse slices of Echo Planar Image (EPI) of a rat's brain acquired during the PET ON condition (right).

5.5.3. PET/MRI co-registration

For the current PET/MRI setup, the RF coil is secured into the PET detector. The offsets in X, Y and Z directions are dependent on the mechanical alignment of the spatial imaging volumes. The mean offsets in X and Y directions were < 0.5 mm. The offset in Z-direction is < 1.5 mm. This is due to the variations in the alignment between the RF coil and the PET system. The image co-registration is performed in PMOD fusion software (version 2.75). The orthogonal slices of PET and MR images were overlaid. In addition, the PET images were rotated in sync with the oblique MR image acquisitions (e.g. cardiac mouse imaging).

5.6. Chapter Summary

- Optimum grounding topology was identified and implemented. The cable shield was grounded at multiple points to minimize the inductance and obtain low ground

impedance. The voltage potential between the signal at the power supplies dropped from 120 mV to 0 mV.

- The effect of the RF fields on the PET detector was suppressed by using thin sheets of segmented copper, offset at the segments. Spurious counts that peaked at ~ 8 million counts per second were suppressed to ~1 million counts per second with double-layer shield.
- Good-quality MR images also were obtained in the presence of copper shield; there was a ~35 % degradation of the SNR in the RARE MR images, compared to SNR with no PET in the field of view. The loss in the SNR can be compensated by taking a greater number of signal averages to improve the signal in the MR images.
- The PET detector performance was evaluated after choosing the double-layer copper shield as an optimum shield for the PET/MRI studies. There was no significant degradation on the spatial resolution and time resolution of the PET scanner during MR ON and OFF conditions.
- The energy resolutions during both MR ON- and OFF conditions are comparable. Interestingly, all the spurious counts occur in the low-energy region, which can be windowed to minimize their effect on PET images.
- The difference in the time resolution is not significant after discarding the spurious counts during the RARE acquisition.
- A significant drop in the sensitivity was observed (0.2% vs. 0.3%) when the PET data was acquired during RARE sequence.
- Simultaneous PET/MR images were obtained using phantoms and *in vivo* imaging studies in rats and mice were carried out to demonstrate the feasibility of our approach.

The next chapter will analyze the results obtained with the shielded enclosure and will emphasize on the justification of electromagnetic shielding for the PET/MRI studies, followed by some of the limitations in the study.

CHAPTER 6: ANALYSIS OF PET/MRI EXPERIMENTAL RESULTS AND DISCUSSION

The previous chapter mainly focused on the shielding and grounding arrangements for performing PET/MRI studies with minimal electromagnetic interference. The performance of the PET and MRI systems were evaluated to identify the acceptable limits for *in vivo* quantitative simultaneous acquisition of structural and metabolic information in small animals. This chapter describes some of the significant parameters that have contributed in enhancing RF noise isolation and further discusses the potential impediments of our PET/MRI setup.

6.1. The motivation for employing shielding around the PET detector housing

One of the key points that was highlighted in Chapter 3 was the temporary purging of counts in some of the susceptible PET channels during RF pulsing. The injection of RF currents that play a vital role in disturbing the sensitive PET read-out chain is inevitable if there is no shielding from the high intensity electromagnetic source. The PET electronics need to be protected from the outside environment to perform to their ability without any compromise. There is a considerable amount of literature that describes the importance of implementing practical shielding methods at RF and microwave frequencies. Electronic systems such as antenna and defense systems, military aviation and communication systems, demand high levels of shielding to absorb interference from either the outside environment or from the other electronic components residing in close proximity. Likewise, the RF coil and the PET detector must perform without interfering with each other. Since the main objective of the dissertation is to describe ways to minimize the undesirable effects of EMI, there is a need to quantify and define the acceptable limits and perform tradeoff analysis.

When the need for electromagnetic shielding was realized for PET/MRI studies, some of the PET shielding methods were utilized, as described in Chapter 5. The following subsections describe the justification for using different shields:

6.1.1. Aluminum shield

To investigate an optimum shield around the PET electronics, the PET detector was housed in an aluminum case as shown in Figure 6.1. This arrangement provides a continuous shield and the PET electronics are effectively shielded from the external RF fields.

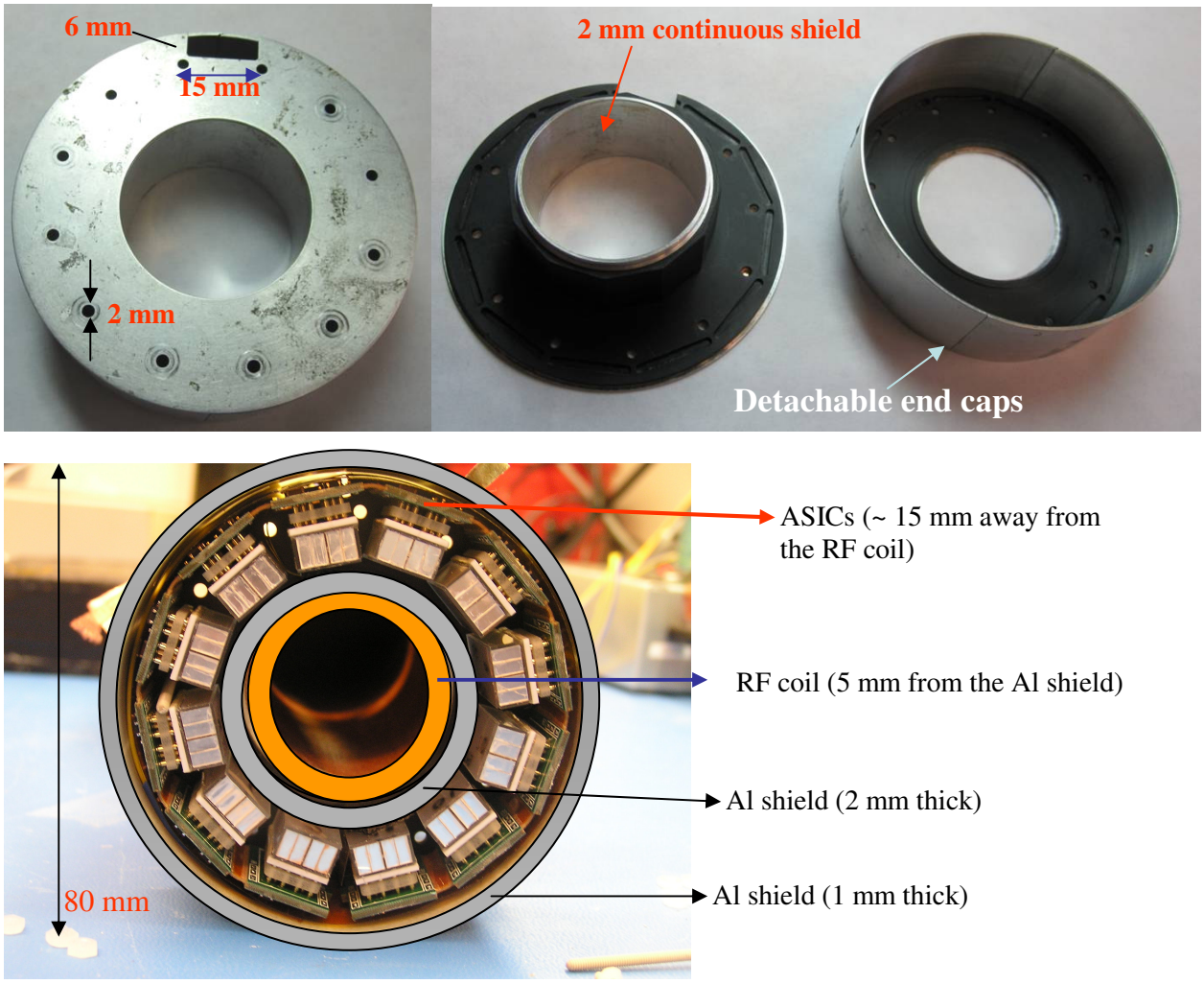

Fig. 6.1. Continuous aluminum housing for PET system.

The outer aluminum endplates and end caps are 1 mm thick. The thickness of the inner sleeve is 2 mm. The RF coil resides inside this inner sleeve. It is assumed that the RF fields originating from the coil create currents on this inner sleeve shield, since the region surrounding the sleeve is considered the active region of the coil. The RF currents are eventually absorbed or reflected from the 2 mm thick shield, as shown in the previous chapter. Therefore, the aluminum case should be an effective shield that has the capability to nullify the effect of RF impinging on the shield. This shield is an extreme contrast compared to an unshielded housing condition. However, the effect of RF in the PET data was still evident in spite of creating a Faraday-cage-like shield around the PET electronics. At 400 MHz, the shielding effectiveness for aluminum in near-field conditions can be calculated as:

$$SE_{(dB)} = A_{(dB)} + R_{(dB)}$$

Here, $A_{(dB)} = 131.4 * t * \sqrt{f * \mu_r * \sigma}_r$ dB and $R_{(dB)} = 14.6 + 10\log\left(\frac{fr^2\sigma_r}{\mu_r}\right)$ dB

Substituting for

μ_r = relative permeability of the aluminum = 1

σ_r = relative conductivity of the aluminum = 0.61 [137]

t = thickness of the aluminum in meters = 0.001 m

r = distance of aluminum from RF source in meters = 0.005 m

$A_{(dB)} = 131.4*0.001*\sqrt{4*10^8 *1*0.61} = \underline{2052.5}$ dB

$R_{(dB)} = 14.6 + 10\log\left(\frac{4*10^8 *(0.001)^2 *0.61}{1}\right) = \underline{38.47}$ dB

Therefore, the overall shielding effectiveness for 1 mm thick aluminum at 400 MHz is

$$SE = 2052.5 + 38.47 = 2091 \text{ dB}$$

From the above theoretical calculation, the value of SE is more than sufficient to eliminate any RF interference on PET electronics at 400 MHz. Although the thickness has helped in suppressing the noise currents drastically, it did not eliminate the noise on the PET completely. From the electromagnetic theory and the skin effect behavior at high frequencies, it can be deduced that the RF current density is maximum along the surface of the aluminum shield that is only few micron skin depths thick since the skin depth is only 4 μm at 400 MHz. The rest of the metal thickness is redundant. Therefore, the thickness term in the calculation of the absorption loss can be considered as an overestimated value. A shielding effectiveness of over 90 dB is considered an excellent shield for practical EMI applications [110]. It must be noted that there are seams near the mating surfaces of the aluminum end plates, where the shield can break if there isn't enough solid contact or pressure. Some of the other possible explanations for interference are given below:

- Distance between the RF coil and the shield: In the reflection loss calculation mentioned above, the distance between the source and the shield is assumed to be 5 mm. The overall reflection loss is much less compared to the absorption loss term because the reflection loss does not depend on the shield thickness. When dealing with near-field conditions

(i.e. source to shield distance < $\lambda/2\pi$), the electric and magnetic fields are considered separately [119, 121]. This is because the shielding effectiveness for near-field sources depends on the type of source (electric or magnetic) and the intrinsic impedance of the shield. Another significant parameter is the magnitude of the wave impedance against distance (r) from the source. In a near-field condition, the magnetic field is proportional to $1/r^3$, if the source is magnetic. For an electric source, the magnetic field is proportional to $1/r^2$ in near field. Therefore, if the RF coil is assumed to be a dominant magnetic field source, its magnitude is proportional to $1/r^3$ distance from the PET electronics in the housing. In reference [121], a qualitative summary of shielding effectiveness chart is presented, where it is mentioned that the magnetic field reflection loss (and hence the shielding) is less if the distance between the source and the shield is less and where proximity effects take over.

- Shield connection to the ground plane: Another important factor is how well the shield is connected to the ground plane. The RF currents flowing on the surface of the shield must find a path of low impedance to drain the RF into a solid ground plane. Also, the integrity of the ground plane to which the shield is connected is believed to be crucial. This is because the RF currents may flow only at one end if there is a break in the ground plane connection because they can create RF potentials. Floating shields are considered ineffective shields if they are not terminated to ground [118].
- Parasitic capacitances between the RF coil, aluminum shield and PET electronics: There is a possibility that the RF signals may still leak into the shield through the parasitic capacitance. If there are high RF voltage potentials developed across the coil and the shield, and the shield and the PET electronics, RF currents are created through the stray capacitance in the environment. In general practice, the integrated circuit chips are packaged by covering the chip surface with a copper foil to ground. This ensures the suppression of any stray capacitance around the chip. The front-end electronics of the PET detector include 12 ASICs. There is no copper foil/tape on the chips of the PET detector. Since the shield, the RF coil and the electronic circuits are constricted in a closed region, the stray capacitance between them may complete the loop and change the path of alternating currents pulsed by the RF coil. Imperfections in the shield may also lead to increase in the stray capacitance and further boost spurious RF coupling.

- Imperfections in the shield: Although the shielding effectiveness is defined as the summation of absorption and reflection losses [110, 112, 119, 124], the handbook on electromagnetic shielding redefined shielding effectiveness for imperfect shields as [138]:

  SE = A + R + M – Leakage effects – Standing waves, where

  A = absorption loss; R = reflection loss; M = multiple reflections.

  The leakage effects include apertures, holes, seams, cracks etc. The effect of standing waves in electromagnetic shielding can become significant in near-field conditions with the RF fields reflecting at cavity resonances. In the PET detector housing with aluminum, the signal and power traces of the PET detector from the flexible printed circuit board (PCB) are routed through a thin PCB layer, which is 150 mm long, 10 mm wide and 1 mm thick. This trace exits the shield from a 15 mm x 6 mm rectangular slot on the aluminum endplate. Although, the linear dimensions of this opening are much smaller compared to one wavelength of RF at 400 MHz (75 cm), there is a possibility of the PCB traces and electronic components coupling to the external RF fields, through this opening. To further illustrate the point, an experiment was conducted with and without shielding the open slot. The RARE and FLASH sequences were pulsed for both conditions and the list-mode PET data were acquired. Figure 6.2 shows the RF spikes in the singles PET counts histogrammed in 1 ms time bins, for RARE pulse sequence.

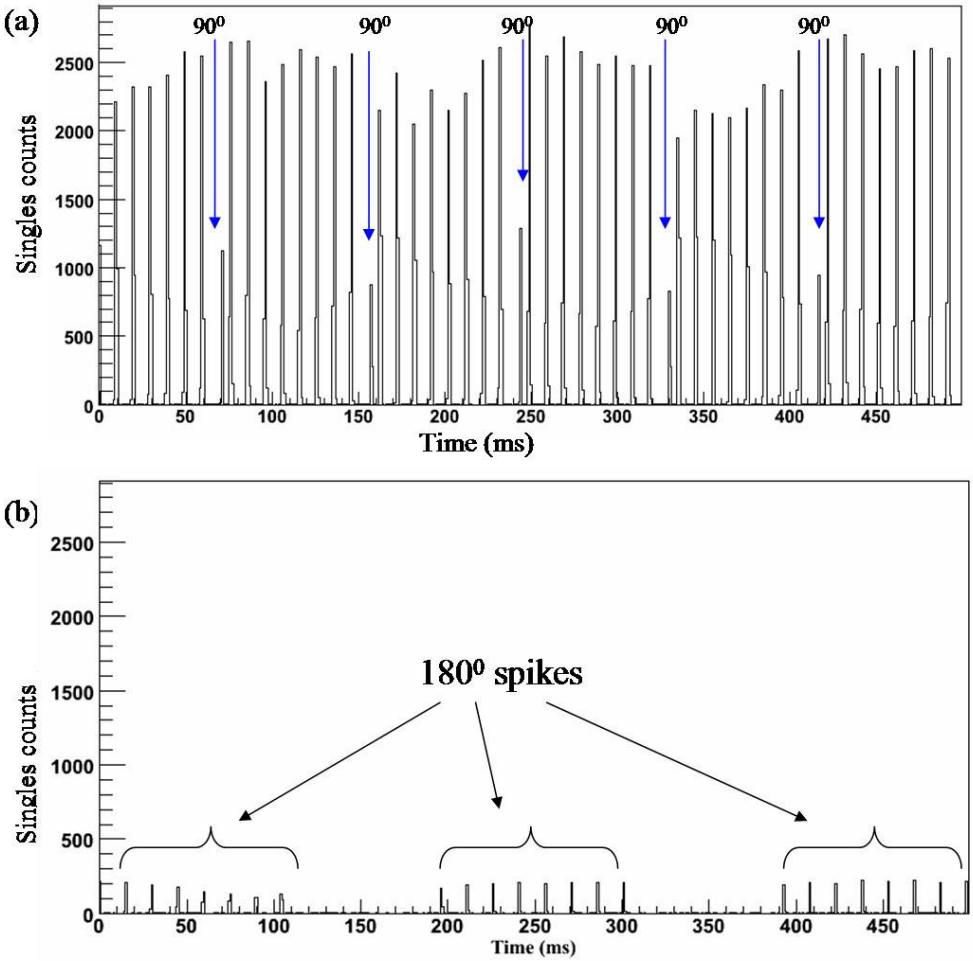

Fig. 6.2. RF spikes without (top) and with (bottom) shielding the slot where the PCB traces exits the aluminum endplate.

From the above figure, it is clear that the magnitude of the RF spikes were significantly larger when the slot was not covered. It must be noted that the number of MR acquisition slices (hence, the repetition time TR) are different for the two conditions. But the pulse duration and the pulse type (sinc3 pulse) remain the same for both conditions. Another observation from the plot with the slot-shielded condition is that the RF spike contribution from the 90^0 RF pulse is missing, compared to the plot with the slot-unshielded. In other words, the 90^0 pulses were attenuated by closing the slot. The 180^0 refocusing pulses were not attenuated in either condition, indicating that the power levels utilized for refocusing pulses were greater than the 90^0 pulse. For FLASH sequences, the interference was completely eliminated in the slot-shielded condition. Figure 6.3 shows the comparison of the effect of slot-shield in the aluminum housing for singles count rate.

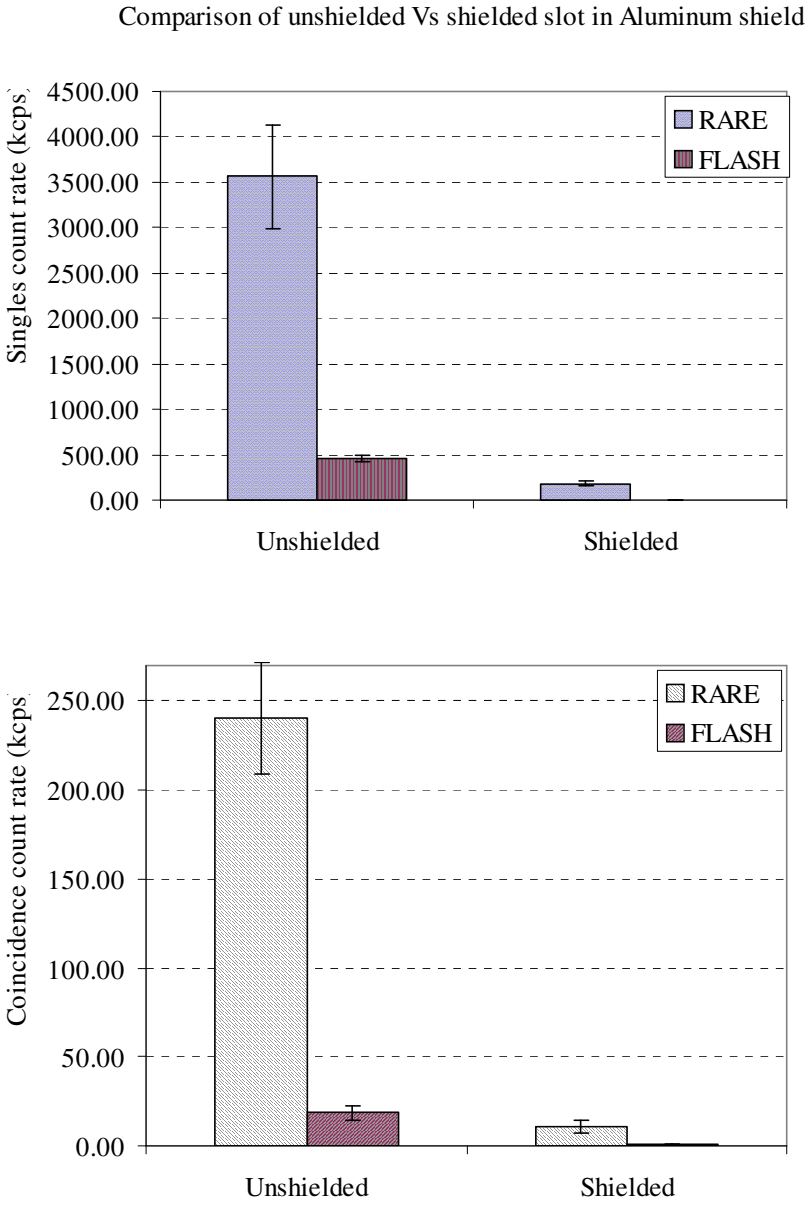

Fig. 6.3. Singles and coincidence count rate for unshielded and shielded slot in aluminum shield.

In another experiment, the low level discriminator (LLD) energy threshold of the PET was varied for the unshielded slot. The energy window for routine PET scans is set at 350 keV to 650 keV. At the upper level discriminator (ULD) threshold at 650 keV, none of the PET counts will be triggered. However, during RARE pulse acquisition, considerable PET counts were registered even at 650 keV threshold for unshielded slot condition. From the PET detector block hitmap, it was identified that all the counts were coming from a single block detector out of all the 12

detector blocks. This detector block is close to the slot opening through which the PCB traces exit the PET housing. This observation demonstrates that the RF fields can enter into a shield with even minimal openings.

6.1.2 Shielding effectiveness for aluminum shield: Theoretical evaluation

The aluminum shield with a open slot from where the PCB traces (tether) exits the shield can be considered as an example of a conductive shield with an open slot. The shielding effectiveness for a slot in the shield is given by [117]

$$SE_{dB} = 100 - 20\log l_{mm} - 20\log f_{MHz} + 20\log\left(1 + 2.3\log\frac{l_{mm}}{h_{mm}}\right) + 30\frac{t_{mm}}{l_{mm}} \text{ where}$$

l_{mm} = linear dimension of the slot in mm

f_{MHz} = frequency in MHz

h = slot height in mm

t = thickness of the slot (= thickness of the shield) in mm

The dimensions for aluminum shield are given below:

l_{mm} = 15 mm; f_{MHz} = 400.32 MHz; h = 6 mm; t = 1 mm

Substituting the above values in the equation,

$$SE_{dB} = 100 - 20\log 15 - 20\log 400.32 + 20\log\left(1 + 2.3\log\frac{15}{6}\right) + 30\frac{1}{15}$$

$$SE_{dB} = 36.28dB$$

Therefore, the 1 mm thick aluminum shield provides only ~36 dB attenuation because of the slot dimensions. In order to achieve at least 75 dB attenuation, the slot dimensions should be as small as 1 mm. It also suggests that the thumb rule of λ/20 at 400 MHz might not yield a good attenuation. Rather, apertures as small as λ/50 provides attenuation from the RF fields, especially if the RF coil is in such close proximity to the shield. Experimental results reported by Sharma *et al.,* concluded that the RF noise suppression was possible when the physical dimensions of the apertures were kept smaller than 30 mm at 200 MHz frequency (λ/50) [123]. For a 100 MHz frequency source, it is suggested that the apertures should not exceed 10 mm [117]. From the above theoretical evaluation, it can also be deduced that that thickness of the shield is not significant if there are imperfections in the shield. In addition, the slot height does not contribute

to the degradation of the SE. It is the slot length that creates a complementary dipole antenna near the shield.

From the observations made so far, it is clear that the RF can leak into the Faraday cage if the shield is not perfectly covered. In addition, the PET electronics can act as unintentional antennas even though they are electrically short. As discussed in Chapter 4, the rule of thumb [117, 118, 123] for many EMC applications is to have the linear dimension of the apertures or seams less than 1/50 wavelength. From table 4.1 in Chapter 4, the RF wave is 75 cm long at 400 MHz. For isolating RF leaks, the physical dimensions of the apertures or slots must be less than 1/50 wavelength or < 15 mm at 400 MHz. To further understand this phenomenon, the slot acts like an aperture through which the PCB traces and the other digital read-out electronics can 'see' the RF fields from the inside. The impinging RF fields on the aluminum shield attenuate and reflect off the shield. However, the resultant currents on the outside of the shield will generate reactive fields and cause RF potentials across the slot which will act as sources of re-radiation. This is an example of complementary dipole antenna as was discussed in Chapter 4. Therefore, it is necessary to create a near-perfect Faraday cage around the components that requires protection from RF without any openings. As discussed above, the shield can be bonded to a solid ground plane. Figure 6.4 shows the shielding not only around the sensitive PET detector, but also throughout the PET power and data cables. Copper shields were used to cover the PET cables. This shield is bonded to the TSPM enclosure that connects to the chassis ground of the power supplies.

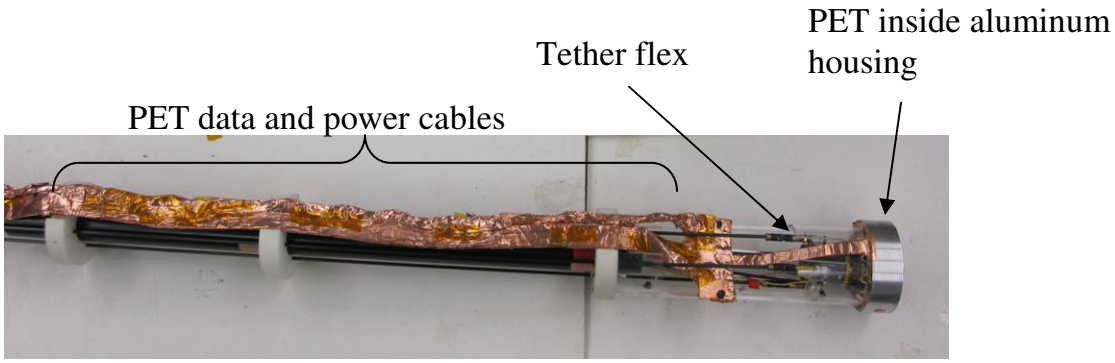

Fig. 6.4. Copper shielded arrangement to shield the PET assembly completely.

A continuous Faraday cage around the PET assembly is desired. The shield is bonded to the chassis ground and the signal returns to create a low-impedance ground, as discussed in Chapter 5. The PET signal processing module (TSPM board) secured in an aluminum box was also

sealed to contain the RF interference from the clocks and other digital activity on the board. This arrangement also helped in eliminating the interference picked up by the RF coil observed at 400 MHz. Figure 6.5 shows the power return-loss reflection coefficient plots of a tuned RF coil before and after shielding the TSPM box.

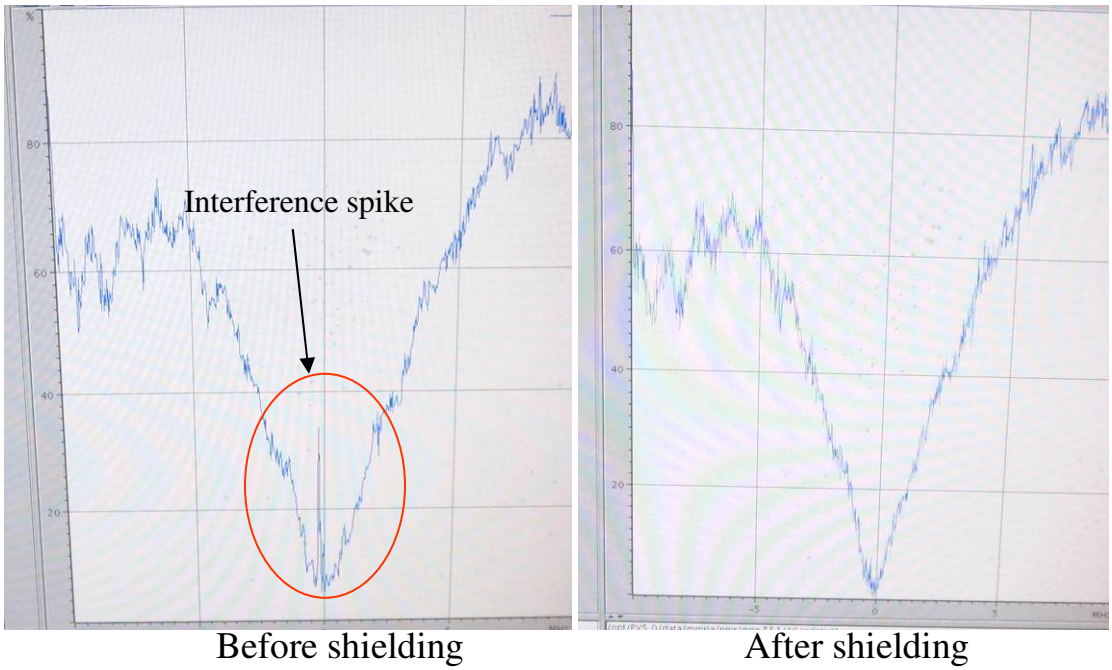

Fig. 6.5. Power-return loss reflection plots showing the interference spike before the shielding and no spike after the shielding.

The MR images acquired with the aluminum shield were poor in SNR and were mainly degraded due to the eddy current effects, as shown in Figure 5.11 in Chapter 5. The coupling between the coil and the imaging sample must be maximized for obtaining MR images with higher SNR. However, the presence of a continuous metal shield in 5 mm proximity of the RF coil would alter the coil inductance and disturb the overall coupling mechanism with the imaging sample. Although the poor quality from the MR images using the aluminum shield was expected, the main goal was to find out if the interference on PET can be minimized or completely eliminated using a thick shield. To identify a tradeoff between obtaining good quality MR images and enhancing RF isolation, thin sheets of copper layers were used.

6.1.3 Single-layer copper shield

With the exception of the PET detector ring, the shielding of the rest of the PET data and signal cables was the same as described in the previous section. Since the RF currents circulate

only on the surface of the conducting shield at 400 MHz, a thin copper layer is adequate for a good shield. The copper layer had a thickness of 18 µm and was deposited on a dielectric substrate (kapton) that had a thickness of 54 µm. This copper thickness corresponds to five skin depths capable of providing good shielding [116]. The endplates, the outer and inner sleeve dimensions of the PET detector were used as a template to make the copper layer using PCB technology. To minimize the effect of eddy currents during MR imaging, the copper layer had etched segments spaced at equal distance from each other. The concept of slotted RF shields is not uncommon in designing RF coils for MR imaging. The copper shields with segments are used in the design of transmission line RF resonators to avoid undesired coupling between the RF and gradient fields, in addition to minimizing the effect of eddy currents [139-143]. Figure 6.6 shows the two copper layers for each of the endplates and one segmented copper film that covers the outer ring. The inner ring is double-layer copper with segments and is offset at the segments (not shown in the figure). A single layer of copper was glued with epoxy to the unshielded plastic housing. The copper film was glued on the inner rim of the outer ring. Each of the copper layers was connected at the inner ring with copper tabs interconnecting all the layers. Although, the inner sleeve of the PET ring is attached with a double-layer copper, the rest of the surfaces were glued with single-layer copper. For conventional clarity, this shield is referred to as single-layer segmented copper shield.

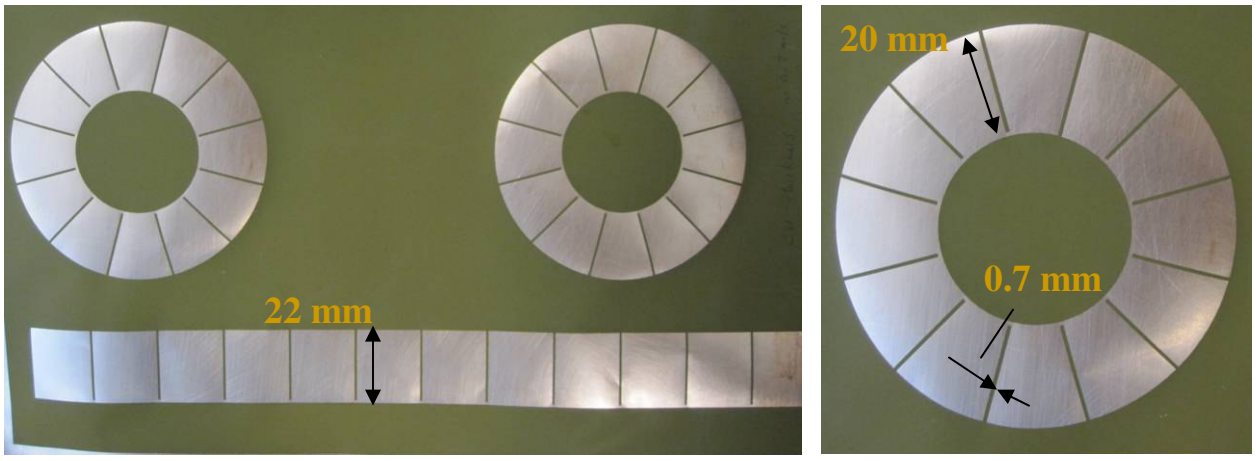

Fig. 6.6. Thin layers of copper with segments etched on a PCB substrate made of kapton.

The results from a single-layer copper shield were not encouraging compared to the aluminum shield in attenuating the RF spikes. One of the main reasons is the breaks in the

copper shield. The segment in the shield is an example of a *seam*. The linear dimensions of the 12 axial segments on the copper layer, as seen in the Figure 6.6 are 20 mm on the end plates and 22 mm on the outer copper film. The width of the segment is 0.7 mm. For a single slot dimension, the shielding effectiveness is calculated using the formula given in section 6.1.2.

$$SE_{dB} = 100 - 20\log 22 - 20\log 400.32 + 20\log\left(1 + 2.3\log\frac{22}{0.7}\right) + 30\frac{0.018}{22}$$

SE_{dB} = 34.76 dB

In addition, there are 12 circular holes each having a diameter of 2 mm. Compared to the linear dimensions of the slot exiting the aluminum shield as discussed in section 6.1.1, the RF coupling will be more predominant because of these axial gaps. Each of the segments can be considered as a long narrow slot or a seam. The segments are acting as slot antennas considering the complementary dipole. Since the segments and holes in the shield are an example of multiple apertures that have the linear dimensions less than ½ wavelength, the decrease in the shielding effectiveness is proportional to the square root of the number of apertures [144].

$$SE = -20\log\sqrt{n} \qquad \text{or}$$

$$SE = -10\log n \quad \text{(dB)}$$

where n is the number of apertures that are equal in linear dimensions and closely spaced. There are 12 segments on the outer copper film, the total number of apertures will be 36 (12+12+12), not considering the evenly spaced 2 mm diameter holes and slots on the inner copper film with two layers and offset. Therefore, the decrease in the shielding effectiveness is

$$SE = -10\log(36) = -15.56 \text{ dB}$$

The overall decrease in the shielding effectiveness with less than ½ wavelength linear dimension including the number of apertures is given by

$$SE = 20\log\left(\frac{150}{f_{MHz} * l_{meters} * \sqrt{n}}\right) \text{ dB}$$

Substituting the values at 400.32 MHz and considering 36 apertures having an average linear dimension of 21 mm, the decrease in SE is

$$SE_{(Copper)} = 20\log\left(\frac{150}{400.32 * 0.021 * \sqrt{36}}\right) = 9.5 \text{ dB}$$

From the above equation, it is clear that the fewer the number of apertures and the smaller the linear dimension, the better the shielding that can be achieved. Figure 6.7 shows how the SE drops with the increase in number of slots and the linear dimension at 100 MHz and 400.32 MHz frequency.

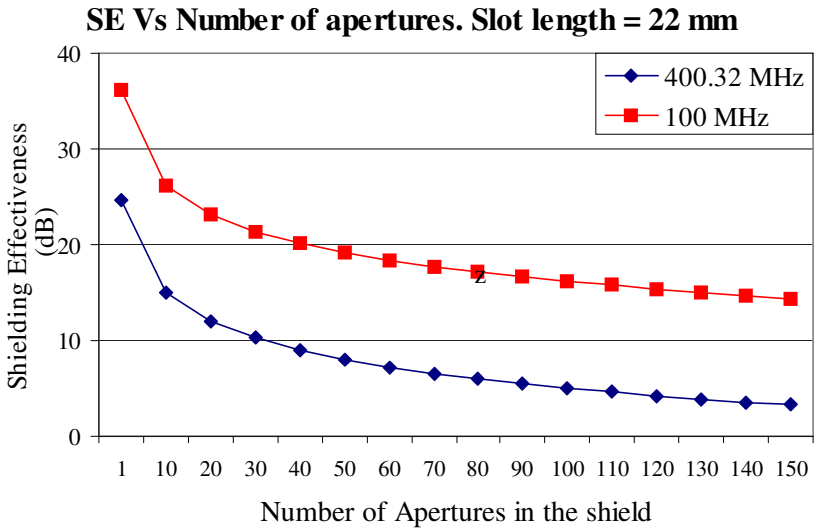

Fig. 6.7. Shielding effectives as a function of number of apertures (linear dimension is assumed to be 22 mm).

6.1.4. Evaluation of shield thickness for optimum shielding effectiveness

For theoretical estimation of SE, the thicker the shield the higher the absorption loss; therefore the shield should provide the best SE against stray RF fields. However, as it was discussed in previous sections, the seams and apertures spoil the SE at higher frequencies. It is reiterated that the thickness term in the SE equation has minimal impact on the overall improvement of the SE. Figure 6.8 below shows the SE as a function of copper shield thickness for 36 slots, each having a slot length of 21 mm. The SE is calculated for a copper thickness of 10, 000 µm (10 mm). Although there is an increase in the SE at 10 mm copper, the thickness below 1000 µm (1 mm) does not significantly contribute to the SE. In other words, a shield thickness of 10 µm is as good as a shield thickness of 1000 µm. It requires 100 times the shield thickness to achieve a moderate SE from 9.5 dB to 11 dB. Moreover, a 10 mm thick shield for isolating the RF fields for PET/MRI applications is impractical and undesirable.

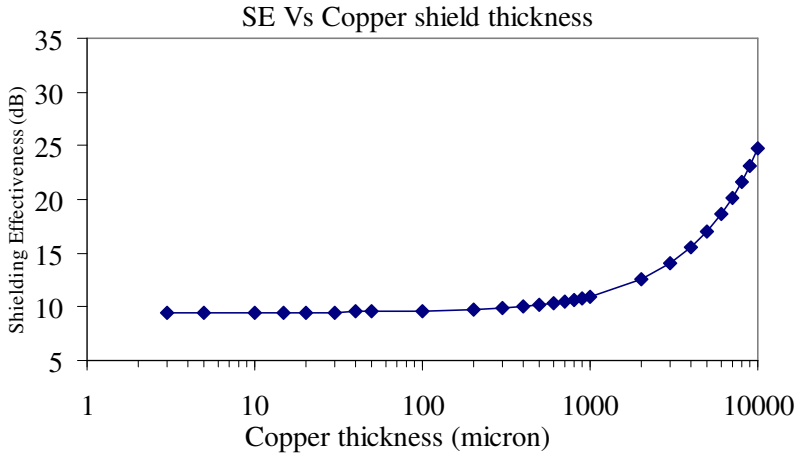

Fig. 6.8. Shielding effectiveness as a function of copper thickness for a total of 36 slots (21 mm slot length).

On the other hand, figure 6.9 shows the increase in the SE with the decrease in the slot dimensions at 400.32 MHz. for 36 slots. The SE is also plotted at 106 MHz frequency corresponding to the PET system clock, as shown in figure 6.10.

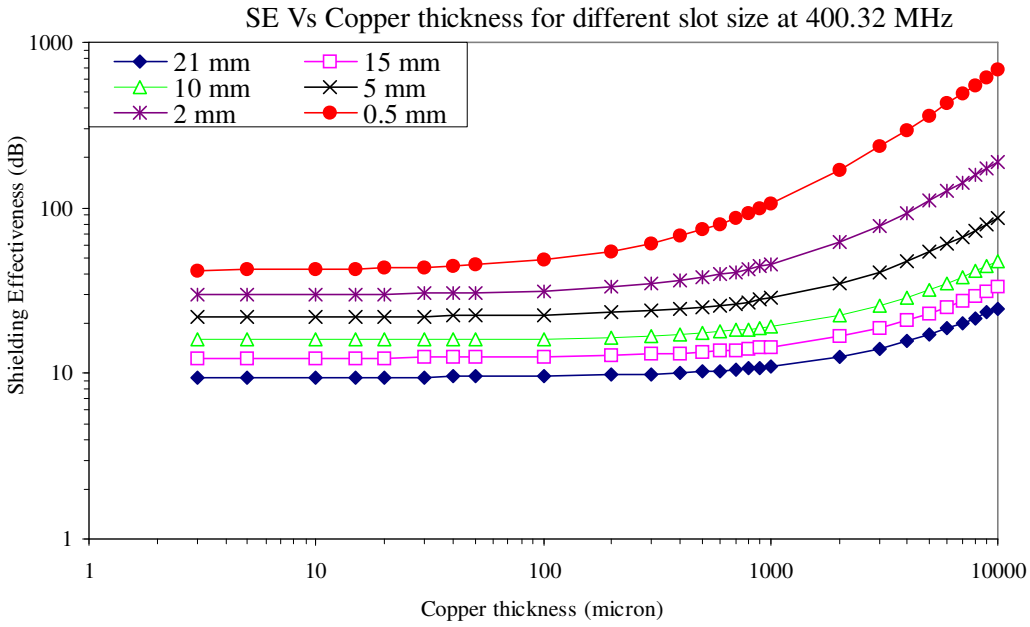

Fig. 6.9. Shielding effectiveness with 36 slots for various slot lengths at 400.32 MHz.

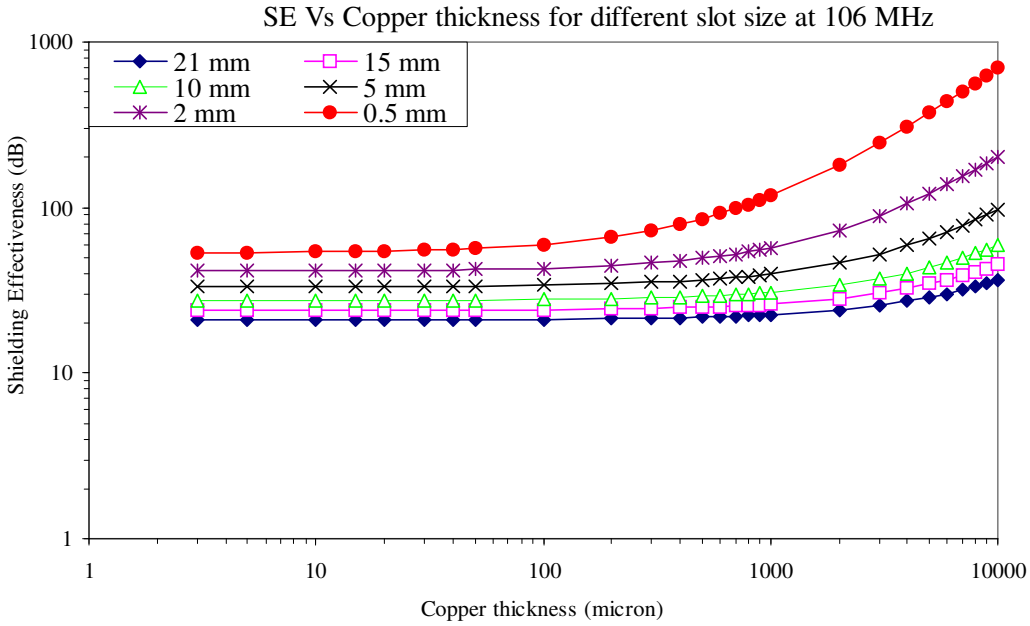

Fig. 6.10. Shielding effectiveness with 36 slots for various slot lengths at 106 MHz.

A decrease in the linear dimension as well as having minimum number of holes would help improve the SE.

6.1.5 The double-layer copper shield

The results obtained from the single-layer shield indicate that the overall shielding around the PET detectors is not a Faraday cage, unlike the aluminum shield. The shielding must be RF tight and any breaks in the shield (even less than 1/50 of wavelength) must be closed. A continuous metal barrier acts as a good RF shield around the PET detector. However, the main goal is to limit the effect of RF on the PET data as well as obtaining good quality MR images. The introduction of segments in the shield is justified to minimize the possible effect of eddy currents. It has also been observed that these segments are contributing to the overall decrease in the shielding effectiveness. One of the solutions to this problem is to decrease the linear dimensions of the segments and/or decrease the number of segments. Therefore, the goal was to construct a shield that provides as good attenuation as the aluminum shield and allows us to obtain good quality MR images that are comparable when acquired with the no-shield condition (0 dB).

It has been mentioned in the literature that the shielding can be used as a waveguide [110, 119, 138, 145]. An example of a honeycomb structure is a good example. Using a double-sided copper provides a good shield barrier whose performance can be comparable to a continuous shield. It must be noted that the shield around the RF coil is a double-sided copper film with the segments offset. A similar structure is desired on the remaining outer surfaces of the PET housing. Therefore, adding another segmented layer and offsetting the segments would make the shield more RF tight and minimize the effect of apertures. In addition, the thickness of the copper shield is doubled (36 µm). The two layers are interconnected forcing the RF fields to pass through an extended waveguide. They work as a good barrier, shielding the RF currents from passing through and minimizing the eddy currents compared to the aluminum shield. There have been some interesting articles on the advantages of using double-layer [143, 146] and multilayer shields [147-150], compared to single-layer shields. However, for RF shielding in PET/MRI applications, adding more layers can be redundant if there is no considerable increase in the shielding effectiveness and may degrade the MR image quality. In addition, two copper layers provide a shield depth of 36 skin depths at 400 MHz. The first step in improving the shielding effectiveness is to make the shield a near-perfect Faraday cage. As shown in Figure 6.11, the copper tabs are used to connect the layers on the remaining surfaces.

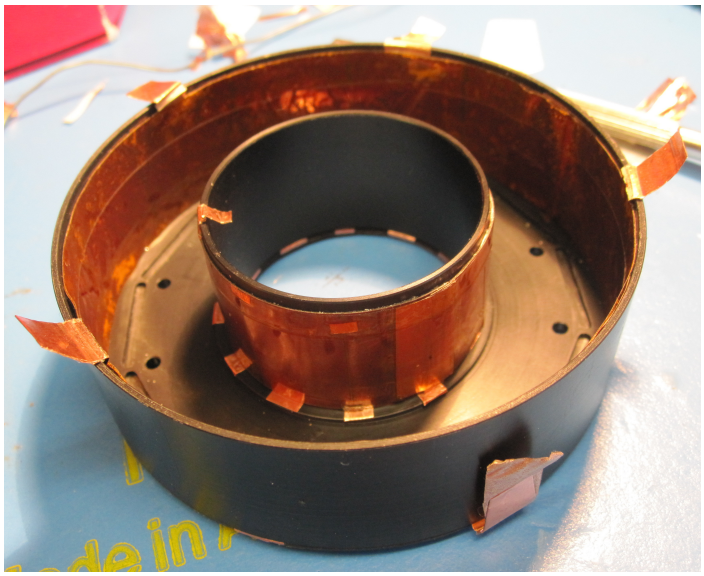

Fig. 6.11. Shield connections inside the PET housing using copper tabs.

Ideally, a 360^0 contact must be implemented to shield the possible seams, openings from where the RF can leak. Also, the shield contact between the joints must be solid and enough pressure must be exerted to improve the shield. Figure 6.12 shows the singles and coincidence count rates for different sequences as a function of shields with different thicknesses.

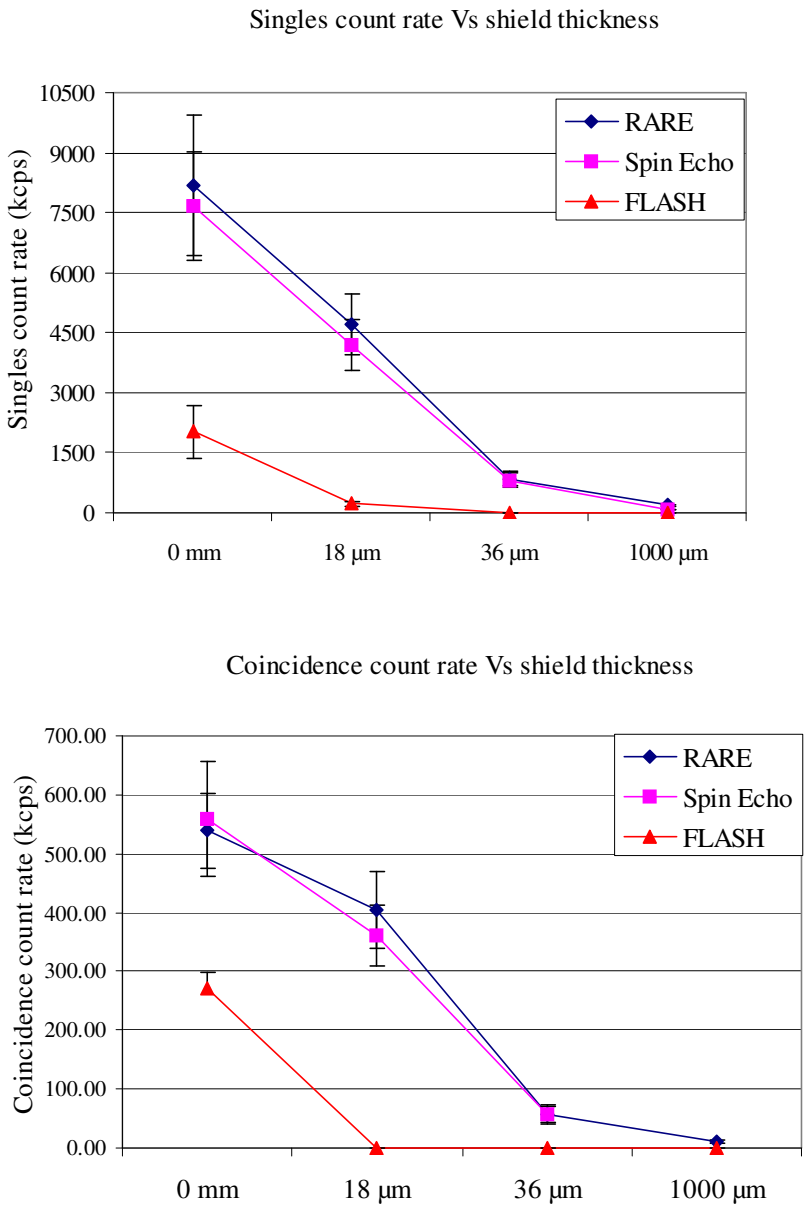

Fig. 6.12. Singles and coincidence count rates for different shield thickness.

The double-layer copper suppressed the effect of RF coupling compared to the single-layer shield. In addition, there are no knocked-out channels in PET that were left in an inoperable state during the RF pulsing for the unshielded PET condition. The 1 mm aluminum shield certainly

provided better shielding compared to the copper shields. The improvement in the performance is accounted for the closed structure of the aluminum rather than the thickness alone. With an increase in the frequency, we gain in the shielding due to the absorption loss. Yet, the interference is not eliminated. If the performance of the shield is not a concern, then the interference could lie elsewhere. An overall shield covering the entire length of the RF coil may minimize of the RF coupling.

6.2 RF power

The magnitude of the RF spikes was observed to be dependent on the applied RF power levels. From the interference results, it is apparent that the spurious counts were highest for 180^0 refocusing pulses in the spin echo and RARE sequences and were lowest for 20^0 flip angle in the FLASH gradient echo sequences. From the results presented in Chapter 5 for double-layer copper and aluminum shields respectively, there was no interference from the FLASH gradient echo sequences. The typical flip angles that were used during PET/MRI studies for FLASH sequences ranged between 10^0 to 20^0. The bandwidth of the RF pulse is around 5 kHz per slice. Therefore, a narrower RF pulse is obtained after applying the Fourier transform. The RF pulse duration for FLASH sequences was 1 ms.

On the other hand, the RF power levels were higher for 90^0 and 180^0 pulses in the spin echo sequences. The slice-select bandwidth for 90^0 pulse is around 3 kHz per slice, while the bandwidth for refocusing pulse is between 2-3 kHz per slice. The RF pulse duration for 90^0 pulse is between 1-2 ms and for the 180^0 it is 2-4 ms. Hence, the duty cycle of the RARE sequences is higher and is proportional to the dead time in the PET data after discarding the spurious counts as a result of interference. From the interference patterns observed in the PET data for different sequences, there seems to be a threshold above which the RF leaks into the shield with the increase in the power levels. The absolute power that is injected into the imaging sample provides some clues in identifying the power levels at which the PET electronics become susceptible to RF pulsing. To measure the actual power, a pulsed RF power calculation was done.

The PET detector was set up the same way as for routine PET/MRI studies. The RF coil connected to the 90^0 hybrid coupler was loaded with a cylindrical sample and was adjusted for tuning and matching. The RF pulse gain adjustments were performed to optimize for the

corresponding imaging sequence. The RF transmitter that had a 3 dB attenuator was disconnected from the coupler and connected to one end of a BNC coaxial cable. The other end of the cable was connected to a 100 dB attenuator. The attenuator was in turn connected to the oscilloscope that was set at 50 Ω input impedance. The goal was to adjust the attenuation levels on the attenuator, until the RF spikes were visible on the scope. The attenuation level was reduced from 100 dB to 40 dB. The RF was pulsed for different flip angles for FLASH sequences and 90^0 and 180^0 flip angles for the spin echo and RARE sequences, respectively. The peak-to-peak voltage was measured on the scope for all the pulse acquisitions. All the RF pulses were sinc pulses. The root mean square (RMS) voltage was calculated as

$$V_{rms} = \frac{V_{pk-pk}}{2 * \sqrt{2}}$$

Using the power formula, $P = \frac{V^2_{rms}}{R}$, the power in watts was calculated. Here R = 50 Ω. Since the total attenuation is 43 dB (40 dB on attenuator + 3 dB on RF transmitter), the absolute power is now calculated using the formula

$$43dB = 10\log\left(\frac{P_1}{P_0}\right)$$; rearranging the formula, $P_1 = P_0 * 10^{(4.3)}$

where P_1 is absolute power in watts.

Table 6.1 shows the absolute power for different flip angles.

Table 6.1. RF Power measurements using scope for different sequences

Flip Angle	Pk-Pk (mV)	V_{rms} (mV) = V_{peak}/1.41	Power = V^2_{rms}/R(watts)	Absolute RF Power (watts)	dB_m
FLASH					
15.00	55.80	19.73	0.000008	0.16	21.91
30.00	111.00	39.24	0.000031	0.61	27.89
45.00	176.00	62.23	0.000077	1.55	31.89
60.00	226.00	79.90	0.000128	2.55	34.06
75.00	280.00	98.99	0.000196	3.91	35.92
90.00	339.00	119.85	0.000287	5.73	37.58
Spin Echo					
90.00	140.00	49.50	0.000049	0.98	29.90
180.00	217.00	76.72	0.000118	2.35	33.71
RARE					
90.00	180.00	63.64	0.000081	1.62	32.08
180.00	380.00	134.35	0.000361	7.20	38.58
180.00	380.00	134.35	0.000361	7.20	38.58
180.00	380.00	134.35	0.000361	7.20	38.58
180.00	380.00	134.35	0.000361	7.20	38.58
180.00	380.00	134.35	0.000361	7.20	38.58
180.00	380.00	134.35	0.000361	7.20	38.58
180.00	380.00	134.35	0.000361	7.20	38.58
180.00	380.00	134.35	0.000361	7.20	38.58

Figure 6.13 shows the RF power plots for FLASH and RARE sequences. For each imaging sequence, the pulses are optimized accordingly. Therefore the 90^0 pulse for FLASH, Spin Echo and RARE sequences would be different. From the above table it is clear that the amount of RF power delivered to the imaging sample may have a huge impact on the PET electronics residing close to the coil, especially with RARE sequences. In addition, if the rise/fall times of the RF pulses are fast then even small apertures can act as effective antennas. The pulsed RF source has higher frequency component compared to a continuous wave. Most of the common EMI problems are addressed for continuous broadband RF wave. Therefore, having the RF coil (source) very close to the PET circuitry (receiver) will enhance RF coupling.

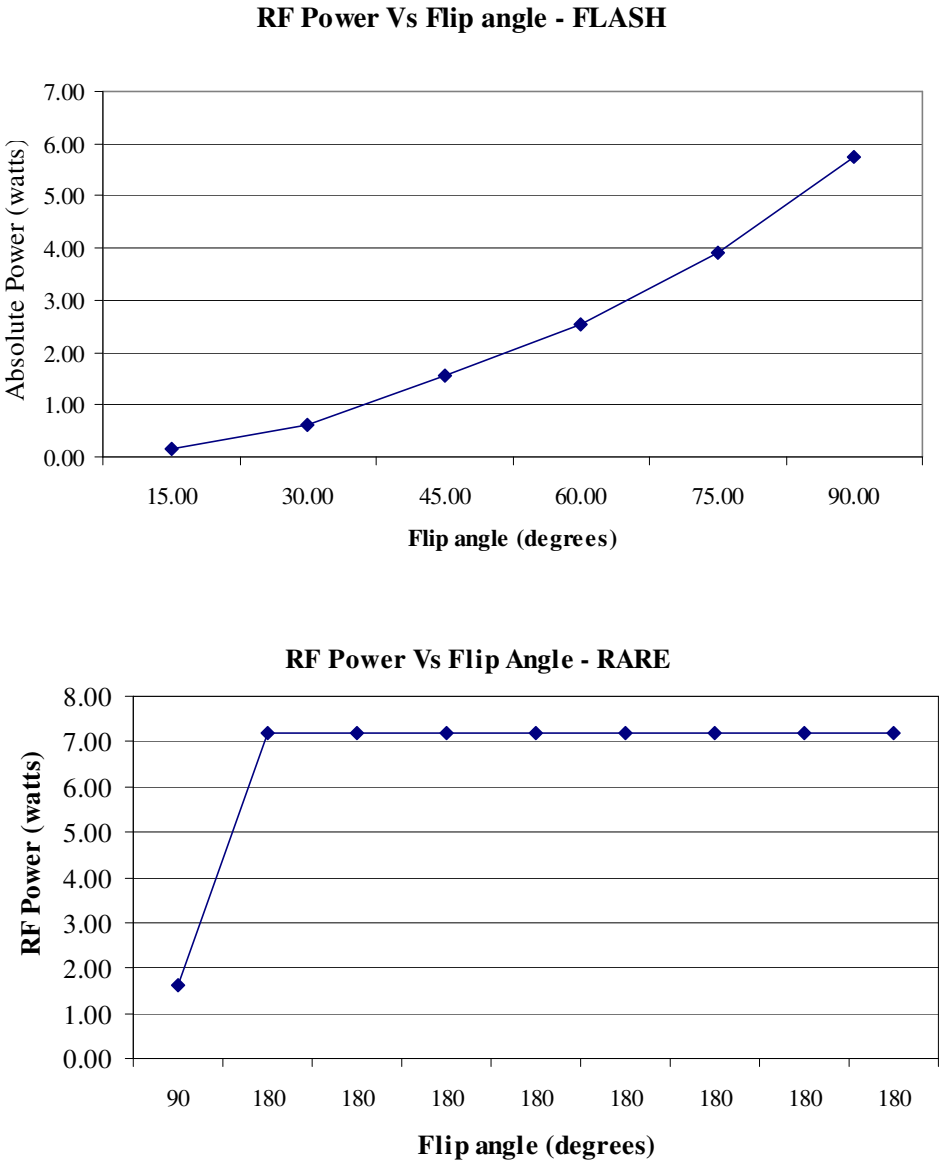

Fig. 6.13. Absolute RF power that is excited near the sample for FLASH and RARE sequences.

Another measure of analysis is the pattern of prompts count rate as a function of energy threshold. For this measurement, the energy threshold has been varied between 350 keV to 650 keV during the RF pulsing and the PET data was acquired. Figure 6.14 shows the plot for different threshold samples for a single-layer copper. The energy threshold can be set to reject a considerable number of spurious counts during RF pulsing. From the energy spectrum plot during MR ON condition for a single channel, it appears that most of the spurious counts fall in the ULD region.

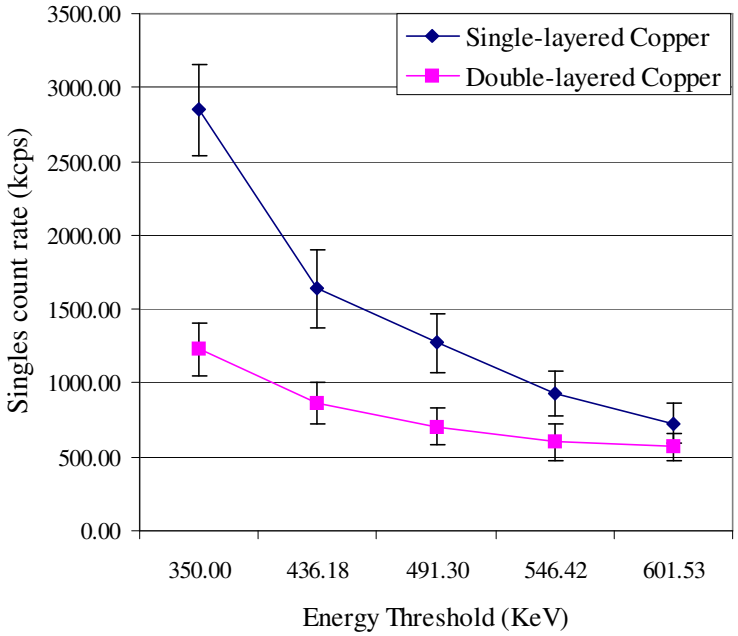

Fig. 6.14. Count rate pattern for different energy thresholds in a single-layer copper shield.

The flip angle θ of an RF pulse can be calculated as

$$\theta = \gamma B_1 t$$

B_1 = amplitude of the applied magnetic field.

t = RF pulse duration (ms)

From the above formula, the B_1 field amplitude can be calculated at a given flip angle and RF pulse duration. Typically, RF pulse duration varies between 1-2 mm for 90^0 pulse and 2-4 ms for 180^0 pulse in a RARE sequence. For FLASH gradient echo sequences, it is between 1-2 ms. Figure 6.15 shows the B_1 field amplitude as a function of pulse duration for different flip angles.

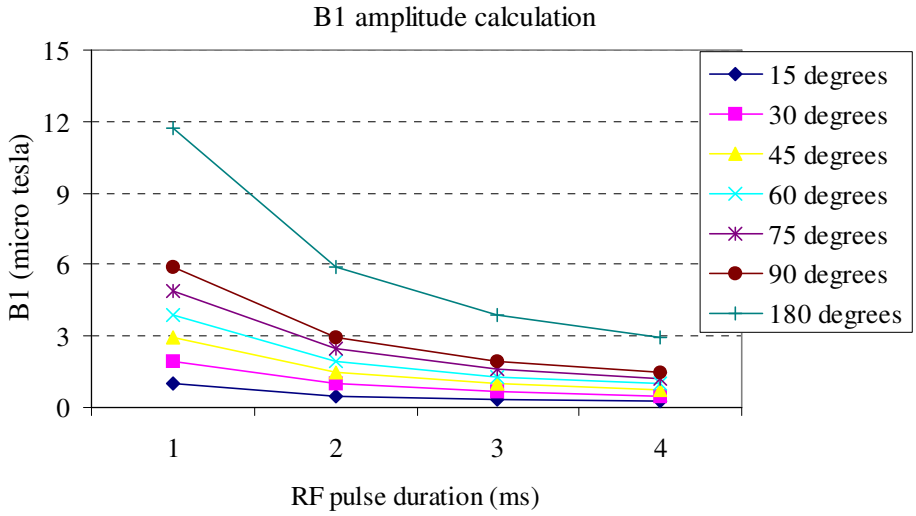

Fig. 6.15. B_1 field amplitude as a function of RF pulse duration.

It must be noted that the magnitude of B_1 field is not the only concern in attenuating the spurious counts in the PET data. To be precise, the dead space in the PET data as a result of removing the spurious spikes is because of the duration of the RF pulse in that period. A higher magnitude RF pulse (high B_1 field) contributes more towards writing unwanted data to the disk and possibly knocking some of the susceptible PET channels. For PET data acquisition perspective, it is necessary to minimize the duty factor of the RARE MR sequences, although the B_1 amplitude is not at its peak. The valuable PET data is lost mainly due to the duty factor of the RF pulses. It also depends on the number of slices acquired in an MR sequence. Figure 6.16 shows the duty factor of MR RARE sequence as a function of number of slices acquired, for a repetition time TR of 2500 ms. The TR = 2500 ms represents the time over all the slices in a sequences. Therefore, the TR per slice for a 29-slice sequence is 86.2 ms. It is 108 ms, 131 ms and 166 ms for 23-, 19- and 15-slice MR acquisitions, respectively.

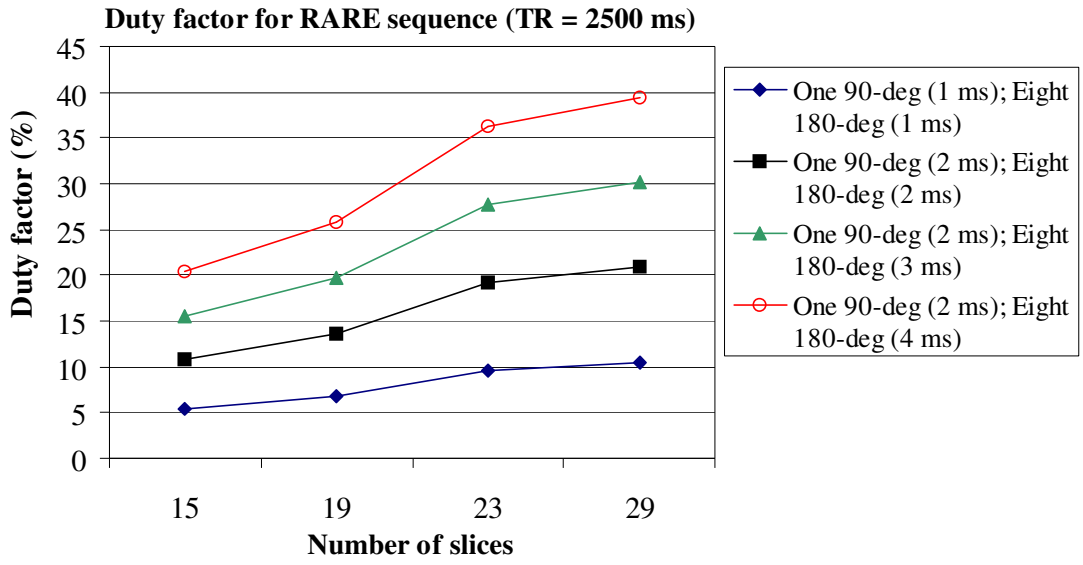

Fig. 6.16. Duty factor as a function of number of slices for different pulse duration in a RARE sequence.

From the above plots, it can be concluded that the MR pulse sequences can be optimized during PET/MRI studies in addition to shielding, for better performance of either system. Although perfect shielding will eliminate the undesirable effects due to the RF pulses, new MRI scanning protocols can be implemented based on the above observations.

6.3 Limitations

Integrating a PET detector inside a 9.4 T MRI yielded good quality PET/MRI data that demonstrate the feasibility of performing simultaneous PET/MRI studies in live animals. The studies have few limitations.

- Although effort was made to minimize the RF coupling on the PET data, the effect was not eliminated completely in spite of creating a solid shield around the PET electronics. The loss of counts in the PET data corresponds to the RF pulse duration and the duty cycle of the spin echo imaging sequences, despite the use of copper shield. In addition, the use of LLD and ULD energy windows would have minimized the effect of the spurious counts on the PET data to some extent. The ULD energy threshold is non-functional for the current version of the PET detector. Nevertheless, the pattern of PET

counts that were blocked during RF pulsing has been eliminated with the double-layer copper shield.

- Another caveat in the studies is the degree of the inhomogeneities in the MR images. Given the coil volume, it is challenging to obtain a high degree of uniformity in the MR images. The degradation in SNR and uniformity in the MR images were observed with the copper shield, compared to the unshielded condition. The acquisition of the MR phantom data was not performed using the same RF coil. Instead, another RF coil with the same circuitry but different values of capacitors was used to acquire the MR images without the PET condition. This suggests that the behavior of the RF coil does not remain the same with the changes made to the RF shielding. The main challenge was to perform impedance matching on the coil for any changes made to the overall shielding around it. The RF coil coupling is sensitive to even slight displacement (~1 mm) with respect to the position of the PET detector suggesting that the proximity of the shield near the coil components becomes critical. An excellent source of information about the performance of the small animal RF coils can be found in the reference [88]. The author acknowledges that as the volume of the RF coils decrease, the uniformity of the coil conductors in the imaging volume is compromised.
- The theoretical evaluation of the shielding effectiveness (SE) described in section 6.1.2 using different shields for aperture control is based on far-field conditions. The SE calculations for RF antenna in near-field conditions require complex computations and require defining the boundary conditions [151]. In addition, a multiphysics electromagnetic model is required to deduce an accurate evaluation of SE as it is difficult to predict the outcome, unlike far-field conditions. This is because the electric and magnetic fields must be considered separately for near-field conditions.
- Finally, no temperature measurements were performed during the PET/MRI studies as it was not practically feasible to lay long temperature sensors that enter the PET detector shield. Although, the 1:1 coupling between the scintillator and the APDs ensures no ambiguity in detecting the events, there could be a potential shift in the photopeaks. However, the shifts will be the same for the events. To maintain a Faraday cage around the PET detector, any openings are covered which may increase the temperature inside the PET detector where the APDs reside.

CHAPTER 7: FUTURE RECOMMENDATIONS AND CONCLUSIONS

7.1 Future recommendations

The analysis on shielding presented in this thesis would provide an insight into the magnitude of electromagnetic interactions at very high frequencies. The following sub-sections discuss about the possible improvements in the current and future PET designs based on the experience gained with the current setup.

7.1.1. The RF coil

The design and construction of the two pairs of cross coils for PET/MRI studies was unique and built around the geometry of the PET detector. The coil is robust and generates RF fields around the active region of the coil. From the PET electronics view point, the coil is the main source of interference causing the PET circuitry to become the default victim. There has been a lot of effort and work devoted to shield the victim, but shielding the source might yield better results. The most common practice to investigate the RF coupling in EMC applications is to shield the source that is radiating RF fields. It must be reiterated that the interference was reduced in double-layer shielding because the second copper layer was introduced only at the endplates of the housing. The outer rim of the inner sleeve already had a double-layer shield. This implies that there were stray RF fields that were emanating from other regions of the coil, besides the active region of the imaging volume.

In future, it would be advantageous to encapsulate the entire length of the RF coil with a copper shield. This is an important first step in ensure that the RF fields do not propagate over long distances or create undesired RF currents on the neighboring circuits. For most of the MRI coil technology, the emphasis is usually given to shielding the RF coil because the RF fields may interact with the gradient fields compromising the overall coil performance. Most of the commercially available RF coils have a built-in shield around it. The shielding around the entire length of the coil confines the parasitic fields within the shield and provides efficient power transfer to the imaging sample.

None in the publications performing simultaneous PET/MR imaging studies reported the effect of RF on their PET imagers, although the effect due to the gradients was reported [49]. This is because most of the research groups employ standard and much larger shielded RF coils

that are commercially available and in compliance with the MRI scanners. For example, the PET/MRI groups from the Sungkyunkwan University, Korea, University of Tuebingen, Germany and University of California – Davis, employ 35 mm diameter standard Bruker RF birdcage coil for their small animal imaging studies in a Bruker 7 T MRI scanners [49, 50, 53]. Simultaneous PET/MR imaging of a rat brain performed by Raylman *et al.,* was done using a simple receive only coil with a saddle structure [33]. A standard RF transmit coil was used in 3 T MRI scanner.

Another important factor is the proximity of the coil to the PET electronics in our studies. The standard Bruker coils have 35 mm inner diameter (ID) and 60 mm outer diameter (OD). Our custom built transceiver coil has (ID/OD) 32 mm/37mm. The distance from the inner rim of the RF coil to the front face of the PET scintillation detector is as close as 7 mm in our studies while it is about 15 mm for the other groups [49, 50, 53]. Therefore, for future design of PET systems, analysis on the effect of coil on the digital circuits can be performed at the design stage of the PET systems. Since we are limited by the geometry of the PET scanner, further analysis on shielding and RF coil design can be explored by performing EMI/RF simulations.

7.1.2 EMI/RF simulations

There are some good simulation packages that are available for the design of RF coils for specific applications. The strength of these simulation packages can be exploited for further studying the EMI patterns when combining PET with MRI. The simulation tools would help in understanding how the RF currents flow on the shield surface and how the shield affects the coil resonance and overall performance. Some of the commercially available simulation packages include:

- SemCADX
- COMSOL Multiphysics
- CST Microwave Studios
- Vector fields

7.1.3. Common-mode and sniffer probes

Since the imbalances in the ground topology and ground loops were a concern for this study, common-mode probes can help measure the conducted emissions on the cables [152]. Many EMC compliance handbooks recommend measuring the common-mode currents on all the cables connected to the test equipment, which would save a lot of speculation and time in solving interference problems. The sniffer probes, on the other hand, helps in measuring magnetic coupling on the PCBs. Careful test setup is required for these tests. In house sniffer probes can be constructed for this application.

7.1.4. Board level shielding

Shielding some of the digital electronics on the PCB will help suppress some of the radiated emissions. Board level shielding can be implemented on the circuits where there is high level of digital activity. They confine the radiation from coupling with other circuits in close vicinity. The new versions of the TSPM board and PCI cards can have board level shielding, some of which are made of plastic.

7.1.5. Carbon fiber nanotubes – New EMI shield material

There have been recent studies on the use of carbon nanofiber composites and conducting polymers [150] as the shield materials. If the use of metallic shielding is a problem, new EMI shielding materials can be explored. Although some report the effects of temperature at high frequencies, there has been a lot of promise to use some of the fabric material.

7.2. Conclusions

In conclusion, the electromagnetic interactions between the PET and MRI systems were described, identified and evaluated. Some of the sources of EMI were identified and steps were taken to isolate the RF fields interfering with the PET system.

- The custom-built RF coil was tested for its optimal performance on the work bench. The two pairs of Helmholtz coil was carefully tuned and matched for different load variations in the imaging volume using a calibrated spectrum/network analyzer with an RF impedance adapter connected to the instrument. The impedance matching was performed

to obtain lower reflection coefficient for efficient power transfer during the MRI acquisitions. With the introduction of the different shields around the coil, a change in the resonance frequency and the overall performance of the coil was observed. The coil was retuned by changing the capacitance values on the coil circuitry to improve the coil performance in the presence of different shields.

- The grounding configuration of the PET system was modified to minimize the ground loops. This was achieved by terminating the grounds between the signal return and chassis ground at multiple points. As a result, the ground potential between the signal returns and the chassis was minimized. For all practical purposes, ground terminations within 1/20 of the wavelength are suggested to minimize the ground loops.
- The Faraday box shielding around the TSPM board eliminated the effect of PET interference on the RF clock. The RF coil was picking up the noise emanating from the multiple clock harmonics of the PET system. By shielding the cables and closing the TSPM shield box, RF coupling was eliminated.
- One of the main challenges encountered during the course of the work is to evaluate the shielding around the PET detectors that in close proximity of the RF coil. Different shield configurations (aluminum, single-layer segmented copper and double-layer segmented copper with offset) for PET housing were evaluated. The double-layer copper provides a reasonable tradeoff in obtaining good quality MR images and suppressing the interference due to the RF on PET.
- From the shielding theory and applications, the minimum aperture dimensions required to achieve good attenuation were estimated. At 400 MHz, the linear dimension of the apertures $< \lambda/50$ is desired.
- Shielding the RF coil can be considered in the future to significantly minimize the undesired effects due to RF coupling.
- Cooling the PET electronics with mesh openings can be employed in the current and future systems to optimally reduce RF penetration in these openings.

Bibliography

[1] C. von Forstner, J. H. Egberts, O. Ammerpohl, D. Niedzielska, R. Buchert, P. Mikecz, U. Schumacher, K. Peldschus, G. Adam, C. Pilarsky, R. Grutzmann, H. Kalthoff, E. Henze, and W. Brenner, "Gene expression patterns and tumor uptake of 18F-FDG, 18F-FLT, and 18F-FEC in PET/MRI of an orthotopic mouse xenotransplantation model of pancreatic cancer," *J Nucl Med,* vol. 49, pp. 1362-70, Aug 2008.

[2] R. L. Wahl, L. E. Quint, R. D. Cieslak, A. M. Aisen, R. A. Koeppe, and C. R. Meyer, ""Anatometabolic" tumor imaging: fusion of FDG PET with CT or MRI to localize foci of increased activity," *J Nucl Med,* vol. 34, pp. 1190-7, Jul 1993.

[3] P. B. Garlick, P. K. Marsden, A. C. Cave, H. G. Parkes, R. Slates, Y. Shao, R. W. Silverman, and S. R. Cherry, "PET and NMR dual acquisition (PANDA): applications to isolated, perfused rat hearts," *NMR Biomed,* vol. 10, pp. 138-42, May 1997.

[4] S. Azman, J. Gjaerum, D. Meier, L. T. Muftuler, G. Maehlum, O. Nalcioglu, B. E. Patt, B. Sundal, M. Szawlowski, B. M. W. Tsui, D. J. Wagenaar, and W. Yuchuang, "A nuclear radiation detector system with integrated readout for SPECT/MR small animal imaging," in *IEEE Nucl Sci Symp Conf Rec*, 2007, pp. 2311-2317.

[5] D. Meier, D. J. Wagenaar, S. Chen, J. Xu, J. Yu, and B. M. W. Tsui, "A SPECT camera for combined MRI and SPECT for small animals," *Nuclear Instruments and Methods in Physics Research Section A: Accelerators, Spectrometers, Detectors and Associated Equipment,* vol. In Press, Corrected Proof, 2010.

[6] T. Beyer, D. W. Townsend, T. Brun, P. E. Kinahan, M. Charron, R. Roddy, J. Jerin, J. Young, L. Byars, and R. Nutt, "A combined PET/CT scanner for clinical oncology," *J Nucl Med,* vol. 41, pp. 1369-79, Aug 2000.

[7] O. Mawlawi, T. Pan, and H. A. Macapinlac, "PET/CT imaging techniques, considerations, and artifacts," *J Thorac Imaging,* vol. 21, pp. 99-110, 2006.

[8] W. Sureshbabu and O. Mawlawi, "PET/CT imaging artifacts," *J Nucl Med Technol,* vol. 33, pp. 156-61, 2005.

[9] A. Bockisch, T. Beyer, G. Antoch, L. S. Freudenberg, H. Kuhl, J. F. Debatin, and S. P. Muller, "Positron emission tomography/computed tomography-imaging protocols, artifacts, and pitfalls," *Mol Imaging Biol,* vol. 6, pp. 188-99, 2004.

[10] R. Weissleder, "Scaling down imaging: molecular mapping of cancer in mice," *Nat Rev Cancer,* vol. 2, pp. 11-8, 2002.

[11] J. Werner, J. Schmidt, A. L. Warshaw, M. M. Gebhard, C. Herfarth, and E. Klar, "The relative safety of MRI contrast agent in acute necrotizing pancreatitis," *Ann Surg,* vol. 227, pp. 105-11, 1998.

[12] B. Huang, M. W. Law, and P. L. Khong, "Whole-body PET/CT scanning: estimation of radiation dose and cancer risk," *Radiology,* vol. 251, pp. 166-74, 2009.

[13] I. Tkac, P. G. Henry, P. Andersen, C. D. Keene, W. C. Low, and R. Gruetter, "Highly resolved in vivo 1H NMR spectroscopy of the mouse brain at 9.4 T," *Magn Reson Med,* vol. 52, pp. 478-84, 2004.

[14] P. S. Chandra, N. Salamon, J. Huang, J. Y. Wu, S. Koh, H. V. Vinters, and G. W. Mathern, "FDG-PET/MRI coregistration and diffusion-tensor imaging distinguish epileptogenic tubers and cortex in patients with tuberous sclerosis complex: a preliminary report," *Epilepsia,* vol. 47, pp. 1543-9, 2006.

[15] N. Salamon, J. Kung, S. J. Shaw, J. Koo, S. Koh, J. Y. Wu, J. T. Lerner, R. Sankar, W. D. Shields, J. Engel, Jr., I. Fried, H. Miyata, W. H. Yong, H. V. Vinters, and G. W. Mathern, "FDG-PET/MRI coregistration improves detection of cortical dysplasia in patients with epilepsy," *Neurology,* vol. 71, pp. 1594-601, 2008.

[16] K. Meguro, C. LeMestric, B. Landeau, B. Desgranges, F. Eustache, and J. C. Baron, "Relations between hypometabolism in the posterior association neocortex and hippocampal atrophy in Alzheimer's disease: a PET/MRI correlative study," *J Neurol Neurosurg Psychiatry,* vol. 71, pp. 315-21, Sep 2001.

[17] A. Malesci, L. Balzarini, A. Chiti, and G. Lucignani, "Pancreatic cancer or chronic pancreatitis? An answer from PET/MRI image fusion," *Eur J Nucl Med Mol Imaging,* vol. 31, p. 1352, Sep 2004.

[18] J. Ruf, E. Lopez Hanninen, M. Bohmig, I. Koch, T. Denecke, M. Plotkin, J. Langrehr, B. Wiedenmann, R. Felix, and H. Amthauer, "Impact of FDG-PET/MRI image fusion on the detection of pancreatic cancer," *Pancreatology,* vol. 6, pp. 512-9, 2006.

[19] C. J. Ledezma, W. Chen, V. Sai, B. Freitas, T. Cloughesy, J. Czernin, and W. Pope, "18F-FDOPA PET/MRI fusion in patients with primary/recurrent gliomas: initial experience," *Eur J Radiol,* vol. 71, pp. 242-8, Aug 2009.

[20] G. El-Haddad, R. Kumar, R. Pamplona, and A. Alavi, "PET/MRI depicts the exact location of meniscal tear associated with synovitis," *Eur J Nucl Med Mol Imaging,* vol. 33, pp. 507-8, Apr 2006.

[21] T. Maeda, U. Tateishi, Y. Sasajima, T. Hasegawa, H. Daisaki, Y. Arai, and K. Sugimura, "Atypical polypoid adenomyoma of the uterus: appearance on (18)F-FDG PET/MRI fused images," *AJR Am J Roentgenol,* vol. 186, pp. 320-3, Feb 2006.

[22] R. Benedetto, M. P. Carneiro, F. A. Junqueira, A. Coutinho, Jr., A. von Ristow, and L. M. Fonseca, "(18)F-FDG in distinction of atherosclerotic plaque: Innovation in PET/MRI technology," *Arq Bras Cardiol,* vol. 93, pp. e84-7, e97-100, Dec 2009.

[23] M. D. Seemann, "Whole-body PET/MRI: the future in oncological imaging," *Technol Cancer Res Treat,* vol. 4, pp. 577-82, Oct 2005.

[24] J. Gaa, E. J. Rummeny, and M. D. Seemann, "Whole-body imaging with PET/MRI," *Eur J Med Res,* vol. 9, pp. 309-12, Jun 30 2004.

[25] G. Antoch and A. Bockisch, "Combined PET/MRI: a new dimension in whole-body oncology imaging?," *Eur J Nucl Med Mol Imaging,* vol. 36 Suppl 1, pp. S113-20, Mar 2009.

[26] G. Lucignani, "Time-of-flight PET and PET/MRI: recurrent dreams or actual realities?," *Eur J Nucl Med Mol Imaging,* vol. 33, pp. 969-71, Aug 2006.

[27] A. Boss, S. Bisdas, A. Kolb, M. Hofmann, U. Ernemann, C. D. Claussen, C. Pfannenberg, B. J. Pichler, M. Reimold, and L. Stegger, "Hybrid PET/MRI of Intracranial Masses: Initial Experiences and Comparison to PET/CT," *J Nucl Med,* vol. 51, pp. 1198-205, Aug 2010.

[28] Z. H. Cho, Y. D. Son, H. K. Kim, S. T. Kim, S. Y. Lee, J. G. Chi, C. W. Park, and Y. B. Kim, "Substructural hippocampal glucose metabolism observed on PET/MRI," *J Nucl Med,* vol. 51, pp. 1545-8, Oct 2010.

[29] H. P. Schlemmer, B. J. Pichler, R. Krieg, and W. D. Heiss, "An integrated MR/PET system: prospective applications," *Abdom Imaging,* vol. 34, pp. 668-74, Nov 2009.

[30] A. Fatemi-Ardekani, N. Samavati, J. Tang, and M. V. Kamath, "Advances in multimodality imaging through a hybrid PET/MRI system [abstract]," *Crit Rev Biomed Eng,* vol. 37, pp. 495-515, 2009.

[31] S. K. Kim, H. J. Choi, S. Y. Park, H. Y. Lee, S. S. Seo, C. W. Yoo, D. C. Jung, S. Kang, and K. S. Cho, "Additional value of MR/PET fusion compared with PET/CT in the detection of lymph node metastases in cervical cancer patients," *Eur J Cancer,* vol. 45, pp. 2103-9, Aug 2009.

[32] H. B. Christensen NL, Heil BG, Fetterly K., "Positron emission tomography within a magnetic field using photomultiplier tubes and lightguides," *Physics in Medicine and Biology,* vol. 40, pp. 691-697, 1995.

[33] R. R. Raylman, S. Majewski, S. K. Lemieux, S. S. Velan, B. Kross, V. Popov, M. F. Smith, A. G. Weisenberger, C. Zorn, and G. D. Marano, "Simultaneous MRI and PET imaging of a rat brain," *Phys Med Biol,* vol. 51, pp. 6371-9, 2006.

[34] Y. Shao, S. R. Cherry, K. Farahani, K. Meadors, S. Siegel, R. W. Silverman, and P. K. Marsden, "Simultaneous PET and MR imaging," *Phys Med Biol,* vol. 42, pp. 1965-70, Oct 1997.

[35] R. B. Slates, K. Farahani, Y. Shao, P. K. Marsden, J. Taylor, P. E. Summers, S. Williams, J. Beech, and S. R. Cherry, "A study of artefacts in simultaneous PET and MR imaging using a prototype MR compatible PET scanner," *Phys Med Biol,* vol. 44, pp. 2015-27, 1999.

[36] J. E. Mackewn, D. Strul, W. A. Hallett, P. Halsted, R. A. Page, S. F. Keevil, S. C. R. Williams, S. R. Cherry, and P. K. Marsden, "Design and development of an MR-compatible PET scanner for imaging small animals," *IEEE Trans Nucl Sci.,* vol. 52, pp. 1376-1380, 2005.

[37] M. Imaizumi, S. Yamamoto, M. Kawakami, M. Aoki, E. Sugiyama, Y. Kanai, E. Shimosegawa, and J. Hatazawa, "Simultaneous imaging of magnetic resonance imaging and positron emission tomography by means of MRI-compatible optic fiber-based PET: a validation study in ex vivo rat brain," *Jpn J Radiol,* vol. 27, pp. 252-6, 2009.

[38] S. Yamamoto, M. Imaizumi, Y. Kanai, M. Tatsumi, M. Aoki, E. Sugiyama, M. Kawakami, E. Shimosegawa, and J. Hatazawa, "Design and performance from an integrated PET/MRI system for small animals," *Ann Nucl Med,* 2010.

[39] J. E. Mackewn, D. Strul, W. A. Hallett, P. Halsted, R. A. Page, S. F. Keevil, S. C. R. Williams, S. R. Cherry, and P. K. Marsden, "Design and development of an MR-

compatible PET scanner for imaging small animals," *Nuclear Science, IEEE Transactions on,* vol. 52, pp. 1376-1380, 2005.

[40] P. K. Marsden, D. Strul, S. F. Keevil, S. C. Williams, and D. Cash, "Simultaneous PET and NMR," *Br J Radiol,* vol. 75 Spec No, pp. S53-9, Nov 2002.

[41] S. Takamatsu, S. Yamamoto, H. Murayama, and K. Minato, "Design and construction of a multi-slice, depth-of-interaction MR-compatible PET," in *Nuclear Science Symposium Conference Record, 2004 IEEE*, 2004, pp. 3810-3813 Vol. 6.

[42] A. J. Lucas, R. C. Hawkes, R. E. Ansorge, G. B. Williams, R. E. Nutt, J. C. Clark, T. D. Fryer, and T. A. Carpenter, "Development of a combined microPET-MR system [abstract]," *Technol Cancer Res Treat,* vol. 5, pp. 337-41, 2006.

[43] M. Poole, R. Bowtell, D. Green, S. Pittard, A. Lucas, R. Hawkes, and A. Carpenter, "Split gradient coils for simultaneous PET-MRI," *Magn Reson Med,* vol. 62, pp. 1106-11, 2009.

[44] K. M. Gilbert, W. B. Handler, T. J. Scholl, J. W. Odegaard, and B. A. Chronik, "Design of field-cycled magnetic resonance systems for small animal imaging," *Phys Med Biol,* vol. 51, pp. 2825-41, Jun 7 2006.

[45] B. J. Pichler, M. S. Judenhofer, C. Catana, J. H. Walton, M. Kneilling, R. E. Nutt, S. B. Siegel, C. D. Claussen, and S. R. Cherry, "Performance test of an LSO-APD detector in a 7-T MRI scanner for simultaneous PET/MRI," *J Nucl Med,* vol. 47, pp. 639-47, 2006.

[46] R. Grazioso, N. Zhang, J. Corbeil, M. Schmand, R. Ladebeck, M. Vester, G. Schnur, W. Renz, and H. Fischer, "APD-based PET detector for simultaneous PET/MR imaging," *Nuclear Instruments and Methods in Physics Research Section A: Accelerators, Spectrometers, Detectors and Associated Equipment,* vol. 569, pp. 301-305, 2006.

[47] M. S. Judenhofer, H. F. Wehrl, D. F. Newport, C. Catana, S. B. Siegel, M. Becker, A. Thielscher, M. Kneilling, M. P. Lichy, M. Eichner, K. Klingel, G. Reischl, S. Widmaier, M. Rocken, R. E. Nutt, H. J. Machulla, K. Uludag, S. R. Cherry, C. D. Claussen, and B. J. Pichler, "Simultaneous PET-MRI: a new approach for functional and morphological imaging," *Nat Med,* vol. 14, pp. 459-65, Apr 2008.

[48] C. Catana, Y. Wu, M. S. Judenhofer, J. Qi, B. J. Pichler, and S. R. Cherry, "Simultaneous acquisition of multislice PET and MR images: initial results with a MR-compatible PET scanner," *J Nucl Med,* vol. 47, pp. 1968-76, Dec 2006.

[49] C. Catana, D. Procissi, Y. Wu, M. S. Judenhofer, J. Qi, B. J. Pichler, R. E. Jacobs, and S. R. Cherry, "Simultaneous in vivo positron emission tomography and magnetic resonance imaging," *Proc Natl Acad Sci U S A,* vol. 105, pp. 3705-10, Mar 11 2008.

[50] M. S. Judenhofer, C. Catana, B. K. Swann, S. B. Siegel, W. I. Jung, R. E. Nutt, S. R. Cherry, C. D. Claussen, and B. J. Pichler, "PET/MR images acquired with a compact MR-compatible PET detector in a 7-T magnet," *Radiology,* vol. 244, pp. 807-14, 2007.

[51] K. Buscher, M. S. Judenhofer, M. T. Kuhlmann, S. Hermann, H. F. Wehrl, K. P. Schafers, M. Schafers, B. J. Pichler, and L. Stegger, "Isochronous assessment of cardiac metabolism and function in mice using hybrid PET/MRI," *J Nucl Med,* vol. 51, pp. 1277-84, Aug 2010.

[52] K. Buscher, M. S. Judenhofer, M. T. Kuhlmann, S. Hermann, H. F. Wehrl, K. P. Schafers, M. Schafers, B. J. Pichler, and L. Stegger, "Isochronous Assessment of Cardiac Metabolism and Function in Mice Using Hybrid PET/MRI," *J Nucl Med,* vol. 51, pp. 1277-84, Aug.

[53] J. Kang, Y. Choi, K. J. Hong, J. H. Jung, W. Hu, Y. S. Huh, H. Lim, and B.-T. Kim, "A feasibility study of photosensor charge signal transmission to preamplifier using long cable for development of hybrid PET-MRI," *Medical Physics,* vol. 37, pp. 5655-5664, 2010.

[54] H. P. Schlemmer, B. J. Pichler, M. Schmand, Z. Burbar, C. Michel, R. Ladebeck, K. Jattke, D. Townsend, C. Nahmias, P. K. Jacob, W. D. Heiss, and C. D. Claussen, "Simultaneous MR/PET imaging of the human brain: feasibility study," *Radiology,* vol. 248, pp. 1028-35, Sep 2008.

[55] A. Boss, A. Kolb, M. Hofmann, S. Bisdas, T. Nagele, U. Ernemann, L. Stegger, C. Rossi, H. P. Schlemmer, C. Pfannenberg, M. Reimold, C. D. Claussen, B. J. Pichler, and U. Klose, "Diffusion tensor imaging in a human PET/MR hybrid system," *Invest Radiol,* vol. 45, pp. 270-4, 2010.

[56] D. R. Schaart, S. Seifert, R. Vinke, H. T. van Dam, P. Dendooven, H. Lohner, and F. J. Beekman, "LaBr(3):Ce and SiPMs for time-of-flight PET: achieving 100 ps coincidence resolving time," *Phys Med Biol,* vol. 55, pp. N179-89, Apr 7 2010.

[57] R. Vinke, H. Löhner, D. R. Schaart, H. T. van Dam, S. Seifert, F. J. Beekman, and P. Dendooven, "Optimizing the timing resolution of SiPM sensors for use in TOF-PET

detectors," *Nuclear Instruments and Methods in Physics Research Section A: Accelerators, Spectrometers, Detectors and Associated Equipment,* vol. 610, pp. 188-191, 2009.

[58] R. Hawkes, A. Lucas, J. Stevick, G. Llosa, S. Marcatili, C. Piemonte, A. Del Guerra, and T. A. Carpenter, "Silicon photomultiplier performance tests in magnetic resonance pulsed fields," in *IEEE Nucl Sci Symp Conf Rec*, 2007, pp. 3400-3403.

[59] D. P. McElroy, V. Saveliev, A. Reznik, and J. A. Rowlands, "Evaluation of silicon photomultipliers: A promising new detector for MR compatible PET," *Nuclear Instruments and Methods in Physics Research Section A: Accelerators, Spectrometers, Detectors and Associated Equipment,* vol. 571, pp. 106-109, 2007.

[60] H. Seong Jong, S. In Chan, M. Ito, K. Sun Il, L. Geon Song, S. Kwang-Souk, P. Kwang Suk, R. June Tak, and L. Jae Sung, "An Investigation Into the Use of Geiger-Mode Solid-State Photomultipliers for Simultaneous PET and MRI Acquisition," *Nuclear Science, IEEE Transactions on,* vol. 55, pp. 882-888, 2008.

[61] S. España, L. M. Fraile, J. L. Herraiz, J. M. Udías, M. Desco, and J. J. Vaquero, "Performance evaluation of SiPM photodetectors for PET imaging in the presence of magnetic fields," *Nuclear Instruments and Methods in Physics Research Section A: Accelerators, Spectrometers, Detectors and Associated Equipment,* vol. 613, pp. 308-316, 2010.

[62] G. Delso and S. Ziegler, "PET/MRI system design," *Eur J Nucl Med Mol Imaging,* vol. 36 Suppl 1, pp. S86-92, Mar 2009.

[63] B. J. Pichler, A. Kolb, T. Nagele, and H. P. Schlemmer, "PET/MRI: paving the way for the next generation of clinical multimodality imaging applications," *J Nucl Med,* vol. 51, pp. 333-6, Mar 2010.

[64] N. E. Bolus, R. George, J. Washington, and B. R. Newcomer, "PET/MRI: the blended-modality choice of the future?," *J Nucl Med Technol,* vol. 37, pp. 63-71; quiz 72-3, Jun 2009.

[65] R. J. Hicks and E. W. Lau, "PET/MRI: a different spin from under the rim," *Eur J Nucl Med Mol Imaging,* vol. 36 Suppl 1, pp. S10-4, Mar 2009.

[66] H. F. Wehrl, A. W. Sauter, M. S. Judenhofer, and B. J. Pichler, "Combined PET/MR imaging--technology and applications [abstract]," *Technol Cancer Res Treat,* vol. 9, pp. 5-20, Feb 2010.

[67] H. Herzog, U. Pietrzyk, N. J. Shah, and K. Ziemons, "The current state, challenges and perspectives of MR-PET," *Neuroimage,* vol. 49, pp. 2072-82, Feb 1 2010.

[68] G. Delso, A. Martinez-Moller, R. A. Bundschuh, S. G. Nekolla, and S. I. Ziegler, "The effect of limited MR field of view in MR/PET attenuation correction," *Med Phys,* vol. 37, pp. 2804-12, Jun 2010.

[69] M. Hofmann, F. Steinke, V. Scheel, G. Charpiat, J. Farquhar, P. Aschoff, M. Brady, B. Scholkopf, and B. J. Pichler, "MRI-based attenuation correction for PET/MRI: a novel approach combining pattern recognition and atlas registration," *J Nucl Med,* vol. 49, pp. 1875-83, Nov 2008.

[70] M. Hofmann, B. Pichler, B. Scholkopf, and T. Beyer, "Towards quantitative PET/MRI: a review of MR-based attenuation correction techniques," *Eur J Nucl Med Mol Imaging,* vol. 36 Suppl 1, pp. S93-104, Mar 2009.

[71] A. Martinez-Moller, M. Souvatzoglou, G. Delso, R. A. Bundschuh, C. Chefd'hotel, S. I. Ziegler, N. Navab, M. Schwaiger, and S. G. Nekolla, "Tissue classification as a potential approach for attenuation correction in whole-body PET/MRI: evaluation with PET/CT data," *J Nucl Med,* vol. 50, pp. 520-6, Apr 2009.

[72] V. Keereman, Y. Fierens, T. Broux, Y. De Deene, M. Lonneux, and S. Vandenberghe, "MRI-based attenuation correction for PET/MRI using ultrashort echo time sequences," *J Nucl Med,* vol. 51, pp. 812-8, May 2010.

[73] C. Catana, A. van der Kouwe, T. Benner, C. J. Michel, M. Hamm, M. Fenchel, B. Fischl, B. Rosen, M. Schmand, and A. G. Sorensen, "Toward implementing an MRI-based PET attenuation-correction method for neurologic studies on the MR-PET brain prototype," *J Nucl Med,* vol. 51, pp. 1431-8, Sep 2010.

[74] E. Schreibmann, J. A. Nye, D. M. Schuster, D. R. Martin, J. Votaw, and T. Fox, "MR-based attenuation correction for hybrid PET-MR brain imaging systems using deformable image registration," *Med Phys,* vol. 37, pp. 2101-9, May 2010.

[75] H. Y. Lee, Z. Li, K. Chen, A. R. Hsu, C. Xu, J. Xie, S. Sun, and X. Chen, "PET/MRI dual-modality tumor imaging using arginine-glycine-aspartic (RGD)-conjugated radiolabeled iron oxide nanoparticles," *J Nucl Med,* vol. 49, pp. 1371-9, Aug 2008.

[76] C. Glaus, R. Rossin, M. J. Welch, and G. Bao, "In vivo evaluation of (64)Cu-labeled magnetic nanoparticles as a dual-modality PET/MR imaging agent," *Bioconjug Chem,* vol. 21, pp. 715-22, Apr 21 2010.

[77] D. Patel, A. Kell, B. Simard, B. Xiang, H. Y. Lin, and G. Tian, "The cell labeling efficacy, cytotoxicity and relaxivity of copper-activated MRI/PET imaging contrast agents," *Biomaterials,* Oct 27 2010.

[78] L. Frullano, C. Catana, T. Benner, A. D. Sherry, and P. Caravan, "Bimodal MR-PET agent for quantitative pH imaging," *Angew Chem Int Ed Engl,* vol. 49, pp. 2382-4, Mar 22 2010.

[79] C. I. Zaragoza, Borja ; Borreguero, Luis Jesus Jimenez; Schulz, Volkmar ; Fayad, Zahi ; Fuster, Valentín "Future Perspectives In Cardiovascular Imaging. Simultaneous PET/MRI Technology In Biomedical Research," 2010.

[80] Y. Wu, C. Catana, R. Farrell, P. A. Dokhale, K. S. Shah, Q. Jinyi, and S. R. Cherry, "PET Performance Evaluation of an MR-Compatible PET Insert," *Nuclear Science, IEEE Transactions on,* vol. 56, pp. 574-580, 2009.

[81] B. J. Peng, J. H. Walton, S. R. Cherry, and J. Willig-Onwuachi, "Studies of the interactions of an MRI system with the shielding in a combined PET/MRI scanner," *Phys Med Biol,* vol. 55, pp. 265-80, 2010.

[82] J. E. Mackewn, P. Halsted, G. Charles-Edwards, R. Page, J. J. Totman, K. Sunassee, D. Strul, W. A. Hallett, M. Jauregui-Osoro, P. Liepins, S. C. R. Williams, T. Schaeffter, S. F. Keevil, and P. K. Marsden, "Performance Evaluation of an MRI-Compatible Pre-Clinical PET System Using Long Optical Fibers," *Nuclear Science, IEEE Transactions on,* vol. 57, pp. 1052-1062, 2010.

[83] H. F. Wehrl, M. S. Judenhofer, A. Thielscher, P. Martirosian, F. Schick, and B. J. Pichler, "Assessment of MR compatibility of a PET insert developed for simultaneous multiparametric PET/MR imaging on an animal system operating at 7 T," *Magn Reson Med,* Aug 30 2010.

[84] G. Delso, A. Martinez-Moller, R. A. Bundschuh, R. Ladebeck, Y. Candidus, D. Faul, and S. I. Ziegler, "Evaluation of the attenuation properties of MR equipment for its use in a whole-body PET/MR scanner," *Phys Med Biol,* vol. 55, pp. 4361-74, Aug 7 2010.

[85] R. H. Hashemi, W. G. Bradley, and C. J. Lisanti, *MRI : the basics*, 2nd ed. Philadelphia: Lippincott Williams & Wilkins, 2004.

[86] D. W. McRobbie, *MRI from picture to proton*, 2nd ed. Cambridge, UK ; New York: Cambridge University Press, 2007.

[87] M. A. Brown and R. C. Semelka, *MRI : basic principles and applications*, 3rd ed. Hoboken, N.J.: Wiley-Liss, 2003.

[88] F. D. Doty, G. Entzminger, J. Kulkarni, K. Pamarthy, and J. P. Staab, "Radio frequency coil technology for small-animal MRI," *NMR Biomed,* vol. 20, pp. 304-25, May 2007.

[89] M. K. D. Belohrad, "Saddle Coil for MRI," *In Proceedings of the 10th International Conference Radioelectronics, Slovak Republic* 2000.

[90] H. D. Chen C, Sank VJ., "Quadrature detection coils—a further sqrt(2) improvement in sensitivity.," *J Magn Reson,* vol. 54, pp. 324–327, 1983.

[91] D. I. Hoult, C. N. Chen, and V. J. Sank, "Quadrature detection in the laboratory frame," *Magn Reson Med,* vol. 1, pp. 339-53, Sep 1984.

[92] J. Mispelter, M. Lupu, A. Briguet, and ebrary Inc., "NMR probeheads for biophysical and biomedical experiments theoretical principles & practical guidelines," Imperial College Press, 2006, pp. xiv, 596 p.

[93] C. Woody, P. Vaska, D. Schlyer, J. F. Pratte, S. Junnarkar, S. J. Park, S. Stoll, M. Purschke, S. Southekal, A. Kriplani, S. Krishnamoorthy, S. Maramraju, D. Lee, W. Schiffer, S. Dewey, J. Neill, A. Kandasamy, P. O'Connor, V. Radeka, R. Fontaine, and R. Lecomte, "Initial studies using the RatCAP conscious animal PET tomograph," *Nucl Inst Met Phys Res Sec A,* vol. 571, pp. 14-17, 2007.

[94] P. Vaska, C. L. Woody, D. J. Schlyer, S. Shokouhi, S. P. Stoll, J. F. Pratte, P. O'Connor, S. S. Junnarkar, S. Rescia, B. Yu, M. Purschke, A. Kandasamy, A. Villanueva, A. Kriplani, V. Radeka, N. Volkow, R. Lecomte, and R. Fontaine, "RatCAP: miniaturized head-mounted PET for conscious rodent brain imaging," *IEEE Trans Nucl Sci.,* vol. 51, pp. 2718-2722, 2004.

[95] P. Vaska, C. Woody, D. Schlyer, J. F. Pratte, S. Junnarkar, S. Southekal, S. Stoll, D. Schulz, W. Schiffer, D. Alexoff, D. Lee, V. Patel, M. Purschke, W. Lee, J. Fried, W. Lenz, S. Krishnamoorthy, S. Maramraju, A. Kriplani, V. Radeka, P. O'Connor, R. Lecomte, and R. Fontaine, "The design and performance of the 2nd-generation RatCAP awake rat brain PET system," *IEEE Nucl Sci Symp Conf Rec.,* vol. 6, pp. 4181-4184, 2007.

[96] J. F. Pratte, S. Junnarkar, G. Deptuch, J. Fried, P. O'Connor, V. Radeka, P. Vaska, C. Woody, D. Schlyer, S. Stoll, S. H. Maramraju, S. Krishnamoorthy, R. Lecomte, and R. Fontaine, "The RatCAP Front-End ASIC," *IEEE Trans Nucl Sci.,* vol. 55, pp. 2727-2735, 2008.

[97] S. S. Junnarkar, J. Fried, S. Southekal, J. F. Pratte, P. O'Connor, V. Radeka, P. Vaska, M. Purschke, D. Tomasi, C. Woody, and R. Fontaine, "Next Generation of Real Time Data Acquisition, Calibration and Control System for the RatCAP Scanner," *IEEE Trans Nucl Sci.,* vol. 55, pp. 220-224, 2008.

[98] S. J. Park, S. Southekal, M. Purschke, S. S. Junnarkar, J. F. Pratte, S. P. Stoll, C. L. Woody, D. J. Schlyer, and P. Vaska, "Digital Coincidence Processing for the RatCAP Conscious Rat Brain PET Scanner," *IEEE Trans Nucl Sci.,* vol. 55, pp. 510-515, 2008.

[99] S. Southekal, M. Purschke, C. L. Woody, D. J. Schlyer, and P. Vaska, "Optimization of image reconstruction for the RatCAP (PET) tomograph: An analysis of the statistical quality of the system response matrix," *IEEE Nucl Sci Symp Conf Rec,* vol. 4, pp. 3051-3054, 2007.

[100] A. Kriplani, S. P. Stoll, D. J. Schlyer, S. Shokouhi, P. Vaska, A. Villanueva, Jr., and C. L. Woody, "Light output measurements of LSO single crystals and 4×8 arrays: comparison of experiment with Monte Carlo simulations," in *Nuclear Science Symposium Conference Record, 2003 IEEE*, 2003, pp. 3036-3040 Vol.5.

[101] C. Woody, V. Dzhordzhadze, R. Fontaine, S. Junnakar, A. Kandasamy, A. Kriplani, S. Krishnamoorthy, R. Lecomte, P. O. Connor, C. Page, J. F. Pratte, M. Purschke, V. Radeka, I. Rampil, D. Schlyer, S. Shokouhi, S. Southekal, S. Stoll, P. Vaska, A. Villanueva, and B. Yu, "The RatCAP conscious small animal PET tomograph," in *Nuclear Science Symposium Conference Record, 2004 IEEE*, 2004, pp. 2334-2338 Vol. 4.

[102] R. L. H. T. K. Lewellen, and S. Vannoy, "The SimSET program (Chapter 7)," in *Monte Carlo calculations in nuclear medicine: applications in diagnostic imaging*, 1998, pp. 77-92.

[103] S. Southekal, "Strategies for quantitative neuroimaging with the Rat Conscious Animal PET (RatCAP) [PhD. Dissertation]. Stony Brook, NY. Stony Brook University," 2009.

[104] J. Mispelter, M. Lupu, A. Briguet, and ebrary Inc., "NMR probeheads for biophysical and biomedical experiments theoretical principles & practical guidelines. Chapter 10, page 504.," Imperial College Press, 2006, pp. xiv, 596 p.

[105] B. L. Wilkoff, D. Bello, M. Taborsky, J. Vymazal, E. Kanal, H. Heuer, K. Hecking, W. B. Johnson, W. Young, B. Ramza, N. Akhtar, B. Kuepper, P. Hunold, R. Luechinger, H. Puererfellner, F. Duru, M. J. Gotte, R. Sutton, and T. Sommer, "Magnetic Resonance Imaging in Patients with a Pacemaker System Designed for the MR Environment," *Heart Rhythm,* Oct 5.

[106] T. G. Reese, O. Heid, R. M. Weisskoff, and V. J. Wedeen, "Reduction of eddy-current-induced distortion in diffusion MRI using a twice-refocused spin echo," *Magn Reson Med,* vol. 49, pp. 177-82, Jan 2003.

[107] U. Klose, "In vivo proton spectroscopy in presence of eddy currents," *Magn Reson Med,* vol. 14, pp. 26-30, Apr 1990.

[108] F. Schick, "Whole-body MRI at high field: technical limits and clinical potential," *Eur Radiol,* vol. 15, pp. 946-59, May 2005.

[109] L. Friedman and G. H. Glover, "Report on a multicenter fMRI quality assurance protocol," *J Magn Reson Imaging,* vol. 23, pp. 827-39, Jun 2006.

[110] H. W. Ott, *Electromagnetic Compatibility Engineering*. Hoboken, New Jersey: John Wiley & Sons, 2009.

[111] E. Solis, D. Tomasi, S. Junnarkar, D. Schlyer, P. Vaska, C. Woody, J. F. Pratte, P. O'Connor, and A. O. Rodriguez, "Shielded transceiver RF coil array for simultaneous PET-MRI," *Brazilian Journal of Physics,* vol. 38, pp. 287-291, 2008.

[112] "IEEE Standard for Measuring the Effectiveness of Electromagnetic Shielding Enclosures," *IEEE Std 299-1991,* p. 1, 1991.

[113] H. W. Ott, "Noise Reduction Techniques in Electronic Systems," Wiley, 1988.

[114] R. Morrison, *Grounding and Shielding Techniques*, Fourth edition ed.: Wileys, 1998.

[115] W. D. Kimmel and D. D. Gerke, *Electromagnetic compatibility in medical equipment : a guide for designers and installers*. New York, Buffalo Grove, Ill.: Institute of Electrical and Electronics Engineers; Interpharm Press, 1995.

[116] D. L. Terrell, *Digital Design for Interference Specifications*: TKC, 1997.

[117] X. C. Tong, "Advanced materials and design for electromagnetic interference shielding," Boca Raton: CRC Press, 2009, pp. xv, 313 p.

[118] M. Mardiguian, *Controlling radiated emissions by design*, 2nd ed. Boston: Kluwer Academic Publishers, 2001.

[119] C. R. Paul, *Introduction to electromagnetic compatibility*, 2nd ed. Hoboken, N.J.: Wiley-Interscience, 2006.

[120] V. Radheka, "Shielding and grounding in large detectors," *4th workshop on electronics for LHC experiments, Rome (Italy),* pp. 21-25, 1998.

[121] H. W. Ott, *Electromagnetic Compatibility Engineering, Chapter 6, page 298.* Hoboken, New Jersey: John Wiley & Sons, 2009.

[122] K. A. Bakshi, *Antennas And Wave Propagation*. Pune, India: Technical Publications, 2009.

[123] A. K. Sharma, Mishra, K.K., Raghuramaiah, M. Naik,P.A., and P.D.Gupta, "Design and Performance Characteristics of an Electromagnetic Interference Shielded Enclosure for High Voltage Pockels Cell Switching System," *Sadhana,* vol. 32, pp. 235-242, 2007.

[124] R. B. Schulz, V. C. Plantz, and D. R. Brush, "Shielding theory and practice," *Electromagnetic Compatibility, IEEE Transactions on,* vol. 30, pp. 187-201, 1988.

[125] L. Ferraris and W. Chang-Yu, "EMI shielding-common problems and containment strategies," in *Electromagnetic Compatibility Proceedings, 1997 International Symposium on*, 1997, pp. 86-89.

[126] H. W. Ott, "Ground - a path for current to flow," *IEEE Intl. Symp. Electromagnetic Compatibility,* 1979.

[127] M. Montrose, *EMC and Printed circuit Board Design - Design, Theory and Layout made Simple*. Piscataway, NJ: IEEE Press, 1999.

[128] M. Montrose, I., *Printed Circuit Board Design Techniques for EMC Applications - AHandbook for Designers*. Piscataway, NJ: IEEE Press, 2000.

[129] R. Schmitt and Knovel (Firm), "Electromagnetics explained a handbook for wireless/RF, EMC, and high-speed electronics," in *EDN series for design engineers* Amsterdam ; Boston: Newnes, 2002, pp. xvi, 359 p.

[130] R. Schmitt, "Understanding electromagnetic fields and antenna radiation takes (almost) no math," in *EDN* March 2, 2000.

[131] D. Westen, *Cable Shielding for Electromagnetic Compatibility*: Springer, 1995.

[132] H. W. Ott, *Electromagnetic Compatibility Engineering, Cabling, page 85*. Hoboken, New Jersey: John Wiley & Sons, 2009.

[133] R. Morrison, *Grounding and Shielding*: Wiley, 2007.

[134] C. R. Paul, "Effect of Pigtails on Crosstalk to Braided-Shield Cables," *Electromagnetic Compatibility, IEEE Transactions on,* vol. EMC-22, pp. 161-172, 1980.

[135] H. W. Ott, *Electromagnetic Compatibility Engineering, Chapter 2, page 90.* Hoboken, New Jersey: John Wiley & Sons, 2009.

[136] R. R. Price, L. Axel, T. Morgan, R. Newman, W. Perman, N. Schneiders, M. Selikson, M. Wood, and S. R. Thomas, "Quality assurance methods and phantoms for magnetic resonance imaging: report of AAPM nuclear magnetic resonance Task Group No. 1," *Med Phys,* vol. 17, pp. 287-95, Mar-Apr 1990.

[137] C. R. Paul, *Introduction to electromagnetic compatibility (Chapter 10, page 734)*, 2nd ed. Hoboken, N.J.: Wiley-Interscience, 2006.

[138] L. H. Hemming, "Architectural electromagnetic shielding handbook a design and specification guide " New York: IEEE Press :Institute of Electrical and Electronics Engineers, 1992, pp. xviii, 222 p.

[139] J. T. Vaughan, G. Adriany, M. Garwood, E. Yacoub, T. Duong, L. DelaBarre, P. Andersen, and K. Ugurbil, "Detunable transverse electromagnetic (TEM) volume coil for high-field NMR," *Magn Reson Med,* vol. 47, pp. 990-1000, May 2002.

[140] J. T. Vaughan, H. P. Hetherington, J. O. Otu, J. W. Pan, and G. M. Pohost, "High frequency volume coils for clinical NMR imaging and spectroscopy," *Magn Reson Med,* vol. 32, pp. 206-18, Aug 1994.

[141] M. Alecci and P. Jezzard, "Characterization and reduction of gradient-induced eddy currents in the RF shield of a TEM resonator," *Magn Reson Med,* vol. 48, pp. 404-7, Aug 2002.

[142] B. Wu, C. Wang, D. A. Kelley, D. Xu, D. B. Vigneron, S. J. Nelson, and X. Zhang, "Shielded microstrip array for 7T human MR imaging," *IEEE Trans Med Imaging,* vol. 29, pp. 179-84, Jan.

[143] G. Shen, "Double-sided stripline RF shield," *Proc. 11th Annu. Meeting ISMRM,* p. 4048, 1992.

[144] H. W. Ott, *Electromagnetic Compatibility Engineering, Chapter 6, page 270.* Hoboken, New Jersey: John Wiley & Sons, 2009.

[145] D. Westen, *Electromagnetic Compatibility - principles and applications*: Marcel Dekker, 2001.

[146] X. Liu and S. Y. R. Hui, "An Analysis of a Double-layer Electromagnetic Shield for a Universal Contactless Battery Charging Platform," in *Power Electronics Specialists Conference, 2005. PESC '05. IEEE 36th*, 2005, pp. 1767-1772.

[147] W. Liuping, G. Yougang, S. Yuanmao, and R. Fangming, "Analysis on Shielding Effectiveness of Aperture Arrays with Different Spacing," in *Electromagnetic Compatibility, 2007. EMC 2007. International Symposium on*, 2007, pp. 333-336.

[148] Y. Trenkler and L. E. McBride, "Shielding improvement by multi-layer design," in *Electromagnetic Compatibility, 1990. Symposium Record., 1990 IEEE International Symposium on*, 1990, pp. 1-4.

[149] S. M. Yang, Y. Y. Chang, Y. C. Hsieh, Y. J. Lee, "Electromagnetic shielding effectiveness of multilayer metallic thin film on plastic substrates," in *www.onlinelibrary.wiley.com/doi/10.1002/app.28806/pdf*, 2008.

[150] J. Joo and C. Y. Lee, "High frequency electromagnetic interference shielding response of mixtures and multilayer films based on conducting polymers," *Journal of Applied Physics,* vol. 88, pp. 513-518, 2000.

[151] V. Neganov, "A self-consistent method for the electromagnetic-field calculation in near-field regions of radiating structures with cylindrical surfaces," *Doklady Physics,* vol. 51, pp. 234-237, 2006.

[152] H. W. Ott, *Electromagnetic Compatibility Engineering, Chapter 18, page 690.* Hoboken, New Jersey: John Wiley & Sons, 2009.